Ref. Ares(2026)5175599 - 21/05/2026

Co-funded by the European Union

6GSNS

SUPERIOT

D2.4 Energy subsystem for node integration

Project number	**101096021**
Project name	**Truly Sustainable Printed Electronics-based IoT Combining Optical and Radio Wireless Technologies**
Project acronym	**SUPERIOT**
Call	**HORIZON-JU-SNS-2022**
Deliverable No	**D2.4**
Deliverable Name	**Energy subsystem for node integration**
Status	**Final**
Dissemination level	**Public**
Due date of deliverable	**2024-12-31 (M24)**
Actual submission date	**2024-12-27 (M24)**
Resubmission date	**2026-05-21**
Work package	**WP2 "Sustainable RIoT Node"**
Lead beneficiary	**KU Leuven**
Authors	Yasser Qaragoez, Khodr Hammoud, KU Leuven Junaid Bocus, Kerstin Eder, U of Bristol Marja Välimäki, VTT Joana Vaz Pinto, Joao Coelho, NOVA.id.FCT Marcin Drzewiecki, MPICOSYS
Reviewers:	Jaakko Leppäniemi, VTT Dominique Schreurs, KU Leuven

The SUPERIOT project has received funding from the Smart Networks and Services Joint Undertaking (SNS JU) under the European Union's Horizon Europe research and innovation programme under Grant Agreement No 101096021, including top-up funding by UK Research and Innovation (UKRI) under the UK government's Horizon Europe funding guarantee.

Views and opinions expressed are however those of the authors only and do not necessarily reflect those of the European Union, SNS JU or UKRI. The European Union, SNS JU or UKRI cannot be held responsible for them.

Executive Summary

The SUPERIOT project operates in the emerging printed electronics domain, focused on IoT applications. This deliverable focuses on enhancing energy efficiency and integration in node-level systems through innovative modelling, energy harvesting, and communication techniques. It involves measuring and analysing energy consumption and power dissipation to develop and validate novel energy and power models that optimize usage during development and runtime. In addition, RF and light energy harvesting modules are designed with a shared power management system, utilizing printed components such as RF antennas, PV cells, rectifiers, and supercapacitors to achieve high efficiency, including significant RF power conversion.

Indicative experimental results confirm the viability of the approach. Under indoor illumination of approximately 937 lx, the light-harvesting subsystem delivers sub-milliwatt power levels, specifically around 0.45 mW unloaded, 0.35 mW under load, and about 0.36 mW transferred to the supercapacitor through an 80%-efficient DC-DC converter. The dual-band RF rectifier exhibits measured power-conversion efficiencies of approximately 53% at 920 MHz and 40% at 2.5 GHz and over-the-air measurements at 1 m with a transmitted power of 19 dBm yield average rectifier output voltages of roughly 0.586 V and 0.126 V at the two RF outputs, respectively. Additional effort has been devoted to the compact co-integration of RF antennas and PV cells to enable combined RF and optical harvesting within a shared form factor. Simultaneous wireless power and information transfer, both RF-based and light-based, is explored through energy-efficient architectures that enable information down conversion and uplink communication via RF backscattering. Printed components are central to practical implementation, and the most effective approaches will progress to demonstrator systems in WP4.

Table of contents

Editions

Version	Date	Modified by	Modification
0.1	2024-11-16	Yasser Qaragoez, KU Leuven	Initial template
0.2	2024-12-14	Khodr Hammoud, KU Leuven	Modified template
0.3	2024-12-19	Yasser Qaragoez, KU Leuven	Internal review document
1.0	2024-12-27	Yasser Qaragoez and Khodr Hammoud, KU Leuven	Final document for submission
2.0	2026-05-22	Junaid Bocus, and Kerstin Eder, U of Bristol Yasser Qaragoez and Khodr Hammoud, KU Leuven	Modifications addressing the request for revision in Executive Summary and Section 3 (including 3.2, 3.2.1, 3.3.1, 3.3.2, 3.3.2.2, 3.3.2.3). Texts revisited throughout Section 3.

1 Acronyms

a-Si	Amorphous Silicon
Ag	Silver
Al	Aluminum
app	Application
BLE	Bluetooth Low Energy
CIGS	Copper Indium Gallium Selenide
CPU	Central Processing Unit
E-ink	Electronic Ink
GPIO	General-Purpose Input/Output
H_2SO_4	Sulfuric Acid
IC	Integrated Circuit
IR	Infrared
ISR	Interrupt Service Routine
JSON	JavaScript Object Notation
LED	Light-Emitting Diode
LiCl	Lithium Chloride
LiF	Lithium Fluoride
LUT	Look Up Table
MTU	Maximum Transmission Unit
NBVLC	Narrowband Visible Light Communication
NEC	Nippon Electric Company
NF3000	Organic Conductive Polymer
OOK	On-Off Keying
OPV	Organic Photovoltaic
OS	Operating System
OTA	Over-The-Air

P3HT:PCBM	Poly (3-Hexylthiophene)/Phenyl-C61-Butyric Acid Methyl Ester
PCB	Printed Circuit Board
PCE	Power Conversion Efficiency
PEDOT:PSS	Poly (3,4-EthyleneDiOxyThiophene) Polystyrene Sulfonate
PE	Printed Electronic
PEN	Polyethylene Naphtholate
PH1000	Poly (Styrene Sulfonic Acid)
PHY	Physical Layer
PPKII	Power Profiler Kit II
Pt	Platinum
PVA	Polyvinyl Alcohol
PWM	Pulse Width Modulation
RIoT	Reconfigurable Internet-of-Things
RX	Receiver
S_{11}	Reflection Coefficient (transmission line)
SLIPT	Simultaneous Light Information and Power Transfer
SoC	System-on-Chip
SWIPT	Simultaneous Wireless Information and Power Transfer
Ti	Titanium
TV	Television
TX	Transmitter
UART	Universal Asynchronous Receiver-Transmitter
USB	Universal Serial Bus
VLC	Visible Light Communication
ZTO	Zinc Tin Oxide
μSC	Micro Supercapacitor

2 Introduction

2.1 Motivation

The ever-expanding Internet of Things (IoT) paradigm holds the promise of connecting billions—and eventually trillions—of entities, facilitating wide-ranging applications in healthcare, smart cities, energy management, logistics, and beyond. Yet, as the number of deployed IoT nodes grows exponentially, so does the environmental footprint associated with manufacturing, powering, and disposing of these devices. The key challenge is to realize a hyperconnected world while ensuring economic and ecological sustainability.

Task 2.4 of the SUPERIOT project directly addresses these challenges by advancing eco-friendly node design and reducing the reliance on non-renewable power sources. Our ambition aligns with the broader mission stated in the proposal: leveraging dual connectivity (RF and light) and sustainable materials—particularly through printed electronics—to achieve the dual goal of robust functionality and minimal environmental impact.

2.2 Background and Objectives

Traditional IoT systems often rely on large-scale deployments of battery-powered devices, which poses multiple sustainability concerns:

- **Resource Use**: Vast numbers of IoT nodes lead to high consumption of critical raw materials and increased e-waste.
- **Energy Consumption**: Even small per-node power draws become significant at scale.
- **Network Infrastructure**: Maintaining dedicated wireless networks for billions of devices incurs infrastructure costs and energy overhead.

To address these challenges, the proposal advocates for exploiting existing communication infrastructures—such as hybrid light–radio networks—and adopting eco-design principles, including the use of printed electronics (PE). These strategies promise to reduce the environmental burden while enabling IoT solutions to remain economically viable and scalable.

2.3 Scope of the Deliverable

Within this broader sustainability-driven vision, Task 2.4 focuses on designing, implementing, and experimentally validating a sustainable energy subsystem that integrates:

- **RF Energy Harvesting:** High power-conversion efficiency rectifiers and efficient waveforms for wireless power transfer, thereby enabling Simultaneous Wireless Information and Power Transfer (SWIPT).
- **Light Energy Harvesting:** Visible-light-based systems that scavenge energy from ambient or dedicated light sources, thereby enabling Simultaneous Light Information and Power Transfer (SLIPT).

The subsystem leverages both radio and light domains for data and power transmission using printed electronics, specifically OPV and μSC, as detailed in D2.2 and D2.3. This approach enables energy-autonomous operation, minimizes reliance on external power supplies, and significantly extends node lifetimes by reducing the need for frequent battery replacements. By harnessing the advantages of printed electronics, the project addresses operational energy consumption, material footprint, and end-of-life sustainability considerations. In addition, energy measurement and modeling aim to optimize and address power consumption in the Si node core (as reported in D2.1) and across modes such as BLE and NBVLC. Validated models guide energy-efficient designs as the project progresses toward printed electronics and energy harvesting.

2.4 Structure of the Document

- **Section 3** – Analysis and Prediction of Energy Consumption: Details the measurement setups, energy models, and predictive frameworks designed to optimize node-level energy usage, resonating with Task 2.4.1.
- **Section 4** – Summarizes the development of printed energy components within the SUPERIOT project, including Zinc Tin Oxide (ZTO) diodes, MXene-based micro supercapacitors (μSCs), and organic photovoltaics (OPVs). It discusses their fabrication, performance characterization, and integration into demonstrators, highlighting advancements and optimizations for sustainable IoT applications.
- **Section 5** – SWIPT System with Integrated Printed solar cell and supercapacitor: Demonstrates how SWIPT can be coupled with backscatter communication (Task 2.4.2/2.4.3) to achieve near-battery less operation.
- **Section 6** – SLIPT System with Integrated Printed Electronics: Extends the dual-mode concept to the light domain, merging visible-light energy harvesting with light wireless communication.
- **Section 7** – Evaluating different designs for the energy subsystem of the RIoT node, focusing on its three key components: energy conversion, energy storage, and energy management. Each design is analyzed in the context of demonstrators and use cases, highlighting sustainability, reconfigurability, and efficiency while addressing specific operational and environmental requirements.
- **Section 8** – Summarizes the alignment of these subsystems with the proposal's high-level KPIs and goals, offering recommendations for future tasks and WP4 demonstrators.

3 Analysis and Prediction of Energy Consumption at Node Level

This chapter explores the essential process of energy measurement, analysis, modelling, and prediction for the silicon (Si)-based reference Reconfigurable Internet-of-Things (RIoT) node, developed during the initial phase of the SUPERIOT framework. Readers seeking more information on the Si-based node developed by UOULU are encouraged to consult deliverables D2.1 and D2.3. Detailed energy measurements were conducted on the Si-based RIoT node, examining its power consumption across different operating modes, including Bluetooth Low Energy (BLE), Narrowband Visible Light Communication (NBVLC), sensing, and E-ink display functionalities. We also present the optimization strategies implemented to substantially reduce energy usage at both the firmware and hardware levels. Additionally, measurement-based models and predictive frameworks were developed to estimate and predict the node's energy consumption under varying operational conditions and configurations. The validation of the energy consumption models will support the energy management and optimization at the node level. The developed models and measurement data will also be instrumental in achieving energy-efficient nodes, particularly as the system integrates energy harvesting and evolves toward printed electronics. This will ensure that different energy-saving techniques are applied appropriately, providing a structured approach to achieving the balance between functionality and energy sustainability in each design iteration. As the project progresses toward a fully printed RIoT node, these insights will be invaluable in guaranteeing that the final system can achieve sufficiently low power consumption while maintaining the required performance and functionality.

3.1 Energy Measurement Setup

During the design phase, several cut (measuring) points were integrated on the Si-based RIoT node (see Figure 3.1.1) to facilitate current measurement across different parts of the node under normal operation. These cut points are shorted by default; hence they must be cut to allow current measurement across the core components. The specific cut-points are as follows:

- **U1**: Allows current measurement from 3.3 V supply to the nRF52833, wake-up IC, and sensor.
- **U2**: Facilitates current measurement from 3.3 V supply to the E-ink driver and Narrow-band VLC TX and RX (NBVLC TX/RX).
- **U7**: Dedicated to measuring current to the NBVLC TX module only.
- **U9**: Dedicated to measuring current to the NBVLC RX module only.
- **U6**: Not used for current measurement but can be cut to reduce the deep sleep current while E-ink display is powered off.

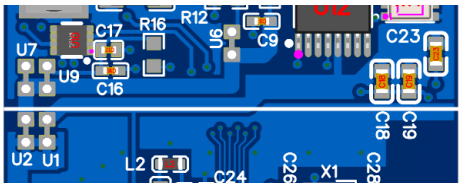

Figure 3.1.1. Cut points on Si-based RIoT node (see markings U1, U2, U6, U7, and U9).

We utilized the Power Profiler Kit II (PPKII) by Nordic Semiconductor to perform an in-depth energy analysis on the Si-based node. Figure 3.1.2 shows the overall diagram of the hardware setup utilized in our current consumption analysis. Overall, five PPKII boards were used. One is used in power supply mode (3.3 V) to power the Si-based node through the H1 pins and simultaneously obtain current measurements across the node. The other four PPKII boards are set to ammeter mode and connected across the four cut points of the Si-based node, namely, U1, U2, U7, and U9. All PPKII boards were connected via USB to a laptop to record the current measurements using the *nRF Connect for Desktop* app (available for download for all operating systems from Nordic Semiconductor website).

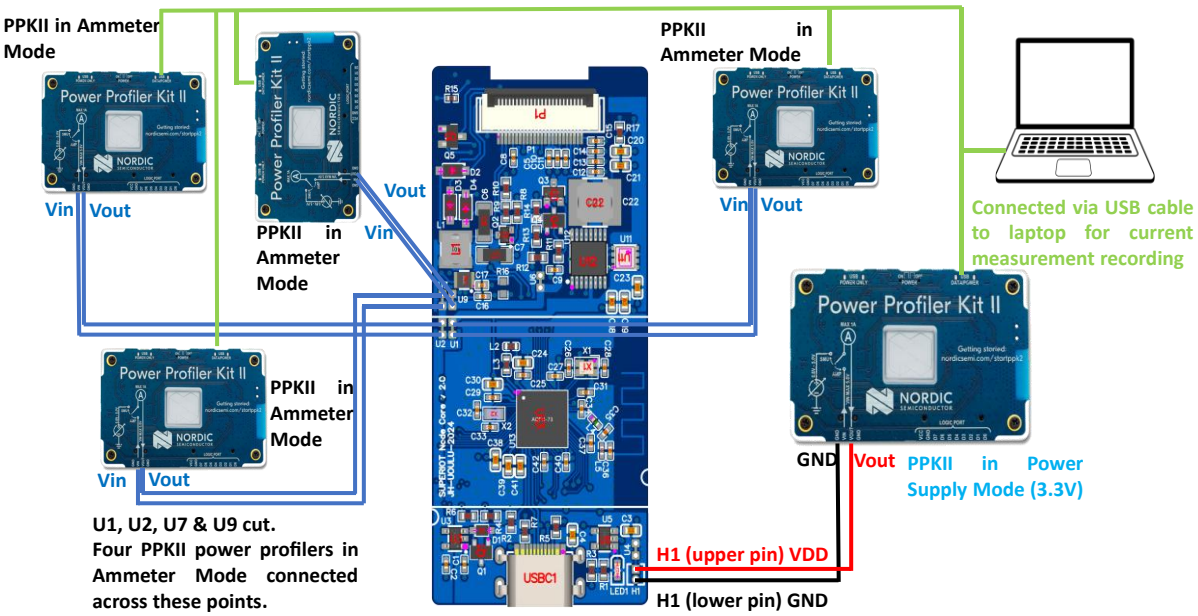

Figure 3.1.2. Diagram detailing the hardware setup of the node for current measurement. Points U1, U2, U6, U7 and U9 were cut, and jumper wires soldered across them to allow easy connection with power profilers. The cut points can also be easily shorted back.

3.2 Energy measurement and analysis

Using the different firmware test modes, a series of experiments was conducted to characterise the current and energy consumption of the Si-based RIoT node. The measurements were performed at different cut points to separate the contributions of the main controller branch and the optical communication/display branch. In particular, U1 corresponds to the branch containing the nRF52833 BLE SoC together with the wake-up IC and sensor-related circuitry, whereas U2 corresponds to an aggregate branch containing the E-ink display, NBVLC TX, and NBVLC RX circuitry. The additional cut points U7 and U9 were used only to isolate the NBVLC TX and NBVLC RX contributions, respectively. Therefore, U7 and U9 are diagnostic sub-branch measurements and are not added separately to U2 when discussing the total node current.

For a periodic firmware mode with cycle duration T_c, the average current at a given cut point may be expressed as

$$\bar{I} = \frac{1}{T_c}\int_0^{T_c} i(t)\,dt, \tag{3.1}$$

where $\bar{I}$ denotes the cycle-averaged current, $i(t)$ is the instantaneous current at time t, and T_c is the total duration of one operating cycle.

When an operation alternates between an active interval and an idle interval, the cycle-averaged current can equivalently be written as

$$\bar{I} = \frac{I_{\text{act}}\,t_{\text{act}} + I_{\text{idle}}\,t_{\text{idle}}}{t_{\text{act}} + t_{\text{idle}}}\ , \tag{3.2}$$

where I_{act} and I_{idle} are the average currents during the active and idle intervals, respectively, and t_{act} and t_{idle} are the corresponding durations of these intervals.

To quantify the relative dominance of the main controller branch in the experiments below, it is useful to define the branch-current share of U1 as

$$\rho_{U1} = \frac{\bar{I}_{U1}}{\bar{I}_{U1} + \bar{I}_{U2}}, \tag{3.3}$$

where $\bar{I}_{U1}$ and $\bar{I}_{U2}$ denote the cycle-averaged currents measured at cut points U1 and U2, respectively, and ρ_{U1} represents the fraction of the total measured branch current attributed to U1. Here, U2 already includes the aggregate contribution of the E-ink display, NBVLC TX, and NBVLC RX circuitry. Here, $\rho_{U1} \in [0,1]$ provides a normalized measure of the relative dominance of the U1 branch with respect to the combined current of U1 and U2.

Table 1. Current consumption over a periodic duty cycle, including sensing, e-ink display updates, and idle phases.

	Average current consumption (mA)			
Measuring point	**Overall**	**Idle state after E-ink display / Idle state between sensing and E-ink display (~7.5 s) / (~200 ms)**	**Sensing (~516 ms)**	**E-ink display (~2.8 s)**
U1 (nRF52833, wake-up IC, sensor)	5.79	5.47 / 5.48	12.05	5.52
U2 (E-ink, NBVLC TX, NBVLC RX)	0.727	0.406 / 0.410	0.408	1.68
U7 (NBVLC TX)	0.0003	0.0003 / 0.0003	0.0003	0.0003
U9 (NBVLC RX)	0.328	0.327 / 0.328	0.329	0.331

3.2.1 Sensing and E-ink display test under BLE-connected operation

In this experiment, the node is connected via BLE to a smartphone acting as the central device, and the firmware test mode is activated using the *nRF Connect* application. During each cycle, the node performs sensing using the integrated BME688 sensor for approximately 516 ms, and then after an idle period of approximately 200 ms, it updates the E-ink display for approximately 2.8 s, and then remains idle again for approximately 7.5 s, giving a total cycle duration of about 11 s. Here, "idle" means that the node is not performing sensing, display, or active data transmission operations, but it remains connected over BLE to the central device using a connection interval of 45 ms and BLE TX power of 0 dBm. In the firmware, this idle period consists of a 2 s delay after the E-ink update followed by a further 5 s delay before the next cycle begins.

Table 1 reports the average current measured at U1, U2, U7, and U9 during the different phases of this test mode. Since the node remains BLE-connected throughout the full operating cycle, the nRF52833 stays active continuously, even when no explicit BLE application payload is being transmitted. Consequently, the current observed at U1 should be interpreted as the current of the BLE-connected controller branch.

The results show that the main controller branch is the dominant contributor to the cycle-averaged current. Using the aggregate comparison between U1 and U2, the overall current share of U1 is

$$\rho_{U1,\text{overall}} = \frac{5.79}{5.79 + 0.727} \approx 0.888, \tag{3.4}$$

that is, about **88.8%** of the measured total branch current. During the two BLE-connected idle intervals (i.e. idle portion after E-ink update and idle portion between sensing and E-ink update), the U1 share becomes:

$$\frac{5.47}{5.47+0.406} \approx 0.931 \text{ and } \frac{5.48}{5.48+0.410} \approx 0.931, \quad (3.5)$$

which corresponds to approximately **93.1%**. This confirms that, under BLE-connected standby conditions, the average node current is dominated by the BLE SoC/controller branch.

The sensing activity is mainly reflected in U1. During sensing, the U1 current increases to 12.05 mA, whereas U2 remains at about 0.408 mA, very close to its idle value. This is consistent with the fact that the sensor and associated digital control reside in the U1 branch rather than the U2 branch.

The E-ink update, by contrast, is visible mainly in U2. During the E-ink display period, U2 rises from its idle level of about 0.41 mA to 1.68 mA. Since NBVLC TX and NBVLC RX are inactive in this firmware mode, their currents remain essentially unchanged at approximately 0.0003 mA and 0.331 mA, respectively. Therefore, the E-ink-related current during its active interval can be approximated as

$$I_{\text{E-ink}} \approx 1.68 - 0.0003 - 0.331 \approx 1.35 \text{ mA}. \quad (3.6)$$

Thus, the E-ink display contributes a clear increase in current when active, but its average contribution remains lower than that of the BLE-connected SoC branch. Nevertheless, because the display refresh lasts significantly longer than the short NBVLC bursts discussed later, the E-ink can still make an important contribution to the energy per operation.

Overall, this experiment shows that in a BLE-connected sensing-and-display cycle, the dominant average current contribution originates from the continuously active BLE SoC/controller branch at U1, whereas the E-ink contribution appears as a secondary but clearly observable rise in U2 during the display period.

Table 2. Current consumption over a periodic duty cycle consisting of NBVLC TX/RX phase and an idle phase.

	Average current consumption (mA)		
Measuring point	**Overall**	**Idle state between NBVLC TX/RX (~5.31 s)**	**NBVLC TX/RX (~84 ms)**
U1 (nRF52833, wake-up IC, sensor)	5.42	5.42	5.42
U2 (E-ink, NBVLC TX, NBVLC RX)	0.458	0.407	3.74
U7 (NBVLC TX)	0.0402	0.00035	2.56
U9 (NBVLC RX)	0.329	0.328	0.427

3.2.2 NBVLC transmission and reception test under BLE-connected operation

In this experiment, the node is again connected via BLE to a central device, and the corresponding firmware test mode is activated using *nRF Connect* application. During this test, the node performs NBVLC transmission and immediate reception of a 32-bit NEC packet. Between these NBVLC events, the node remains idle for about 5.31 s while still maintaining the BLE connection to the central device, using a connection interval of 45 ms and BLE TX power of 0 dBm. The E-ink display and sensor are inactive in this experiment. The transmitted NBVLC message is emitted using the node's built-in IR LED transmitter and then received immediately by the built-in NBVLC receiver, which occurs over a period of about 84 ms.

Table 2 reports the average current during the NBVLC TX/RX event and during the idle period. As in the previous test, U1 corresponds to the BLE-connected controller branch, while U2 corresponds to the aggregate branch containing the optical/display circuitry. The cut points U7 and U9 are again used only to isolate the NBVLC TX and NBVLC RX contributions, respectively.

The results show that the current at U1 remains almost unchanged between idle and NBVLC-active periods, staying at approximately 5.42 mA. This indicates that the main SoC/controller branch continues to dominate the baseline consumption because the node remains BLE-connected throughout the test. Using the aggregate comparison between U1 and U2, the U1 share of the measured total branch current is

$$\rho_{U1,\text{overall}} = \frac{5.42}{5.42 + 0.458} \approx 0.922, \tag{3.7}$$

that is, about **92.2%** overall. During the BLE-connected idle interval, this increases further to

$$\rho_{U1,\text{idle}} = \frac{5.42}{5.42 + 0.407} \approx 0.930, \tag{3.8}$$

or about **93.0%**. Hence, as in Section 3.2.1, the average node current under BLE-connected idle conditions is dominated by the main SoC branch.

When the NBVLC subsystem becomes active, however, the aggregate U2 current rises strongly from about 0.407 mA to 3.74 mA, showing that NBVLC operation is clearly visible in the optical/display branch. The detailed sub-branch measurements reveal that the largest increase occurs in U7, i.e., the NBVLC TX branch, whose current rises from about 0.00035 mA in idle to approximately 2.56 mA during the NBVLC-active interval. The U9 branch, corresponding to NBVLC RX, increases more modestly from about 0.328 mA to 0.427 mA.

The key distinction here is between instantaneous current during the active interval and cycle-averaged current over the full period. Although NBVLC TX reaches 2.56 mA when active, this occurs only for about 84 ms, followed by an idle interval of about 5.31 s. Its average current over the full cycle is therefore

$$\bar{I}_{U7} = \frac{2.56 \times 0.084 + 0.00035 \times 5.31}{0.084 + 5.31} \approx 0.0402 \text{ mA}, \tag{3.9}$$

which agrees with Table 2. Similarly, for the receiver branch,

$$\bar{I}_{U9} = \frac{0.427 \times 0.084 + 0.328 \times 5.31}{0.084 + 5.31} \approx 0.329 \text{ mA}, \tag{3.10}$$

which also agrees with the measured value. These results show that NBVLC TX produces a pronounced but brief current burst, while NBVLC RX shows only a moderate increase over its idle current.

Therefore, the correct interpretation is not that NBVLC is negligible when active, but rather that its duty cycle is very low, so its contribution to the overall cycle-averaged current is modest compared with the continuously active BLE-connected SoC branch. During the short NBVLC-active interval, the U2 branch becomes much more significant; however, once averaged over the full cycle, the U1 branch remains dominant because it is active continuously for connection maintenance and firmware execution.

3.2.3 Summary of key insights

The measured in Sections 3.2.1 and 3.2.2 show that BLE and NBVLC influence node power consumption in fundamentally different ways. BLE establishes the persistent communication baseline of the node, as the nRF52833 remains active in connected mode throughout the measurement interval. As a result, BLE dominates the time-averaged current consumption across the examined firmware modes. In particular, the main SoC/controller branch (U1) is the

primary contributor to the average node current, since the device continues to maintain BLE connectivity and execute firmware even in the absence of application-level data transmission.

In contrast, NBVLC and the E-ink display contribute through operation-specific current events superimposed on this BLE baseline. NBVLC transmission produces the highest instantaneous current spikes, but only for very short durations, resulting in a relatively small contribution to the cycle-averaged current. NBVLC reception shows only a modest increase above its idle level. These optical communication events are more clearly observed as incremental rises in branch currents (e.g., U7 and U9) during active operation rather than as dominant contributors to long-term consumption.

Similarly, the E-ink display (U2 branch) does not generate the highest peak current, but its comparatively long refresh duration (around 2.8 seconds) leads to a notable energy cost per event.

Overall, the main controller branch U1, which includes the BLE SoC, wake-up IC, and environmental sensor circuitry, dominates the cycle-averaged current consumption of the node, accounting for approximately 89–92% of the total, and up to ~93% during BLE-connected idle intervals in the evaluated test modes.

3.3 Node Optimization

3.3.1 Optimization of the E-ink display

First, in order to reduce the node's overall energy consumption, particular attention was given to the E-ink display operation. The display waveform Look-Up Table (LUT) in the firmware was refined by MPICOSYS to reduce the energy required during each refresh cycle.

For the initial unoptimized E-ink configuration, Figure 3.3.1(a) shows that an average current of approximately 1.37 mA was measured for about 2.8 s across measuring point U2 while the display was active. For the optimized low-power E-ink configuration, Figure 3.3.1(b) shows an average current of approximately 1.48 mA over only about 435 ms. Note that, in order to isolate the E-ink contribution, measuring points U7 and U9 were cut during this test.

Although the optimized waveform exhibits a slightly higher average current during the active refresh interval, this does not imply higher energy consumption. For an electronic paper display, a modest increase in active refresh current is physically plausible because faster particle motion generally requires more intensive drive power. In practice, LUT optimization can shorten the refresh process by modifying the waveform timing, for example through fewer phases, shorter update sequences, or voltage pulses designed to move the ink particles more rapidly. This is similar in principle to fast-refresh operating modes, where quicker transitions are achieved by reducing the time available for the particles to settle to their final high-contrast state [1]. As a result, the display may draw higher peak or average current during the active update interval, even though the total charge and energy consumed per refresh are substantially reduced because the update completes much faster. The trade-off is that such faster waveform operation may slightly degrade image quality, for example through increased ghosting or reduced contrast, but it provides a significant reduction in refresh time and hence in energy per update.

Since the display energy is determined by both the current magnitude and the refresh duration, it can be expressed as

$$E = V\int i(t)\,dt \approx VI_{\text{avg}}t, \tag{3.11}$$

where E is the energy consumed during one display refresh event, V is the supply voltage, $i(t)$ is the instantaneous display current, I_{avg} is the average current during the active refresh interval, and t is the refresh duration. Accordingly, a shorter refresh interval can yield significantly lower energy even when the average current is marginally higher. In this case, the refresh duration is reduced by about 84%, from approximately 2.8 s to 0.435 s. As a result, the display refresh energy decreases from 12.39 mJ to 2.13 mJ, corresponding to an overall reduction of approximately 83%.

Thus, the LUT optimization should be interpreted primarily as a time-domain energy reduction, rather than as a reduction in average current amplitude. The optimized waveform refreshes the display much more quickly, and this substantial reduction in active duration outweighs the short increase in average current, leading to significantly lower total energy consumption per update.

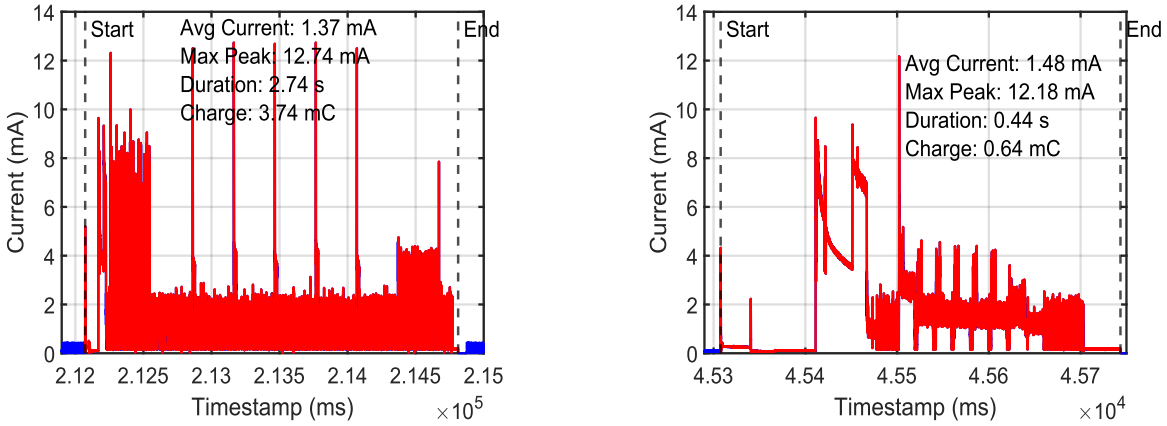

Figure 3.3.1. Current profiles for (a) Original E-ink display configuration, and (b) Optimized E-ink display configuration.

3.3.2 Firmware-level optimization through communication-functionality reconfiguration

The measurements reported in Sections 3.2.1 and 3.2.2 correspond to the original **full hybrid communication-modality firmware configuration**, in which both BLE and NBVLC uplink/downlink functions are enabled at the node. In that configuration, the node is capable of receiving commands from the gateway or access point through either BLE or NBVLC, and of transmitting data using either modality. Subsequent firmware analysis, however, showed that maintaining full NBVLC functionality—particularly the timer- and interrupt-driven support required for NBVLC downlink reception—introduces a non-negligible contribution to the baseline current consumption. Therefore, the lower-power configuration considered in the following subsection should not be interpreted as a purely software-only optimization applied to an otherwise unchanged functionality set. Rather, it reflects a combination of **firmware-level optimization** and **communication-mode reconfiguration**, in which the node is moved from a full hybrid communication configuration to a **partial hybrid communication configuration**. In this reduced configuration, BLE communication remains fully operational in both uplink and downlink, so the node can still receive commands from the gateway or access point via BLE, while NBVLC functionality is reduced to uplink transmission only. As a result, the node no longer processes incoming commands via NBVLC but can still use NBVLC uplink in a duty-cycled manner for data transmission when required. This distinction is important, as it explains why the optimized implementation can achieve substantially lower current consumption than the original full-functionality configuration.

3.3.2.1 NBVLC timer control for low-power operation

The NBVLC functionality is implemented in firmware using timers, interrupts, and Pulse Width Modulation (PWM) control. In particular, a timer-driven handler (*TimerHandler0*) manages the timing and modulation required for NBVLC communication according to the NEC protocol. This protocol uses a 32-bit frame composed of an 8-bit address field, an 8-bit command or data field, and their respective 8-bit complements, together with start-bit timing and error-checking logic. On the transmit side, an *nRF52* PWM instance is used to generate the modulated output waveform for the NBVLC transmitter. On the receive side, a dedicated reception handler monitors the timing of incoming pulses and interprets them according to the expected NEC frame structure. As a result, maintaining NBVLC functionality in the firmware requires periodic timer

activity and associated interrupt processing, even when NBVLC communication is not actively needed.

To manage this overhead, the firmware provides two control functions, *nbvlc_on()* and *nbvlc_off()* defined in Figure 3.3.2, which enable or suppress NBVLC-related timer activity. When NBVLC support is enabled, the timer invokes *TimerHandler0* at the configured interval so that PWM generation and protocol timing can be maintained. When *nbvlc_off()* is used, the timer interval is significantly increased, causing *TimerHandler0* to execute much less frequently. This reduces processor wake-ups and background firmware activity, thereby lowering the baseline current consumption and allowing the system to spend more time in low-power states. In practice, this approach is used to disable unnecessary NBVLC support activity in operating modes where the node remains connected via BLE and performs operations such as sensing and E-ink display updates but does not need NBVLC downlink reception.

For example, *nbvlc_off()* can be called inside the relevant switch-case routines, as shown in Figure 3.3.3, and also inside *void connect_callback(uint16_t conn_handle)*, as shown in Figure 3.3.4, so that NBVLC-related timer activity is suppressed whenever the node enters BLE-connected operation. The same principle can also be applied during BLE advertising. The corresponding energy benefits, achieved in the partial hybrid communication configuration where BLE uplink/downlink is retained and NBVLC is reduced to uplink only, are presented in Section 3.3.2.2.

```
void nbvlc_on() {
  ITimer0.setInterval(TIMER0_INTERVAL_MS / 10, TimerHandler0);
}

void nbvlc_off() {
  ITimer0.setInterval(TIMER0_INTERVAL_MS * 10, TimerHandler0);
}
```

Figure 3.3.2. *nbvlc_on()* and *nbvlc_off()* functions defined in firmware Arduino code.

```
if (Bluefruit.connected()) {
  //Test cases triggered by myChar write/update
  switch (char_m) {
    case 1:
    {
      Serial.println("Test mode #1 activated (eink and sensor test).");
      bme_setup();
      as_setup();
      nbvlc_off();
      char_m = 0;
      tm = 1;
      break;
    }
    case 3:
    {
      Serial.println("Test mode #3 activated (NBVLC rx and tx test).");
      char_m = 0;
      nbvlc_on();
      tm = 3;
      break;
    }
```

Figure 3.3.3. Part of the firmware Arduino code. "*nbvlc_off()*" is added to "case 1" in firmware code to obtain low current consumption over a periodic duty cycle, including sensing, E-ink display update and idle phases. Node is connected to a central device via BLE throughout the measurement interval.

```
void connect_callback(uint16_t conn_handle) {
  // Get the reference to current connection
  BLEConnection* connection = Bluefruit.Connection(conn_handle);
  char central_name[32] = { 0 };
  connection->getPeerName(central_name, sizeof(central_name));
  Serial.print("Connected to ");
  Serial.println(central_name);
  nbvlc_off();
}
```

Figure 3.3.4. Firmware Arduino code for BLE *connect_callback()* function.

3.3.2.2 *Low-power partial hybrid communication configuration: BLE uplink/downlink enabled, NBVLC uplink only*

To minimise power consumption, VLC functionality—particularly for downlink reception—is disabled at the firmware level, while BLE communication remains fully operational in both directions. Thus, the node will not be able to process incoming commands from the gateway or access point received via NBVLC. The NBVLC uplink, however, can still be utilized in a duty-cycled manner, whereby the NBVLC module is activated (using "*nbvlc_on()*") immediately prior to transmitting each NEC packet to a gateway or access point and deactivated (using "*nbvlc_off()*") immediately afterwards.

For a controlled comparison, both the **normal** configuration, corresponding to the **full hybrid communication configuration**, and the **low-power** configuration, corresponding to the **partial hybrid communication configuration**, follow the same operational cycle as shown in Figure 3.3.5, where the node maintains a BLE connection to a central device (e.g. gateway or access point), performs environmental sensing, updates the E-ink display, transmits uplink data via NBVLC, and remains idle between active periods. Although the node is capable of receiving downlink commands and transmitting uplink data through BLE, the present experiment considers a periodic duty-cycled scenario in which sensor data are transmitted periodically in the uplink via NBVLC uplink only.

The results in Figure 3.3.5 show that when the node operates in the low-power mode (i.e. partial hybrid communication configuration), the average current consumption is significantly reduced (by almost 62%) during an operation cycle—from 6.18 mA for the full hybrid communication configuration (Figure 3.3.5 (a)) to 2.36 mA (Figure 3.3.5 (b)). Further reductions are achieved by optimizing the E-ink display, lowering the average current to 2.20 mA (Figure 3.3.5(c)).

Given an operating voltage of 3.3 V, the energy consumption per cycle for the normal node operating mode (i.e. full hybrid communication configuration) is approximately 0.2257 J. For the low-power node operation (i.e. partial hybrid communication configuration), with the optimized E-ink display in use, the energy consumption drops to about 0.0615 J. This corresponds to a 73% reduction in energy consumption during an operation cycle involving sensing, E-ink display update, and NBVLC uplink transmission while the node remains connected via BLE.

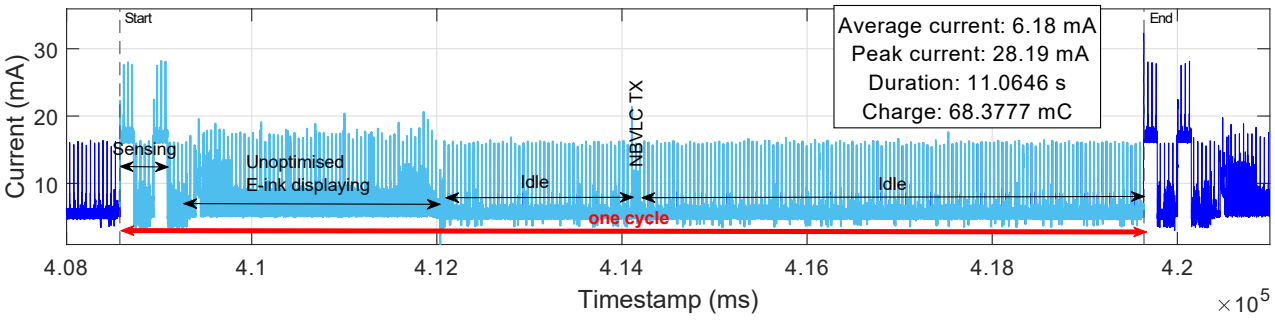

(a)

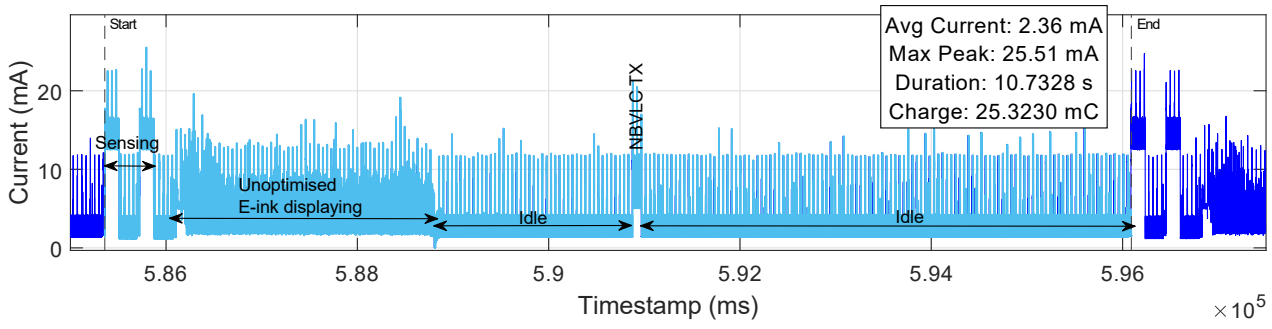

(b)

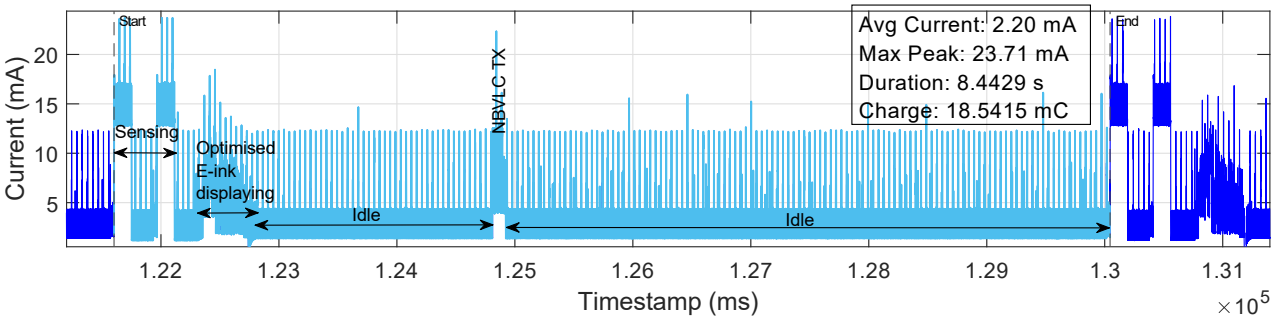

(c)

Figure 3.3.5. Current profile of node during: (a) Normal full hybrid communication configuration with unoptimized E-ink display, (b) Low-power partial hybrid communication configuration with unoptimized E-ink display, and (c) Low-power partial hybrid communication configuration with optimized E-ink display.

3.3.2.3 Further analysis of energy performance under normal full hybrid and low-power partial hybrid communication configurations

Table 3 shows the measured average current consumption of the BLE advertising interval, I_{advInt}, for different TX power levels (P_{tx}). A BLE advertising interval (T_{advInt}) of 152.5 ms is considered. Note that a BLE advertising interval (as illustrated in Figure 3.3.6(a)) is measured from the start of one advertising event to the start of the next (specification limit: 20 ms to 10.24 s). During BLE advertising events when the device is actively broadcasting its presence, higher transmit power levels result in higher average current consumption for the advertising event, I_{advEvent}. Idle current consumption between advertising events, I_{advIdle}, remains relatively constant across different TX power levels, as expected.

Similarly, Table 4 presents the measured average current consumption of the BLE connection interval, I_{connInt} for different TX power levels (P_{tx}). A BLE connection interval (T_{connInt}) of 45 ms is considered. The BLE connection interval (as illustrated in Figure 3.3.6(b)) is measured from the start of one connection event to the start of the next (specification limit: 7.5 ms to 4 s). A clear reduction in current is observed as the BLE TX power (P_{tx}) decreases from + 8 dBm to 0 dBm, indicating that lower transmission power substantially reduces the current drawn during active BLE connection events ($I_{\text{connEvent}}$). In contrast, the idle current (I_{connIdle}), measured between connection events, remains nearly constant, confirming that idle periods are unaffected by variations in TX power.

Table 3. Current draw as measured across nodes for different TX power levels during the BLE advertising state (BLE advertising interval, T_{advInt} = 152.5 ms).

P_{tx} **(dBm)**	I_{advInt} **(mA)**	I_{advIdle} **(mA)** (T_{advIdle}**=148.32 ms**)	I_{advEvent} **(mA)** (T_{advEvent} **=4.18 ms**)
	Normal (full hybrid communication configuration) / Low-power (partial hybrid communication configuration)		
+8	5.75 /1.59	5.48 / 1.32	15.78 / 11.62
+4	5.66 / 1.52	5.48 / 1.32	12.58 / 8.62
0	5.58 / 1.45	5.46 / 1.32	9.65 / 5.95

Table 4. Current draw as measured across nodes for different BLE TX power levels P_{tx} during BLE connected-only state (BLE connection interval, T_{connInt}=45 ms).

P_{tx} **(dBm)**	I_{connInt} **(mA)**	I_{connIdle} **(mA)** (T_{connIdle} **=42.86 ms)**	$I_{\text{connEvent}}$ **(mA)** ($T_{\text{connEvent}}$**=2.14 ms)**
	Normal (full hybrid communication configuration) / Low-power (partial hybrid communication configuration)		
+8	5.59 / 1.48	5.44 / 1.33	8.58 / 4.69
+4	5.56 / 1.46	5.43 / 1.33	8.12 / 4.20
0	5.51 / 1.43	5.43 / 1.33	7.31 / 3.52

(a) (b)

Figure 3.3.6. Illustration of the current profile of a single: (a) BLE advertising interval, (b) BLE connection interval.

Table 5 summarizes the average current consumption over a complete operational cycle that includes sensing, E-ink display updates, and idle phases. The measurements are presented for different BLE connection intervals (T_{connInt}) and transmission power levels (P_{tx}). In the table, T_{sens} denotes the average duration of a sensing operation, and I_{sens} represents the corresponding average current. Similarly, T_{eink} and I_{eink} refer to the duration and average current

of the E-ink display operations (both optimized and unoptimized), respectively. The parameters I_{idleSens} and I_{idleEink} denote the average current consumption during the idle periods following the sensing (T_{idleSens}) and E-ink display (T_{idleEink}) operations, respectively.

Table 5. Measured current consumption across the node for various BLE connection intervals and transmission power levels, comparing normal (full hybrid communication) and low-power (partial hybrid communication) modes during a full operational cycle that includes sensing, E-ink display, and idle phases.

		Average current consumption (mA) **Normal (full hybrid communication configuration) / Low-power (partial hybrid communication configuration)**				
T_{connInt} **(ms)**	P_{tx} **(dBm)**	I_{sens} **(T_{sens}= 516 ms)**	I_{idleSens} **(T_{idleSens} =200 ms)**	I_{eink} **(un-optimized) (T_{eink}=2.8 s)**	I_{eink} **(optimized) (T_{eink}=0.435 s)**	I_{idleEink} **(T_{idleEink}=7.5 s)**
11.25	+8	12.75 / 8.76	5.95 / 1.92	7.30 / 3.55	7.69 / 4.12	6.03 / 2.12
	+4	12.65 / 8.64	5.89 / 1.85	7.21 / 3.47	7.58 / 4.03	5.91 / 2.04
	0	12.55 / 8.52	5.79 / 1.71	7.12 / 3.32	7.45 / 3.93	5.84 / 1.90
45 (default)	+8	12.30 / 8.28	5.58 / 1.49	6.91 / 3.10	7.28 / 3.66	5.62 / 1.68
	+4	12.28 / 8.26	5.56 / 1.46	6.88 / 3.10	7.27 / 3.65	5.59 / 1.64
	0	12.26 / 8.23	5.50 / 1.43	6.84 / 3.09	7.24 / 3.63	5.56 / 1.63
250	+8	12.20 / 8.17	5.47 / 1.37	6.81 / 2.98	7.20 / 3.53	5.53 / 1.55
	+4	12.18 / 8.15	5.47 / 1.36	6.79 / 2.97	7.20 / 3.52	5.53 / 1.54
	0	12.17 / 8.14	5.47 / 1.35	6.78 / 2.96	7.19 / 3.52	5.50 / 1.54
1000	+8	12.13 / 8.13	5.45 / 1.35	6.76 / 2.95	7.19 / 3.50	5.50 / 1.53
	+4	12.12 / 8.13	5.45 / 1.33	6.76 / 2.95	7.17 / 3.50	5.50 / 1.53
	0	12.09 / 8.13	5.45 / 1.33	6.75 / 2.95	7.17 / 3.50	5.49 / 1.53

The results in Table 3, Table 4, and Table 5 further confirm that the partial hybrid communication configuration yields a consistent reduction in average current consumption of approximately 4 mA across the evaluated operating states. This reduction is particularly

significant in the context of energy-constrained IoT applications, especially those powered by energy harvesting sources such as indoor photovoltaics. In such systems, where available power is often in the microwatt to milliwatt range, even small reductions in average current can translate into substantial improvements in energy autonomy.

Moreover, the observed current savings are also beneficial for applications relying on flexible or printed electronics, where power budgets are typically constrained by the limitations of thin-film supercapacitors. The reduction in current draw directly supports more sustainable and longer-lasting operation of printed, ultra-low-power sensor nodes, thereby enhancing the viability of fully self-powered, maintenance-free wireless sensing platforms.

In summary, enabling continuous NBVLC listening for gateway or access-point commands introduces additional firmware processing overhead, mainly through timer- and interrupt-driven PWM control, which in turn increases the baseline current consumption. This overhead is more pronounced in the full hybrid configuration, where both NBVLC uplink and downlink operate alongside BLE communication. In contrast, the partial hybrid configuration reduces this overhead by selectively disabling NBVLC downlink reception, thereby lowering computational load and overall energy consumption while maintaining essential communication functionality. Basically, in this communication configuration, the node can only listen to commands from the gateway or access point via BLE only, while data can be transmitted in the uplink via either communication modalities.

The partial hybrid communication configuration is particularly advantageous in energy-constrained sensing applications where the node primarily performs periodic data acquisition and uplink reporting, while only occasional control or configuration commands are required from the gateway or access point. In such scenarios, BLE can provide the necessary connected-mode control and downlink support, while NBVLC can be retained only for uplink transmission. This reduces the persistent current overhead associated with maintaining full NBVLC functionality and is therefore well suited to harvesting-powered or duty-cycled node operation. By contrast, the full hybrid communication configuration remains preferable in use cases where both BLE and NBVLC uplink/downlink functions must be simultaneously available to maximise communication flexibility, redundancy, or modality selection at runtime.

3.3.3 Hardware optimization under disabled or reduced communication functionality

3.3.3.1 Very low-power node operation with both BLE and NBVLC disabled

In this section, a very-low-power firmware configuration is implemented, whereby the node periodically performs sensing, updates the measured values on the E-ink display, and then transitions into deep sleep after each update. In this operating mode, neither BLE nor NBVLC communication is enabled. To further minimise deep-sleep current, points U9 and U6 (refer to Figure 3.1.1) can be cut, as recommended in the initial node documentation provided by the project partner at UOULU. While U9 is used as a measurement point, U6 is not intended for current measurement; instead, it is opened to reduce standby current when the E-ink display is powered off. This modification reduces the quiescent power consumption during deep sleep by isolating the E-ink display power-control path from the always-on supply, thereby removing leakage current associated with that circuitry. Importantly, this change does not affect the main logic supply or the display-driving capability, and full E-ink refresh functionality is therefore preserved while achieving a lower standby current. Thus, we analysed the current consumption of the very low power firmware under the following four hardware optimization configurations:

(i) points U6 & U9 shorted (default hardware configuration).
(ii) point U6 cut only.
(iii) point U9 cut only.
(iv) both points U6 and U9 cut.

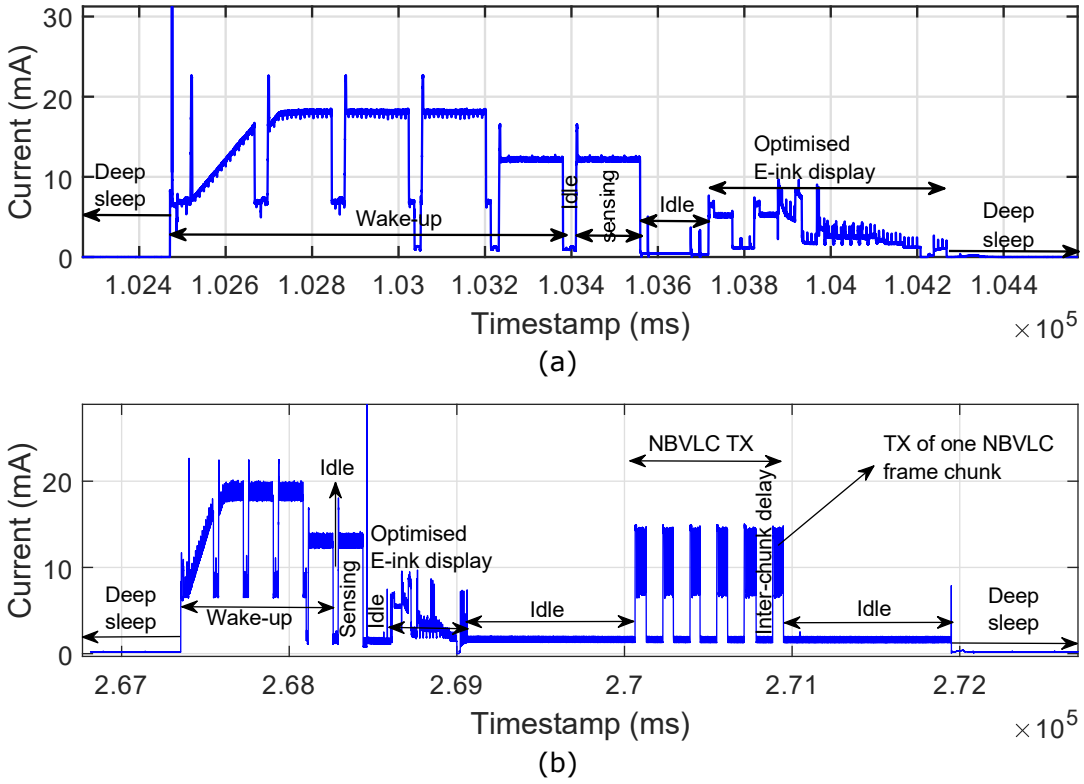

Figure 3.3.7. Current profile of the very low power firmware as measured across the node with: (a) BLE and NBVLC both disabled, and (b) BLE disabled and NBVLC uplink only enabled (U6 and U9 both cut).

Figure 3.3.7(a) illustrates the current profile of the node operating under the very low-power firmware configuration, with both U6 and U9 disconnected. Upon waking from deep sleep, the node immediately performs sensing and E-ink display operations. The corresponding average current consumption for each operation is detailed in Table 6.

Figure 3.3.8 shows the average current consumption of the node operating under the very low-power firmware configuration during the active (wakeup, sensing, E-ink display update, including any idle period between them) phase and deep sleep phases. The active phase lasts approximately 1.75 s when using the optimized E-ink configuration and extends to about 4.05 s with the unoptimized variant. Following this phase, the node enters a deep sleep state for approximately 1:16.1 minutes.

Considering Figure 3.3.8(a), the average current remains consistent at 9.6 mA when both U6 and U9 are shorted by default or when only U6 is cut. A marginal reduction (about 4%) is observed when U9 is cut alone or in combination with U6, indicating that cutting U6 has negligible effect on active-phase current consumption. However, the impact is more pronounced during the deep sleep phase. Cutting either U6, U9, or both significantly reduces the deep sleep current—from approximately 416 µA to just 5 µA—reflecting a ~99% reduction. This demonstrates the substantial energy-saving potential of these hardware modifications.

Thus, we can conclude that disabling the communication modules while allowing the node to remain active for only a brief period before entering a prolonged deep sleep mode significantly reduces the overall energy consumption of the Si-based node. These optimizations directly target the sleep currents of peripheral components: cutting U9 disables the NBVLC receiver circuit by isolating it from the main VDD rail, while cutting U6 affects the E-ink display's standby current. To re-enable the NBVLC receiver during normal operation, a 0 Ω resistor can be soldered in place, allowing power to be supplied via a dedicated nRF52833 General-Purpose Input/Output

(GPIO) pin. This pin can be toggled HIGH to activate the receiver and set LOW to power it down during sleep, thereby improving energy efficiency.

Finally, Figure 3.3.9 shows that reducing the E-ink display's refresh duration further lowers the overall average current consumption under all tested hardware configurations, underscoring the combined benefits of communication modality selection, hardware- and firmware-level optimizations.

Table 6. Average current consumption measured for each operation when the node operates under a very low-power firmware configuration with both NBVLC and BLE disabled.

	Node operations in a cycle (duration)	**Average current across node (mA)**			
		U6 and U9 shorted	**U6 cut only**	**U9 cut only**	**Both U6 and U9 cut**
Active phase node operations	Wakeup (~909 ms)	14.2	14.2	13.9	13.9
	Idle between wake-up and sensing (~30 ms)	1.34	1.34	1.02	1.02
	Sensing (~149 ms)	12.5	12.5	12.2	12.2
	Idle between sensing and E-ink display (~116 ms)	0.843	0.843	0.435	0.435
	Optimized E-ink display (~544 ms) / Unoptimized E-ink display (~2.8 s)	3.33 / 2.72	3.33 / 2.72	2.97 / 2.37	2.97 / 2.37
Average current during active phase with: optimised E-ink / un-optimised E-ink		**9.6 / 5.6**	**9.6 / 5.6**	**9.2 / 5.3**	**9.2 / 5.3**
Deep sleep after E-ink display (1:16.1 min)		0.416	0.344	0.0754	0.0047

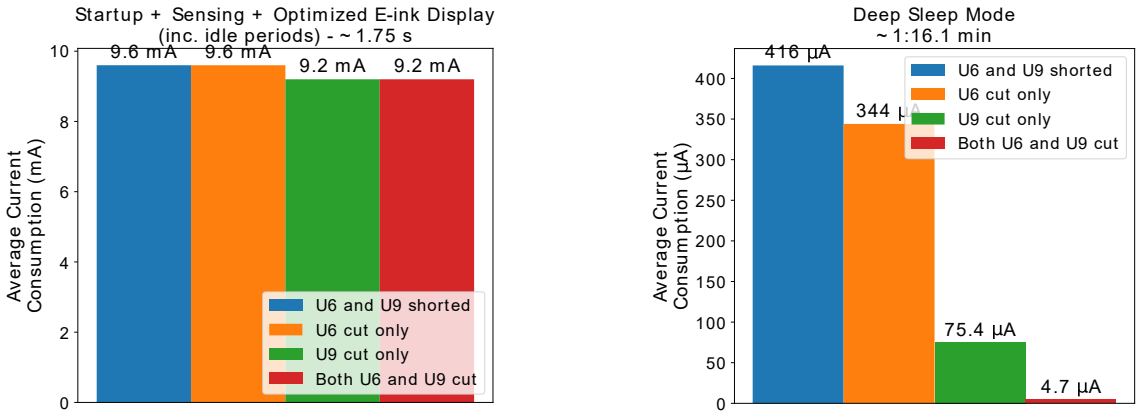

(a) (b)

Figure 3.3.8. Average current consumption of the node running very low power firmware (BLE and NBVLC both turned off) during: (a) active phase, (b) deep sleep phase.

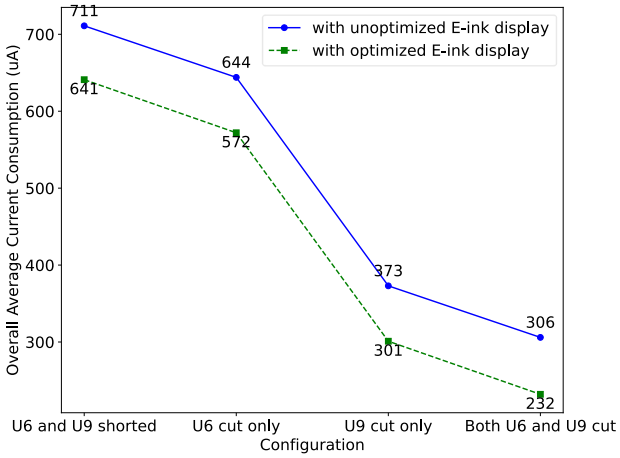

Figure 3.3.9. Overall average current consumption of the node running very low power firmware (BLE and NBVLC both disabled) over one duty cycle consisting of both the active and deep sleep phases.

3.3.3.2 Very low-power node operation with BLE OFF and NBVLC uplink ON

This operational mode is similar to that described in Section 3.3.3.1 with the addition of NBVLC uplink transmission during the active phase, as illustrated in Figure 3.3.7(b). The BLE module remained disabled throughout this experiment. Compared to the profile in Figure 3.3.7(a), an additional idle period of approximately 1 s was inserted after the E-ink display update and NBVLC transmission phase. The measured average current for each operation is summarized in Table 7.

This scenario simulates periodic node activity, where the device awakens to perform sensing, update the E-ink display, and transmit environmental data from the BME688 sensor (e.g., temperature, humidity, pressure, and gas resistance) to a gateway or access point using NBVLC. The sensor data, referred to as the payload, are transmitted using a custom NBVLC frame structure comprising 23 bytes and segmented into multiple 32-bit chunks. Each frame includes key fields such as source and destination addresses, synchronization markers (start and end), payload (e.g. sensor readings, location coordinates or both), payload type and size, and a checksum to ensure data integrity.

In the current profile in Figure 3.3.7(b), the NBVLC uplink transmission is visible as six discrete bursts (chunks), each corresponding to a 32-bit NEC packet. To facilitate accurate decoding at the receiver (e.g., the gateway or access point), 100 ms inter-chunk delays are incorporated, providing the decoder sufficient time to validate and process each segment of the transmitted NBVLC frame, and extract the relevant useful information.

Similar to the observations in Table 6, Table 7 shows that the overall average current consumption decreases when either U6, U9, or both are cut. However, unlike the previous case, the deep sleep current is notably higher when only U9 is cut or when both U6 and U9 are cut. This increase is attributed to the added computational load introduced by the NBVLC functions in the firmware, which likely requires increased CPU activity and tighter coordination between subsystems, thereby elevating energy usage.

Furthermore, the idle intervals surrounding the NBVLC transmission phase (as illustrated in Figure 3.3.7(b) and detailed in Table 7) exhibit relatively high current draw. This highlights the importance of carefully managing these idle periods to optimize overall energy efficiency.

Table 7. Average current measured across the node for each operation with NBVLC uplink transmission enabled under the very low-power firmware (BLE disabled).

	Node operations in a cycle	**Average current across node (mA)**			
		U6 and U9 shorted	**U6 cut only**	**U9 cut only**	**Both U6 and U9 cut**
Active phase node operations	Wakeup (~911 ms)	14.2	14.2	14.0	14.0
	Idle between wakeup and sensing (~30 ms)	1.67	1.48	1.6	1.34
	Sensing (~149 ms)	12.9	12.72	12.75	12.54
	Idle between sensing and E-ink display (~165 ms)	1.35	1.53	1.21	1.37
	Optimized E-ink display (~0.45 s) / Unoptimized E-ink display (~2.8 s)	3.51 / 2.80	3.47 / 2.80	3.18 / 2.63	3.32 / 2.63
	Idle between E-ink display and NBVLC TX (~1 s), Inter-chunk delay (~100 ms), Idle after NBVLC TX	1.5	1.5	1.4	1.4
	Each NBVLC TX chunk (~68 ms)	10.7	10.7	10.2	10.2
Deep sleep after NBVLC TX (1:12.7 min)		0.416	0.344	0.271	0.202
Overall average current consumption (mA) during one cycle (with optimized E-ink / with unoptimized E-ink)		**0.711 / 0.776**	**0.639 / 0.710**	**0.563 / 0.629**	**0.496 / 0.564**

3.4 RIoT Node Energy Models

In this section, we present comprehensive analytical energy models for predicting the energy consumption of the Si-based RIoT node over its operational period. The models account for all relevant phases of operation, including initial BLE communication (advertising and connected modes), firmware start-up sequences, cyclic sensing, E-ink display updates, and data-transmission tasks. The total energy consumption is obtained by considering the current draw and duration of each phase, thereby providing a detailed breakdown of energy usage across the different node activities. Three predictive analytical energy models were developed for the following Si-based RIoT node operating modes:

- **Normal node operation** (full hybrid communication configuration)
- **Low-power node operation** (partial hybrid communication configuration)
- **Very-low-power node operation with hardware optimization considerations** (for communication configurations with either both BLE and NBVLC disabled, or BLE disabled and NBVLC uplink only enabled)

3.4.1 Normal (full hybrid communication) and low-power (partial hybrid communication) node operations

As described in Section 3.3.2, the **full hybrid communication configuration** refers to an operating mode in which both BLE and NBVLC uplink and downlink functions are enabled at the node. In this configuration, the node can receive commands from a gateway or access point via either BLE or NBVLC and can also transmit the requested data using either communication modality. By contrast, the **partial hybrid communication configuration** refers to an operating mode in which BLE uplink and downlink remain enabled, while NBVLC functionality is limited to uplink transmission only.

To get an insight into the energy consumption of the node under these two operating modes, let's consider the following scenario for the node operation:

(i) The node is powered on and starts BLE advertising in fast mode (default fast advertising interval=20 ms). The default BLE TX power level is 0 dBm during BLE advertising and BLE-connected states.
(ii) The timeout for the fast mode BLE advertising is set to 30 s.
(iii) No central device (e.g. gateway or access point) is connected to the node while advertising in fast mode.
(iv) Therefore, the node switches to slow BLE advertising mode (default slow advertising interval=152.5 ms)
(v) A central device (e.g. gateway or access point) connects to the node 30 s after it started slow BLE advertising, with a default BLE connection interval of 45 ms.
(vi) The node remains in BLE-connected mode with the central device for another 30 s (idle).
(vii) A central device subsequently connects to the node via BLE and issues a BLE command by writing to the node's BLE characteristics value. This command triggers the execution of a predefined mode, which includes initializing the BME688 sensor (henceforth referred to as wakeup or startup), performing sensing operations, refreshing the E-ink display, and transmitting data via either NBVLC or BLE in a duty-cycled fashion, as illustrated in Figure 3.4.1.

The initial operations include BLE advertising in both fast and slow modes, BLE-connected idle operation, BLE command reception from the gateway or access point, idle operation after BLE downlink reception, startup, and idle operation after startup. The operations that form the recurring duty cycle of the node are sensing, idle after sensing, E-ink display update, idle after the E-ink update, NBVLC or BLE uplink transmission, and idle after NBVLC or BLE transmission.

The energy model for this scenario can be formulated as follows:

1. Charge consumption during BLE advertising intervals (fast and slow):

The average current consumption for a BLE advertising interval (fast or slow) can be written as follows:

$$I_{\text{advInt}} = \frac{(I_{\text{advEvent}} \times T_{\text{advEvent}}) + (I_{\text{advIdle}} \times T_{\text{advIdle}})}{T_{\text{advEvent}} + T_{\text{advIdle}}}, \quad (3.12)$$

where I_{advEvent} is the average current consumed during an advertising event, T_{advEvent} is the average duration of a single advertising event, I_{advIdle} is the average current consumed during the idle portion between two successive advertising events, and T_{advIdle} is the average duration of the idle period between two successive advertising events ($T_{\text{advIdle}} = T_{\text{slowAdvIdle}}$ for slow BLE advertising mode or $T_{\text{advIdle}} = T_{\text{fastAdvIdle}}$ for fast BLE advertising mode). In our case, the fast and slow advertising modes correspond to a default advertising interval of 20 ms and 152.5 ms, respectively. The measured average current consumption of the BLE advertising interval, I_{advInt}, for different TX power levels (P_{tx}) were reported in Table 3. The total charge consumption (in mAh) for fast advertising intervals is given by:

$$Q_{\text{fastAdvInt}} = I_{\text{fastAdvInt}} \times T_{\text{fastAdvInt}} \times N_{\text{fastAdv}}, \quad (3.13)$$

where $T_{\text{fastAdvInt}}$ is the duration of a fast BLE advertising interval (in hours), and N_{fastAdv} is the number of fast BLE advertising intervals over a given period, which can be computed as

$$N_{\text{fastAdv}} = T_{\text{fastAdv}}/T_{\text{fastAdvInt}}, \tag{3.14}$$

where T_{fastAdv} is the duration for which the node advertises in fast mode during the initial operations. Similarly, the total charge consumption (in mAh) for slow advertising intervals is given by:

$$Q_{\text{slowAdvInt}} = I_{\text{slowAdvInt}} \times T_{\text{slowAdvInt}} \times N_{\text{slowAdv}}, \tag{3.15}$$

where $T_{\text{slowAdvInt}}$ is the duration of a slow BLE advertising interval (in hours), and N_{slowAdv} is the number of slow BLE advertising intervals over a given period, which can be computed as

$$N_{\text{slowAdv}} = T_{\text{slowAdv}} \,/\, T_{\text{slowAdvInt}}, \tag{3.16}$$

where T_{slowAdv} is the duration for which the node advertises in slow mode during the initial operations.

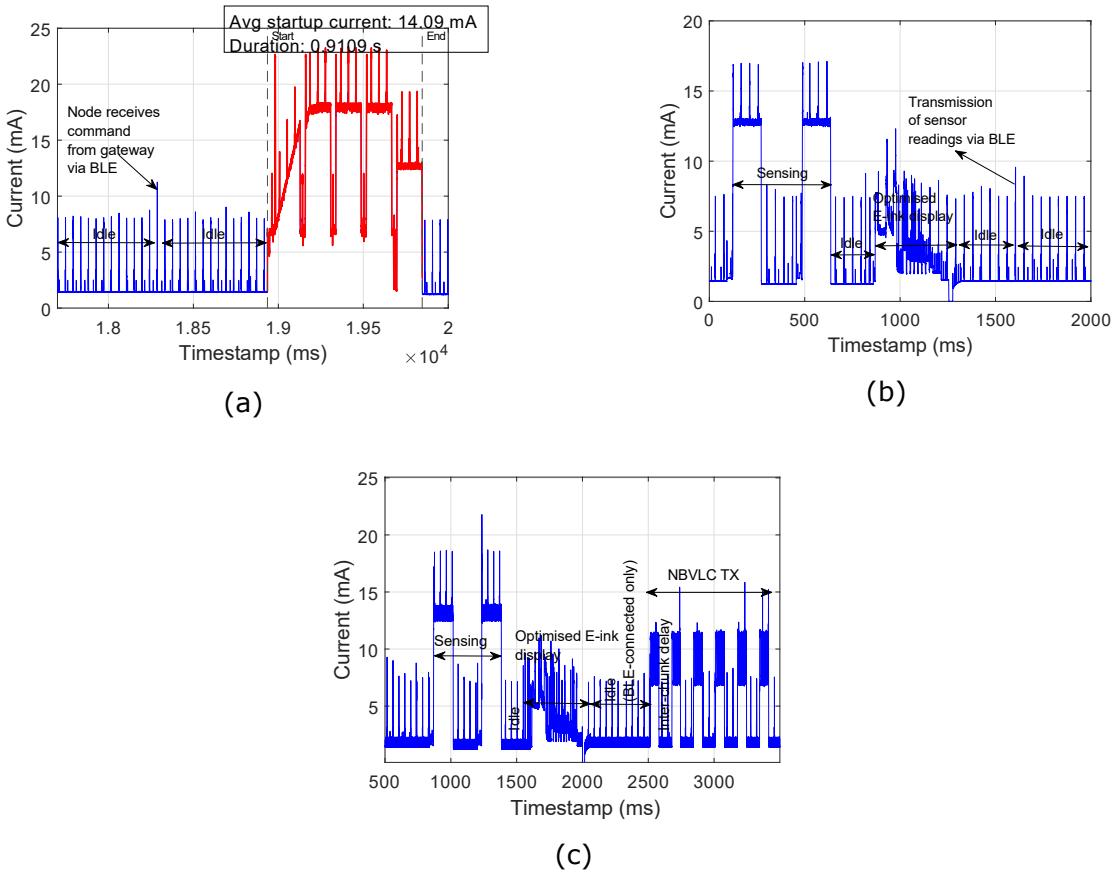

Figure 3.4.1. Illustration of current profiles when node is: (a) receiving BLE command and performing BME688 sensor initialization (wakeup/startup), (b) performing sensing, E-ink display update and transmission of sensor readings via BLE, and (c) performing sensing, E-ink display update and transmission of sensor readings via NBVLC.

2. Charge consumption during BLE connection intervals:

The average current consumption during a BLE connection interval is obtained as follows:

$$I_{\text{connInt}} = \frac{(I_{\text{connEvent}} \times T_{\text{connEvent}}) + (I_{\text{connIdle}} \times T_{\text{connIdle}})}{T_{\text{connEvent}} + T_{\text{connIdle}}}, \tag{3.17}$$

where $T_{\text{connEvent}}$ is the average duration of a single BLE connection event, $I_{\text{connEvent}}$ is the average current consumed during a BLE connection event, T_{connIdle} is the idle period between two successive BLE connection events and I_{connIdle} is the average current consumed during the idle period between two successive BLE connection events. The measured average current consumption of the BLE connection interval, I_{connInt}, for different TX power levels (P_{tx}) were reported in Table 4. The total charge consumption (in mAh) for BLE connection intervals is given by:

$$Q_{\text{connInt}} = I_{\text{connInt}} \times T_{\text{connInt}} \times N_{\text{connInt}} \text{ ,} \quad (3.18)$$

where T_{connInt} is the duration of a BLE connection interval (in hours), and N_{connInt} is the number of instances of the BLE connection intervals over a given period of time during the initial operations, and it can be computed as:

$$N_{\text{connInt}} = T_{\text{bleConn}} / T_{\text{connInt}} \text{ ,} \quad (3.19)$$

where T_{bleConn} is the time spent in BLE-connected only mode during the initial operations.

3. Charge consumption during the reception of a BLE command:

After a gateway or access point connects via BLE to the node, the latter receives a command via BLE, which will subsequently initialize the BME688 sensor and activate different operations on the node in a periodic duty-cycle manner. The charge consumption (in mAh) during the reception of a BLE command is calculated as follows:

$$Q_{\text{bleCmdRx}} = I_{\text{bleCmdRx}} \times T_{\text{bleCmdRx}} \text{ ,} \quad (3.20)$$

where T_{bleCmdRx} is the duration of the BLE command in hours, and I_{bleCmdRx} is the average current consumed during the reception of a BLE command by the node (in mA). In Figure 3.4.1(a), the reception of a BLE command occurs over a period of approximately 2.33 ms, during which the current consumption varies between 7.36 mA at 0 dBm and 7.89 mA at +8 dBm for the normal node operation and between 4.2 mA (0 dBm) and 4.79 mA (8 dBm) for the low-power node operation, depending on the transmission power level of the central device. If we consider a default BLE connection interval of 45 ms, BLE TX power level of 0 dBm, and a 3.3 V operating voltage, the energy per BLE downlink command for the low-power operating mode is approximately 32 μJ. This represents a reduction of roughly 44% relative to the normal mode, where the corresponding energy consumption is about 57 μJ considering the same parameters.

4. Charge consumption during sensor initialization (startup):

The BME688 initialization is typically performed only once, for example, immediately after the node powers on and it receives a gateway-issued command to begin duty-cycled operations that include environmental sensing (as illustrated in Figure 3.4.1(a)). The charge consumption (in mAh) during the startup activity is calculated as follows:

$$Q_{\text{start}} = I_{\text{start}} \times T_{\text{start}} \text{ ,} \quad (3.21)$$

where T_{start} is the average startup duration in hours, and I_{start} is the average current consumed during the startup period (in mA). The initialization phase of the environmental sensor is relatively energy intensive, lasting approximately 916 ms and drawing an average current of about 14-15 mA.

5. Charge consumption during sensing:

The total charge consumed during the sensing operations (in mAh) can be formulated as:

$$Q_{\text{sens}} = I_{\text{sens}} \times T_{\text{sens}} \times N_{\text{sens}}, \quad (3.22)$$

where T_{sens} is the average duration of a single sensing operation (in hours, h), I_{sens} is the average current consumed during a sensing operation (in mA), and N_{sens} is the number of instances of the sensing operations over the node's operating duration.

6. Charge consumption during E-ink display:

The total charge consumed during the E-ink displaying operations (in mAh) can be expressed as:

$$Q_{\text{eink}} = I_{\text{eink}} \times T_{\text{eink}} \times N_{\text{eink}} \ , \tag{3.23}$$

where T_{eink} is the average duration of a single E-ink displaying operation (in hours, h), I_{eink} is the average current consumed during the E-ink displaying operation (in mA), and N_{eink} is the number of instances of the E-ink displaying operations over the node's operating duration.

Table 5 reported the measured average current consumption during a complete sensing and E-ink displaying cycle—including associated idle periods—under varying BLE connection intervals (T_{connInt}) and transmission power levels (P_{tx}) for both the normal (full hybrid communication configuration) and low-power (partial hybrid communication configuration) operating modes.

7. Charge consumption during BLE data TX:

An illustrative current profile corresponding to the uplink transmission of sensor data, along with sensing and optimized E-ink display operations, is presented in Figure 3.4.1(b). The data is sent as a 116-byte JSON string containing the Source ID, Destination ID, and sensor measurements such as temperature, humidity, pressure, and gas concentrations, and dummy location coordinates (X, Y, Z). The BLE link operates with a 2 Mbps PHY data rate, a Maximum Transmission Unit (MTU) of 247 bytes, a connection interval (T_{connInt}) of 45 ms, and a transmission power (P_{tx}) of 0 dBm. BLE uplink transmissions from the node to the gateway or access point are very brief, lasting approximately 3.13 ms, with current draw ranging from 9.10 mA at 0 dBm to 13.41 mA at +8 dBm for the normal operating mode and between 5.91 mA at 0 dBm to 10.18 mA at +8 dBm for the low-power operating mode. Assuming a 45 ms BLE connection interval, a BLE transmit power of 0 dBm, and a 3.3 V operating voltage, the energy required for each BLE uplink transmission is approximately 61 µJ for the low-power node operation—corresponding to a reduction of about 35% compared to the normal-mode operation.

The total charge consumed during the uplink BLE transmission (in mAh) can be estimated using the expression:

$$Q_{\text{bleTx}} = I_{\text{bleTx}} \times T_{\text{bleTx}} \times N_{\text{bleTx}}, \tag{3.24}$$

where I_{bleTx} denotes the average current during a single BLE transmission (in mA), T_{bleTx} is the average duration of one BLE uplink transmission (in hours), and N_{bleTx} represents the number of such transmission events over the node's operational lifetime.

8. Charge consumption during NBVLC data TX:

In this scenario, we evaluate the case where the RIoT node transmits a payload in the uplink using the NBVLC interface while maintaining a BLE connection with a central device. The sensor and dummy location payload are encapsulated within a 23-byte NBVLC frame, which is transmitted as six sequential 32-bit NEC packets (frame chunks). This transmission behavior is clearly reflected in the current profile shown in Figure 3.4.1(c), where each chunk is separated by an inter-chunk delay of 100 ms.

Under both the normal and low-power operating modes, BLE is considerably more energy-efficient than NBVLC for uplink data transmission when a BLE connection is already established. In the normal configuration, assuming a BLE connection interval of 45 ms, a TX power of 0 dBm, and a supply voltage of 3.3 V, a BLE uplink transmission requires approximately 94 µJ, based on a measured current of 9.10 mA over 3.13 ms. By comparison, transmitting the same data via NBVLC uplink, segmented into six chunks while maintaining the BLE connection, requires

about 21.5 mJ, corresponding to an average current of 7.17 mA over 0.91 s. In the low-power configuration, the BLE uplink energy reduces further to approximately 61 μJ, based on a measured current of 5.91 mA over 3.13 ms, whereas the corresponding NBVLC uplink energy is still much higher, at about 15 mJ, with an average current of 4.9 mA over 0.91 s. These results show that the large energy gap is primarily due to the much shorter transmission duration of BLE, enabled by its higher effective data rate. Nevertheless, NBVLC remains a useful alternative in scenarios where RF operation is constrained or undesirable, such as environments containing sensitive medical equipment.

The total charge consumed during the NBVLC transmission and reception operations (in mAh) can be expressed as:

$$Q_{\mathrm{nbvlc}} = I_{\mathrm{nbvlc}} \times T_{\mathrm{nbvlc}} \times N_{\mathrm{nbvlc}} \ , \tag{3.25}$$

where T_{nbvlc} is the average duration of a single NBVLC transmission event (in hours), I_{nbvlc} represents the average current drawn during the transmission (in mA), and N_{nbvlc} is the total number of NBVLC transmission instances over the node's operational lifetime. For a single NBVLC transmission composed of multiple chunks and interleaved delays, the average duration is derived as follows:

$$T_{\mathrm{nbvlc}} = (N_{\mathrm{c}} \times T_{\mathrm{c}}) + (N_{\mathrm{c}} - 1) \times T_{\mathrm{d}} \ , \tag{3.26}$$

where N_{c} is the number of NBVLC transmission chunks, T_{c} is the duration of each transmission chunk, and T_{d} is the duration of the inter-chunk delay. The average current during an NBVLC transmission operation, I_{nbvlc}, is computed using a weighted average of the current during the transmission chunks and the inter-chunk delays, and is formulated as follows:

$$I_{\mathrm{nbvlc}} = \frac{(N_{\mathrm{c}} \times I_{\mathrm{ctx}} \times T_{\mathrm{c}}) + (N_{\mathrm{c}} - 1) \times I_{\mathrm{d}} \times T_{\mathrm{d}}}{T_{\mathrm{nbvlc}}} \ , \tag{3.27}$$

where I_{ctx} is the average current of one NBVLC chunk, and I_{d} is the average inter-chunk delay current.

9. Charge consumption during idle periods:

The idle state refers to periods during which the node remains connected to a central device (e.g., a gateway or access point) via BLE, but no active operations such as sensing, data transmission, or display updates are performed. These states are illustrated in Figure 3.4.1. The total charge consumption during idle periods (in mAh) can be computed using:

$$Q_{\mathrm{idle}} = I_{\mathrm{idle}} \times T_{\mathrm{idle}}, \tag{3.28}$$

where T_{idle} denotes the average duration of an idle period (in hours), and I_{idle} is the average current drawn during the idle period (in mA).

For idle states following specific operations, such as BLE command RX, startup or sensing, the average current—denoted as $I_{\mathrm{idleBleCmdRx}}$, $I_{\mathrm{idleStart}}$ and I_{idleSens}, respectively—corresponds to the average current consumption during a BLE connection interval, I_{connInt}, as computed in Eq. (3.17).

Analysis of the measurement results for the normal operating mode in Table 5, considering a BLE connection interval of 45 ms, shows that the average idle current following the E-ink display is only slightly higher than the BLE-connected-only baseline reported in Table 4. The increase is approximately 0.5%–0.9%, and can therefore be approximated by an average increase of about 0.7%. This applies to idle intervals occurring after the E-ink update, including cases where NBVLC or BLE uplink transmission is scheduled immediately afterwards, as well as subsequent idle periods within the same duty cycle, such as NBVLC inter-chunk delays, as illustrated in Figure 3.4.1(b) and Figure 3.4.1(c). Accordingly, for the normal operating mode,

$$I_{\text{idleEink}} \approx 1.007 \times I_{\text{connInt}} \,. \tag{3.29}$$

By contrast, under the low-power node operating mode, the idle current following the E-ink display is more noticeably elevated. From the comparison of Table 4 and Table 5, again for a BLE connection interval of 45 ms, this current is on average about 14% higher than I_{connInt} across the considered BLE transmission power levels. Hence, for the low-power node operation,

$$I_{\text{idleEink}} \approx 1.14 \times I_{\text{connInt}} \,. \tag{3.30}$$

The node's duty-cycled operation comprises a sequence of recurring tasks, including sensing, E-ink display updates, data uplink transmission, and idle periods that follow these operations. We prioritize BLE-based uplink data transmission over NBVLC, as prior analysis has demonstrated that leveraging an already-established BLE connection yields greater energy efficiency compared to initiating NBVLC transmission for the same payload. Therefore, in the following formulations and energy consumption models, we assume that sensor and dummy location data are transmitted via BLE. Thus, the duration of a full cycle can be expressed as:

$$T_{\text{oneFullCycle}} = T_{\text{sens}} + T_{\text{idleSens}} + T_{\text{eink}} + T_{\text{idleEink}} + T_{\text{bleTx}} + T_{\text{idleBleTx}} \,, \tag{3.31}$$

where T_{idleSens}, T_{idleEink}, and $T_{\text{idleBleTx}}$ denote the durations of the idle periods that immediately follow the sensing, E-ink display update, and BLE transmission operations, respectively.

Conversely, the durations associated with the initial set of operations (T_{initOper})—comprising BLE fast (T_{fastAdv}) and slow (T_{slowAdv}) advertising, the BLE connected-only (idle) state (T_{bleConn}), reception of BLE commands from the gateway (T_{bleCmdRx}), the subsequent idle period ($T_{\text{idleBleCmdRx}}$), sensor initialization/startup (T_{start}), and the idle period following startup ($T_{\text{idleStart}}$)—can be collectively expressed as:

$$T_{\text{initOper}} = T_{\text{fastAdv}} + T_{\text{slowAdv}} + T_{\text{bleConn}} + T_{\text{bleCmdRx}} + T_{\text{idleBleCmdRx}} + T_{\text{start}} + T_{\text{idleStart}}. \tag{3.32}$$

Accordingly, the total number of operational cycles that the node can execute over its operating duration can be determined as:

$$N_{\text{cycles}} = \frac{(T - T_{\text{initOper}})}{T_{\text{oneFullCycle}}}, \tag{3.33}$$

where T is the total operating duration of the node. The number of full cycles over the node's operating time can then be expressed as:

$$N_{\text{fullCycles}} = \lfloor N_{\text{cycles}} \rfloor. \tag{3.34}$$

The total duration of the full cycles is then computed as:

$$T_{\text{fullCycles}} = N_{\text{fullCycles}} \times T_{\text{oneFullCycle}}. \tag{3.35}$$

In the event that there are both $N_{\text{fullCycles}}$ full cycles and also a partial cycle, we need to determine which operations will fit entirely within the partial cycle, which operations will only fit partially, and which operations will not fit at all. These need to be accounted for in the total charge consumption. The partial cycle duration can be computed as

$$T_{\text{partCycle}} = (T - T_{\text{initOper}}) - T_{\text{fullCycles}}. \tag{3.36}$$

To compute the charge consumed over a partial cycle of duration $T_{\text{partCycle}}$, we assume that the node follows the same ordered sequence of operations as in the nominal full duty cycle, but the cycle is truncated before completion. Thus, $T_{\text{partCycle}}$ may end at any point within the cycle, i.e.,

during sensing, idle after sensing, E-ink update, idle after E-ink, BLE transmission, or idle after BLE transmission. Accordingly, the charge consumed over the partial cycle is obtained by summing the contributions of all fully completed operations and the partial contribution of the operation active at time $T_{\text{partCycle}}$.

For the considered case, the nominal cycle consists of the following sequential operations:

sensing → idle after sensing → E-ink display → idle after E-ink → BLE TX → idle after BLE TX.

Let

$$T_{\text{s}} = T_{\text{sens}}, T_{\text{i1}} = T_{\text{idleSens}}, T_{\text{e}} = T_{\text{eink}}, T_{\text{i2}} = T_{\text{idleEink}}, T_{\text{b}} = T_{\text{bleTx}}, T_{\text{i3}} = T_{\text{idleBleTx}},$$

and let the corresponding average currents be

$$I_{\text{s}} = I_{\text{sens}}, I_{\text{i1}} = I_{\text{idleSens}}, I_{\text{e}} = I_{\text{eink}}, I_{\text{i2}} = I_{\text{idleEink}}, I_{\text{b}} = I_{\text{bleTx}}, I_{\text{i3}} = I_{\text{idleBleTx}}.$$

Here,

$$I_{\text{i1}} \approx I_{\text{connInt}},$$

while, for the normal operating mode,

$$I_{\text{i2}} \approx 1.007\, I_{\text{connInt}}, \qquad I_{\text{i3}} \approx 1.007\, I_{\text{connInt}},$$

and, for the low-power operating mode,

$$I_{\text{i2}} \approx 1.14\, I_{\text{connInt}}, \qquad I_{\text{i3}} \approx 1.14\, I_{\text{connInt}}.$$

The nominal full-cycle duration is therefore

$$T_{\text{oneFullCycle}} = T_{\text{s}} + T_{\text{i1}} + T_{\text{e}} + T_{\text{i2}} + T_{\text{b}} + T_{\text{i3}}, \tag{3.37}$$

and the partial-cycle duration satisfies

$$0 \le T_{\text{partCycle}} < T_{\text{oneFullCycle}}. \tag{3.38}$$

Next, we define the cumulative time boundaries as

$$\tau_1 = T_{\text{s}}, \qquad \tau_2 = T_{\text{s}} + T_{\text{i1}}, \qquad \tau_3 = T_{\text{s}} + T_{\text{i1}} + T_{\text{e}},$$
$$\tau_4 = T_{\text{s}} + T_{\text{i1}} + T_{\text{e}} + T_{\text{i2}}, \qquad \tau_5 = T_{\text{s}} + T_{\text{i1}} + T_{\text{e}} + T_{\text{i2}} + T_{\text{b}}.$$

With these definitions, the charge consumed over the partial cycle can be written as

$$Q_{\text{partial}} = \begin{cases} I_{\text{s}}\, T_{\text{partCycle}}, & 0 \le T_{\text{partCycle}} \le \tau_1, \\ I_{\text{s}} T_{\text{s}} + I_{\text{i1}}(T_{\text{partCycle}} - \tau_1), & \tau_1 < T_{\text{partCycle}} \le \tau_2, \\ I_{\text{s}} T_{\text{s}} + I_{\text{i1}} T_{\text{i1}} + I_{\text{e}}(T_{\text{partCycle}} - \tau_2), & \tau_2 < T_{\text{partCycle}} \le \tau_3, \\ I_{\text{s}} T_{\text{s}} + I_{\text{i1}} T_{\text{i1}} + I_{\text{e}} T_{\text{e}} + I_{\text{i2}}(T_{\text{partCycle}} - \tau_3), & \tau_3 < T_{\text{partCycle}} \le \tau_4, \\ I_{\text{s}} T_{\text{s}} + I_{\text{i1}} T_{\text{i1}} + I_{\text{e}} T_{\text{e}} + I_{\text{i2}} T_{\text{i2}} + I_{\text{b}}(T_{\text{partCycle}} - \tau_4), & \tau_4 < T_{\text{partCycle}} \le \tau_5, \\ I_{\text{s}} T_{\text{s}} + I_{\text{i1}} T_{\text{i1}} + I_{\text{e}} T_{\text{e}} + I_{\text{i2}} T_{\text{i2}} + I_{\text{b}} T_{\text{b}} + I_{\text{i3}}(T_{\text{partCycle}} - \tau_5), & \tau_5 < T_{\text{partCycle}} < T_{\text{oneFullCycle}}. \end{cases}$$

(3.39)

Explanation of Equation (3.39):

Equation (3.39) describes the charge consumption over a partial cycle of duration $T_{\text{partCycle}}$, assuming that the operations occur sequentially in the nominal duty-cycle order. If $T_{\text{partCycle}} \le T_{\text{s}}$,

only a portion of the sensing operation is completed, and the corresponding charge consumption is $I_s T_{\text{partCycle}}$. If $T_{\text{partCycle}}$ exceeds T_s but remains within $T_s + T_{i1}$, the sensing operation is fully completed and the remaining time is spent in the idle period after sensing; hence, the charge includes the full sensing contribution plus the partial or complete contribution of this idle interval. Similarly, if $T_{\text{partCycle}}$ extends beyond $T_s + T_{i1}$ but does not exceed $T_s + T_{i1} + T_e$, then sensing and idle-after-sensing are fully completed, and the remaining time contributes to the E-ink display operation. The same principle applies to the subsequent operations. In general, the equation adds the full charge contributions of all operations completed before $T_{\text{partCycle}}$, together with the partial contribution of the operation active at the truncation instant.

The **overall total charge consumption** (in mAh) of the RIoT node then can be expressed as:

$$Q_{\text{total}} = Q_{\text{fastAdvInt}} + Q_{\text{slowAdvInt}} + Q_{\text{bleCmdRx}} + Q_{\text{start}} + Q_{\text{sens}} + Q_{\text{eink}} + Q_{\text{bleTx}} + Q_{\text{idle}} + Q_{\text{partial}}, \quad (3.40)$$

where

Q_{idle} denotes the total charge consumed during all idle states, including both the initial idle phases—such as the BLE connected-only mode following BLE advertising and a subsequent connection with gateway/access point, and the idle periods following BLE command reception and startup—as well as the interleaved idle periods within the full operational cycles, namely those occurring after sensing, E-ink display updates, and BLE transmissions. Thus, the overall charge consumption during idle periods in Eq. (3.28) can be re-written as:

$$\begin{aligned} Q_{\text{idle}} &= Q_{\text{connInt}} + Q_{\text{idleBleCmdRx}} + Q_{\text{idleStart}} + Q_{\text{idleSens}} + Q_{\text{idleEink}} + Q_{\text{idleBleTx}} \\ &= I_{\text{connInt}}[(T_{\text{connInt}} \times N_{\text{connInt}}) + T_{\text{idleBleCmdRx}} + T_{\text{idleStart}} + (T_{\text{idleSens}} \times N_{\text{fullCycles}}) + \\ &\quad \kappa_{\text{idle}}(T_{\text{idleEink}} \times N_{\text{fullCycles}}) + \kappa_{\text{idle}}(T_{\text{idleBleTx}} \times N_{\text{fullCycles}})]. \end{aligned} \quad (3.41)$$

where

$$\kappa_{\text{idle}} = \begin{cases} 1.007, & \text{for the normal operating mode,} \\ 1.14, & \text{for the low-power operating mode.} \end{cases}$$

Thus, we can rewrite Eq. (3.40) as follows:

$$\begin{aligned} Q_{\text{total}} = {} & (I_{\text{fastAdvInt}} \times T_{\text{fastAdvInt}} \times N_{\text{fastAdv}}) + (I_{\text{slowAdvInt}} \times T_{\text{slowAdvInt}} \times N_{\text{slowAdv}}) \\ & + (I_{\text{bleCmdRx}} \times T_{\text{bleCmdRx}}) + (I_{\text{start}} \times T_{\text{start}}) \\ & + N_{\text{fullCycles}}[(I_{\text{sens}} \times T_{\text{sens}}) + (I_{\text{eink}} \times T_{\text{eink}}) + (I_{\text{bleTx}} \times T_{\text{bleTx}})] + Q_{\text{idle}} + Q_{\text{partial}}. \end{aligned} \quad (3.42)$$

The total charge consumption in Coulombs is given by:

$$Q_{\text{total}} \times 3.6 \quad (3.43)$$

and the total energy consumption (in mWh) of the node over an operating duration of T is given by:

$$P_{\text{total}} = Q_{\text{total}} \times V_{\text{operating}} \quad (3.44)$$

where $V_{\text{operating}}$ is the operating voltage of the node.

Finally, the total energy consumption in Joules is given by:

$$P_{\text{total}} \times 3.6 \quad (3.45)$$

The **overall average current consumption** (in mA) of the node over an operating duration of T is given by:

$$I_{\text{overall}} = \frac{I_1 \times (T_{\text{initOper}} + T_{\text{fullCycles}}) + I_2 \times T_{\text{partCycle}}}{T} \quad (3.46)$$

where $T = T_{\text{initOper}} + T_{\text{fullCycles}} + T_{\text{partCycle}}$, and

$$I_1 = \frac{Q_{\text{fastAdvInt}} + Q_{\text{slowAdvInt}} + Q_{\text{bleCmdRx}} + Q_{\text{start}} + Q_{\text{sens}} + Q_{\text{eink}} + Q_{\text{bleTx}} + Q_{\text{idle}}}{T_{\text{initOper}} + T_{\text{fullCycles}}}, \qquad I_2 = \frac{Q_{\text{partial}}}{T_{\text{partCycle}}}$$

Table 8 presents the default parameters used to calculate the node's energy consumption in both normal (full hybrid communication configuration) and low-power (partial hybrid communication configuration) node operations. These parameters were derived from comprehensive measurements taken across various operational states of the node. The average values for current consumption for startup, sensing, E-ink display update, and BLE or NBVLC TX and the idle periods following these operations correspond to the case where the node is connected via BLE to a central device (e.g. gateway or access point) for the whole operating time. The idle periods, for example, after sensing, E-ink displaying, and BLE or NBVLC TX, can be modified in the firmware as per user's requirements. Additionally, parameters such as BLE transmit power (default value of 0 dBm), advertising intervals (both fast and slow), connection intervals, timeouts, and other related BLE settings can also be configured in the node's firmware.

Table 8. Default parameters used to compute the energy consumption of the RIoT node for a given scenario under normal operation (full hybrid communication configuration) and low-power operation (partial hybrid communication configuration).

Default parameter	**Normal (full hybrid communication configuration)**	**Low-power (partial hybrid communication configuration)**
Operating voltage, $V_{\text{operating}}$	3.3 V	
BLE TX power level, P_{tx}	0 dBm	
Node operating time, T	1 hour	
T_{fastAdv}	30 s	
T_{slowAdv}	30 s	
T_{bleConn}	30 s	
$T_{\text{slowAdvInt}}$	152.5 ms	
$T_{\text{fastAdvInt}}$	20 ms	
T_{advEvent}	4.18 ms	
$T_{\text{slowAdvIdle}}$	$T_{\text{slowAdvInt}} - T_{\text{advEvent}}$ = 148.32 ms	
$T_{\text{fastAdvIdle}}$	$T_{\text{fastAdvInt}} - T_{\text{advEvent}}$ = 15.82 ms	
I_{advIdle}	5.46 mA	1.32 mA
I_{advEvent}	9.65 mA	5.95 mA

T_{connInt}	45 ms	
$T_{\text{connEvent}}$	2.14 ms	
$I_{\text{connEvent}}$	7.31 mA	3.52 mA
I_{connIdle}	5.43 mA	1.33 mA
T_{connIdle}	$T_{\text{connInt}} - T_{\text{connEvent}}$ = 42.86 ms	
I_{bleCmdRx}	7.36 mA	4.20 mA
T_{bleCmdRx}	2.33 ms	2.33 ms
$T_{\text{idleBleCmdRx}}$	100 ms	
$I_{\text{idleBleCmdRx}}$	I_{connInt}=5.52 mA	I_{connInt}=1.434 mA
I_{start}	15.03 mA	14.30 mA
T_{start}	915.8 ms	911.1 ms
$T_{\text{idleStart}}$	1.9 s	
$I_{\text{idleStart}}$	I_{connInt}=5.52 mA	I_{connInt}=1.434 mA
T_{sens}	516 ms	
I_{sens}	12.26 mA	8.23 mA
T_{idleSens}	200 ms	
I_{idleSens}	I_{connInt}=5.52 mA	I_{connInt}=1.434 mA
T_{eink}	0.435 s (optimized E-ink)	
I_{eink}	7.24 mA	3.63 mA
T_{idleEink}	2.1 s	
I_{idleEink}	1.007×I_{connInt}=5.56 mA	1.14×I_{connInt}=1.635 mA
N_{c}	6	
T_{c}	68 ms	
T_{d}	100 ms	
I_{d}	1.007×I_{connInt}=5.56 mA	1.14×I_{connInt}=1.635 mA
T_{nbvlc}	0.908 s	
I_{ctx}	9.15 mA	8.90 mA
I_{nbvlc}	7.17 mA	4.90 mA

$T_{\text{idleNbvlc}}$	5.12 s	
$I_{\text{idleNbvlc}}$	$1.007 \times I_{\text{connInt}}$=5.56 mA	$1.14 \times I_{\text{connInt}}$=1.635 mA
I_{bleTx}	9.10 mA	5.91 mA
T_{bleTx}	3.13 ms	
$T_{\text{idleBleTx}}$	5 s	

Based on the default parameter values listed in Table 8 and the analytical expressions in (3.12)–(3.46), the overall energy consumption of the RIoT node for normal operation (full hybrid communication configuration) and low-power operation (partial hybrid communication configuration) is calculated and presented in Table 9 for the scenario defined at the beginning of this section. Compared to the normal node operation, we obtain a staggering ~65% decrease in energy consumption with the low-power node operation, even though both cases involve the node performing the same tasks.

Table 9. Energy computation for normal, low-power and very low-power node operations (default parameters).

Computed parameters	**Normal**	**Low-power**	**Very low-power**
Q_{total}	6.06 mAh (21.8 C)	2.14 mAh (7.71 C)	0.215 mAh (0.776 C)
P_{total}	20.0 mWh (72.0 J)	7.07 mWh (25.45 J)	0.711 mWh (2.56 J)
I_{overall}	6.06 mA	2.14 mA	0.215 mA

3.4.2 Very low-power node operation

In this model, we consider the very low-power node operation scenario previously described in Section 3.3.3, where we analysed the impact of cutting points U9 and U6 on the average current consumption during deep sleep. Recall, in this scenario, BLE communication remains disabled. The total charge consumption for the very low power node operation can be formulated as follows:

$$Q_{\text{total}} = Q_{\text{start}} + Q_{\text{idleStart}} + Q_{\text{sens}} + Q_{\text{idleSens}} + Q_{\text{eink}} + \partial_{\text{nbvlc}} \times (Q_{\text{idleEink}} + Q_{\text{nbvlc}} + Q_{\text{idleNbvlc}}) + Q_{\text{deepSleep}} + Q_{\text{partial}} \quad (3.47)$$

where $\partial_{\text{nbvlc}} = 1$ if NBVLC uplink TX functionality is required; otherwise $\partial_{\text{nbvlc}} = 0$.

This means that when the NBVLC functionality is enabled ($\partial_{\text{nbvlc}} = 1$), the node follows the complete sequence:

Startup → Idle after startup → Sensing → Idle after sensing → E-ink → Idle after E-ink → NBVLC uplink TX → Idle after NBVLC TX → Deep sleep (as illustrated in Figure 3.3.7(b)).

When NBVLC uplink TX is not enabled ($\partial_{\text{nbvlc}} = 0$), the node follows the sequence:

Startup → Idle after startup → Sensing → Idle after sensing → E-ink → Deep sleep (as illustrated in Figure 3.3.7(a)).

In the computations that follow, we consider the very low-power firmware node operation, with the NBVLC uplink TX functionality disabled ($\partial_{\text{nbvlc}} = 0$), as well as BLE. We also consider the case where the node achieved the lowest current consumption, i.e., when both U6 and U9 measuring

points were cut (see Section 3.3.3, Table 6). We also consider using the optimized E-ink display in very low-power firmware node operation.

Unlike the normal and low-power operating modes considered previously, the startup (also referred to as wake-up in this model) operation will be part of the operation cycle. It will be repeated over the node's operating duration, along with the sensing, optimized E-ink-display update, and deep-sleep operations (including any idle periods). The duration of a full cycle consisting of startup, sensing, optimized E-ink displaying, and deep sleep operations (including the idle periods) can be written as:

$$T_{\text{oneFullCycle}} = T_{\text{start}} + T_{\text{idleStart}} + T_{\text{sens}} + T_{\text{idleSens}} + T_{\text{eink}} + T_{\text{deepSleep}} \tag{3.48}$$

where T_{start}, $T_{\text{idleStart}}$, T_{sens}, T_{idleSens}, T_{eink}, $T_{\text{deepSleep}}$ represent the time durations for the startup phase, idle state after startup, sensing operation, idle state after sensing, E-ink display operation, and deep sleep state, respectively. The number of full cycles over the node's operating time is given by

$$N_{\text{fullCycles}} = \left\lfloor \frac{T}{T_{\text{oneFullCycle}}} \right\rfloor. \tag{3.49}$$

Thus, the total duration of the full cycles is given by:

$$T_{\text{fullCycles}} = N_{\text{fullCycles}} \times T_{\text{oneFullCycle}}. \tag{3.50}$$

The remaining partial cycle duration is therefore

$$T_{\text{partCycle}} = T - T_{\text{fullCycles}}, \qquad 0 \le T_{\text{partCycle}} < T_{\text{oneFullCycle}}. \tag{3.51}$$

For the case $\partial_{\text{nbvlc}} = 0$, let

$$T_{\text{st}} = T_{\text{start}}, T_{\text{i1}} = T_{\text{idleStart}}, T_{\text{s}} = T_{\text{sens}}, T_{\text{i2}} = T_{\text{idleSens}}, T_{\text{e}} = T_{\text{eink}}, T_{\text{d}} = T_{\text{deepSleep}},$$

with corresponding currents

$$I_{\text{st}} = I_{\text{start}}, I_{\text{i1}} = I_{\text{idleStart}}, I_{\text{s}} = I_{\text{sens}}, I_{\text{i2}} = I_{\text{idleSens}}, I_{\text{e}} = I_{\text{eink}}, I_{\text{d}} = I_{\text{deepSleep}}.$$

We define the cumulative time boundaries

$$\tau_1 = T_{\text{st}}, \quad \tau_2 = T_{\text{st}} + T_{\text{i1}}, \quad \tau_3 = T_{\text{st}} + T_{\text{i1}} + T_{\text{s}},$$
$$\tau_4 = T_{\text{st}} + T_{\text{i1}} + T_{\text{s}} + T_{\text{i2}}, \quad \tau_5 = T_{\text{st}} + T_{\text{i1}} + T_{\text{s}} + T_{\text{i2}} + T_{\text{e}}.$$

Then the charge consumed in the partial cycle can be written as

$$Q_{\text{partial}} = \begin{cases} I_{\text{st}}\, T_{\text{partCycle}}, & 0 \le T_{\text{partCycle}} \le \tau_1, \\ I_{\text{st}} T_{\text{st}} + I_{\text{i1}}\left(T_{\text{partCycle}} - \tau_1\right), & \tau_1 < T_{\text{partCycle}} \le \tau_2, \\ I_{\text{st}} T_{\text{st}} + I_{\text{i1}} T_{\text{i1}} + I_{\text{s}}\left(T_{\text{partCycle}} - \tau_2\right), & \tau_2 < T_{\text{partCycle}} \le \tau_3, \\ I_{\text{st}} T_{\text{st}} + I_{\text{i1}} T_{\text{i1}} + I_{\text{s}} T_{\text{s}} + I_{\text{i2}}\left(T_{\text{partCycle}} - \tau_3\right), & \tau_3 < T_{\text{partCycle}} \le \tau_4, \\ I_{\text{st}} T_{\text{st}} + I_{\text{i1}} T_{\text{i1}} + I_{\text{s}} T_{\text{s}} + I_{\text{i2}} T_{\text{i2}} + I_{\text{e}}\left(T_{\text{partCycle}} - \tau_4\right), & \tau_4 < T_{\text{partCycle}} \le \tau_5, \\ I_{\text{st}} T_{\text{st}} + I_{\text{i1}} T_{\text{i1}} + I_{\text{s}} T_{\text{s}} + I_{\text{i2}} T_{\text{i2}} + I_{\text{e}} T_{\text{e}} + I_{\text{d}}\left(T_{\text{partCycle}} - \tau_5\right), & \tau_5 < T_{\text{partCycle}} < T_{\text{oneFullCycle}}. \end{cases} \tag{3.52}$$

Considering $\partial_{\text{nbvlc}} = 0$, we can rewrite Eq. (3.37) as follows:

$$Q_{\text{total}} = N_{\text{fullCycles}}\left[\left(I_{\text{start}} \times T_{\text{start}}\right) + \left(I_{\text{idleStart}} \times T_{\text{idleStart}}\right) + \left(I_{\text{sens}} \times T_{\text{sens}}\right) + \left(I_{\text{idleSens}} \times T_{\text{idleSens}}\right) + \left(I_{\text{eink}} \times T_{\text{eink}}\right) + \left(I_{\text{deepSleep}} \times T_{\text{deepSleep}}\right)\right] + Q_{\text{partial}}\ , \tag{3.53}$$

where I_{start}, $I_{\text{idleStart}}$, I_{sens}, I_{idleSens}, I_{eink}, $I_{\text{deepSleep}}$ represent the average current consumption for the startup phase, idle state after startup, sensing operation, idle state after sensing, E-ink display operation, and deep sleep state, respectively.

The **overall average current consumption** (in mA) of the node in **very low power operation mode** over an operating duration of T is given by:

$$I_{\text{overall}} = \frac{\left(I_1 \times T_{\text{fullCycles}}\right) + \left(I_2 \times T_{\text{partCycle}}\right)}{T} \tag{3.54}$$

where $T = T_{\text{fullCycles}} + T_{\text{partCycle}}$, and

$$I_1 = \frac{Q_{\text{start}} + Q_{\text{idleStart}} + Q_{\text{sens}} + Q_{\text{idleSens}} + Q_{\text{eink}} + Q_{\text{deepSleep}}}{T_{\text{fullCycles}}}, \qquad I_2 = \frac{Q_{\text{partial}}}{T_{\text{partCycle}}}$$

Using the average current consumption values in Table 6 (considering both U6 and U9 cut) and considering an operating time of T =1 hour, the overall energy consumption of the RIoT node in the very low power operation mode is given in Table 9. It can be concluded that disabling the communication modules while allowing the node to remain active for only a brief period before entering a prolonged deep sleep significantly reduces the overall energy consumption of the node.

3.5 RIoT Node Energy Consumption Prediction

Building upon the models described in Section 3.4, we have developed an energy prediction app that allows users to modify various parameters and activate different node operations to predict the energy consumption based on their inputs. The app features three tabs:

(i) Tab 1: Predicts energy consumption for normal operating mode (full hybrid communication configuration).
(ii) Tab 2: Predicts energy consumption for low-power operating mode (partial hybrid communication configuration).
(iii) Tab 3: Predicts energy consumption for very low-power operating mode considering hardware optimizations (for communication configurations with either both BLE and NBVLC disabled, or BLE disabled and NBVLC uplink only enabled).

Interested readers may download the developed energy prediction tool from [2]. Further details on the energy measurement, analysis, prediction, and optimization of the SUPERIOT node can be found in [3] and [4].

3.5.1 Tab 1: Normal node operation

A snapshot of **Tab 1 (normal node operation**) is shown in Figure 3.5.1. In this Tab, the users can specify the following parameters:

(i) Amount of time that the node should spend in the two BLE advertising modes (fast and slow),
(ii) Amount of time that the node should stay in BLE-connected mode only (before the other functionalities are activated),
(iii) Operating voltage of the node,
(iv) Operating duration of the node,
(v) BLE TX power level,
(vi) BLE advertising intervals for fast and slow modes,
(vii) BLE connection interval
(viii) Idle periods duration, for example, after the sensing, E-ink, and NBVLC operations.
(ix) Option to activate/deactivate the node's functionalities such as sensing, E-ink display, and NBVLC operations,
(x) Option to enable/disable optimized E-ink display.

In this operation mode, the node remains connected to a central device via BLE for the whole operating time. Depending on the user's input parameters, the other parameters (non-editable) such as average current consumed during BLE advertising, BLE connection, startup, sensing, E-ink, NBVLC, etc. (including the idle periods) will change accordingly.

Once the user has configured the input parameters, pressing on the "EXECUTE" button will display the energy/charge consumption of the individual operations/states as well as other related information such as number of cycles, number of BLE advertising and connection events, among others, as shown in Figure 3.5.1. The overall average current consumption of the node (in mA), total charge consumption (in mAh and Coulombs) and total energy consumption (in mWh and Joules) will also be displayed. Furthermore, the users will be able to visualize the different node's states/operations in a plot, along with their instantaneous current consumption values and durations, as shown in Figure 3.5.1.

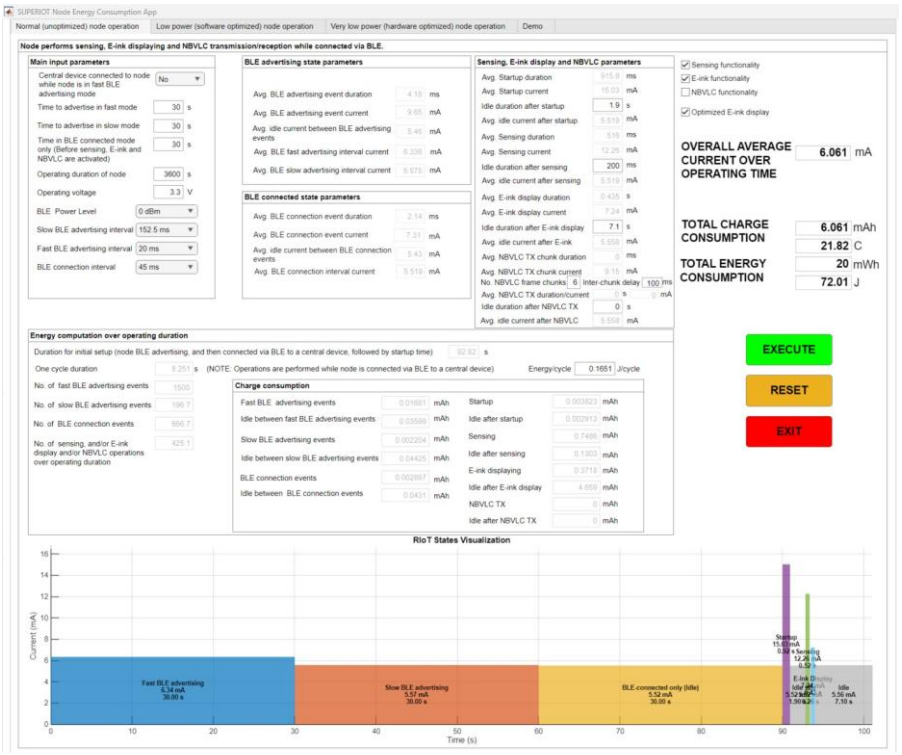

Figure 3.5.1. Energy consumption prediction App (Tab 1: Normal node operation).

3.5.2 Tab 2: Low power node operation

Tab 2 is similar to Tab 1, with the same input parameters and output information. However, in this case, the user can get an insight into the overall energy consumption when the node has been optimized for low-power operation with reduced NBVLC functionality (i.e. BLE uplink/downlink and NBVLC uplink only).

3.5.3 Tab 3: Very low power node operation

A snapshot of **Tab 3**, corresponding to the **very low power operating mode**, is shown in Figure 3.5.2. Unlike Tabs 1 and 2, Tab 3 considers operating configurations in which BLE and NBVLC communication are either both disabled, or BLE is disabled while NBVLC uplink transmission alone may be enabled. In this mode, the node can be configured to wake up independently (startup), perform sensing and E-ink display update operations, including the associated idle periods, and then enter deep sleep in each cycle. An option is also provided to enable NBVLC uplink transmission. Accordingly, the repeated per-cycle operation sequence in this mode consists of startup, sensing, E-ink display update, optional NBVLC uplink transmission, any intermediate idle periods, and deep sleep, while BLE remains disabled throughout.

In Tab 3, the users can specify the following parameters:

(i) Operating voltage of the node,
(ii) Operating duration of the node,
(iii) Idle period after the startup, sensing and deep sleep operations,
(iv) Option to also activate the NBVLC functionality. If activated, the user will be able to specify other parameters such as the idle durations after E-ink displaying and NBVLC TX, before the node goes into deep sleep (deep sleep duration can also be specified),
(v) Hardware optimization configurations, and
(vi) Option to enable/disable optimized E-ink display.

Like Tabs 1 and 2, once the user has configured the input parameters, pressing on the "EXECUTE" button will display the energy/charge consumption of the individual operations/states, as shown in Figure 3.5.2. The overall average current consumption of the node (in mA), total charge consumption (in mAh and Coulombs), and total energy consumption (in mWh and Joules) will also be displayed. Furthermore, the users will be able to visualize the different node's states/operations in a plot, along with their instantaneous current consumption values and durations, as shown in Figure 3.5.2.

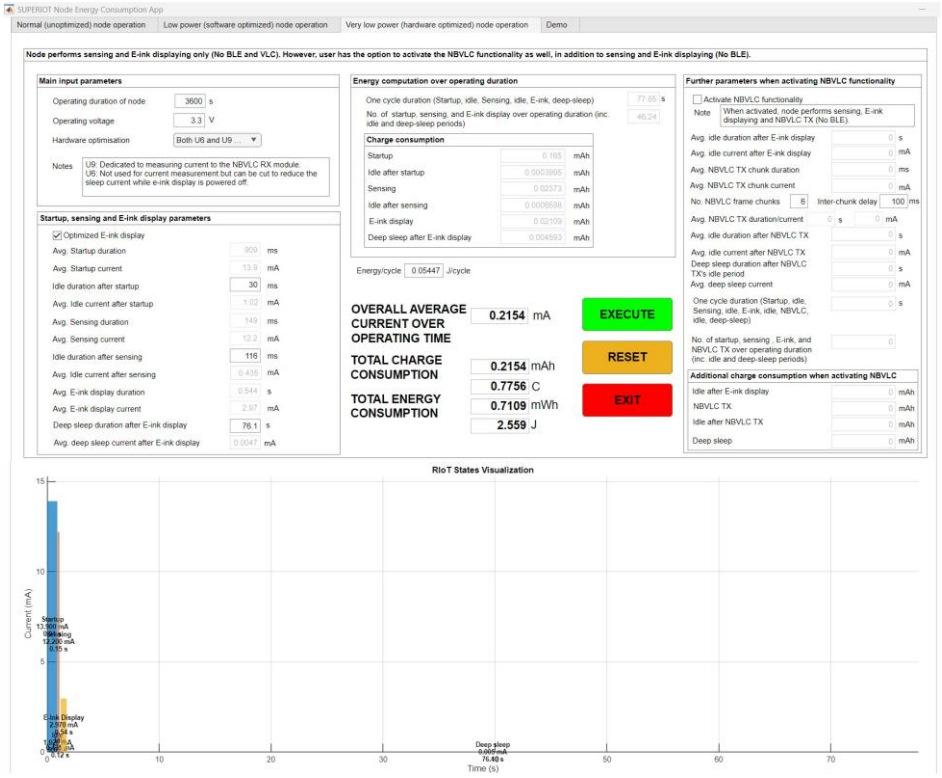

Figure 3.5.2. Energy consumption prediction App (Tab 3: Very low power node operation).

3.6 Validation of Energy Models

The developed energy models for the Si-based node in Section 3.4 are integrated into the energy consumption prediction app (described in Sections 3.5.1, 3.5.2 and 3.5.3), and the models cover the different node operations: (i) normal, (ii) low-power, and (iii) very low-power. In this section, the models integrated into the energy prediction app are thoroughly validated using new measurement data obtained from the node under various configurations and scenarios, as shown in Table 10. Remarkably, the models achieved an accuracy exceeding 97%, indicating their reliability in predicting the node's energy consumption in diverse node configurations.

Table 10. Validation of energy models (√ means feature/functionality activated and X means feature/functionality disabled).

	Normal mode				**Low power mode**			**Very low power mode**		
BLE	√	√	√	√	√	√	√	X	X	X
NBVLC	√	√	X	√	X	√	X	√	X	X
Sensing	√	√	√	√	√	√	√	√	√	√
E-ink display (unoptimized)	√	√	√	X	X	X	X	X	X	√
E-ink display (optimized)	X	X	X	X	√	√	X	√	√	X
P_{tx} (dBm)	0	8	8	0	0	0	8	-	-	-
T (s)	562	755	409.7	804	937	1096	629	1410	509	381.7
T_{fastAdv} (s)	18.92	25.59	27.91	18.09	28.1	28.76	28.33	-	-	-
$T_{\mathrm{fastAdvInt}}$ (ms)	20	20	20	20	20	20	20	-	-	-
T_{slowAdv} (s)	40.76	33.22	71.9	45.18	46.41	42.1	48.06	-	-	-
$T_{\mathrm{slowAdvInt}}$ (ms)	152.5	152.5	152.5	152.5	152.5	152.5	152.5	-	-	-
T_{bleConn} (s)	29.78	26.52	49.35	61.1	47.33	52.01	94.4	-	-	-
T_{connInt} (ms)	45	11.25	11.25	45	45	45	250	-	-	-
$T_{\mathrm{idleBleCmdRx}}$(ms)	-	-	-	-	85	11.15	27.01	-	-	-
$T_{\mathrm{idleStart}}$ (s)	7.02	7.4	9.542	7.02	6.97	11.96	6.98	0.03	0.03	0.03
T_{idleSens} (ms)	200	200	200	200	200	182.2	252.8	122.4	116	116
T_{idleEink} (s)	2.1	2.07	7.642	-	2.08	2.05	-	1.055	0	0
N_{c}	1	1	1	1	-	6	-	6	-	-
T_{d} (ms)	-	-	-	-	-	100	-	100	-	-
$T_{\mathrm{idleNbvlc}}$ (s)	5.12	5.5	-	5.12	-	10.31	-	1.00	-	-
$T_{\mathrm{idleBleTx}}$ (s)	-	-	-	-	5.19	-	5.16	-	-	-
$T_{\mathrm{deepSleep}}$ (s)	-	-	-	-	-	-	-	72.7	76.1	73.9
U6 cut / U9 cut	-	-	-	-	-	-	-	X / X	√ / √	√ / √
Model prediction (J)	**11.42**	**16.64**	**8.81**	**16.2**	**6.44**	**7.54**	**4.00**	**3.373**	**0.381**	**0.357**
Measured (J)	**11.32**	**16.60**	**8.65**	**16.38**	**6.34**	**7.46**	**3.93**	**3.37**	**0.39**	**0.36**
Accuracy (%)	**99.1**	**99.8**	**98.2**	**98.9**	**98.4**	**98.9**	**98.2**	**99.9**	**97.7**	**99.2**

3.7 Chapter Summary

The energy characterization of the SUPERIOT Si-based RIoT node has established a solid foundation for energy optimization and sustainability in the ongoing development of hybrid and fully printed IoT nodes. A comprehensive understanding of the node's energy consumption was achieved through extensive measurements across various operating states. The insights gained from these measurements informed the development of models that accurately predict energy consumption under three modes, achieving a validation accuracy of over 97%. This high accuracy enables precise energy budgeting, optimization, and lifecycle assessments for future node iterations. As the project advances to incorporate energy harvesting in the hybrid node and printed electronics in the final implementation, these models will play a critical role in guiding energy management strategies. They will enable the design of nodes that operate efficiently under varying energy availability conditions, ensuring continuous functionality even in resource-constrained scenarios. The ability to benchmark the current Si-node's energy performance against future configurations will facilitate a structured approach to achieving energy sustainability, ensuring that each design iteration builds upon the efficiency gains of its predecessor.

4 Organic Components

Printed energy harvesting and storage devices are summarized in this section, where printed electronics (PE) components are presented. The chapter summarizes the main developments undertaken in SUPERIOT based on D2.3 for each printed device in a separate sub-section. The fabrication process and the main electrical characterization results are discussed where the status of the integration process onto demonstrators later in the project in WP4 are presented in Sections 5, 6, and 7.

4.1 Printed Diodes

The fabrication of solution-processed Zinc Tin Oxide (ZTO) diodes was described in D2.3. Individual patterned diodes were successfully fabricated based on Titanium/Platinum-Doped Zinc Tin Oxide/Silver (Ti/Pt-ZTO/Ag) stacks and with patterned active areas from 25 μm^2 to 400 μm^2. Good performance devices were fabricated with very low reversed currents in the range of pA and forward currents of 10^{-4} A to 10^{-6} A for an applied bias of 3 V.

New designs were implemented to characterise the frequency response of the devices, as shown in Figure 4.1.1. This characterisation involved using the devices in a text-fixture in INES-TEC to characterise the S-parameter. However, the results obtained were still not successful and further tests are being performed, as well as thicker copper electrodes to facilitate the measurements. Nonetheless, results at low frequency are reproducible using this layout.

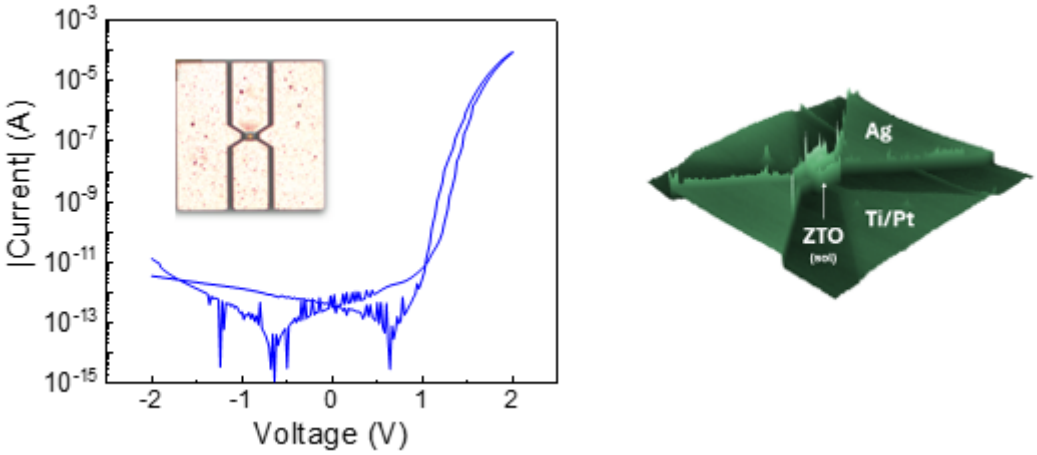

Figure 4.1.1. High-Frequency design diodes fabricated using the same Ti/Pt-ZTO-Ag stack: a) IV characteristics (low frequency) b) Atomic Force Microscopy map of a device.

Another important aspect related to the diode's fabrication, apart from their response in high frequency, is related to the integration. Although these devices achieved good rectification ratios and high reproducibility, they were fabricated as individual devices with micrometer-size electrodes that can only be characterized using specific probe stations and semiconductor parameter analyzer systems (only available in NOVA.id.FCT and VTT). To allow the integration in the Energy RIoT node and on the demonstrator, new masks were drawn, keeping the same active areas but extending the electrode pads to the border of the substrate while also increasing their sizes. Two designs are being implemented as shown in Figure 4.1.2: i) Electrodes widths of 1 mm and a pitch of 3 mm (Figure 4.1.2.a) allowing for a total of 12 diodes, 3 in each side of the substrate, and ii) electrode widths of 0,6 mm and pitch of 1 mm for a total of 32 devices, 8 in each substrate side (Figure 4.1.2.b). Figure 4.1.2.c shows a photograph of devices being fabricated on glass substrates.

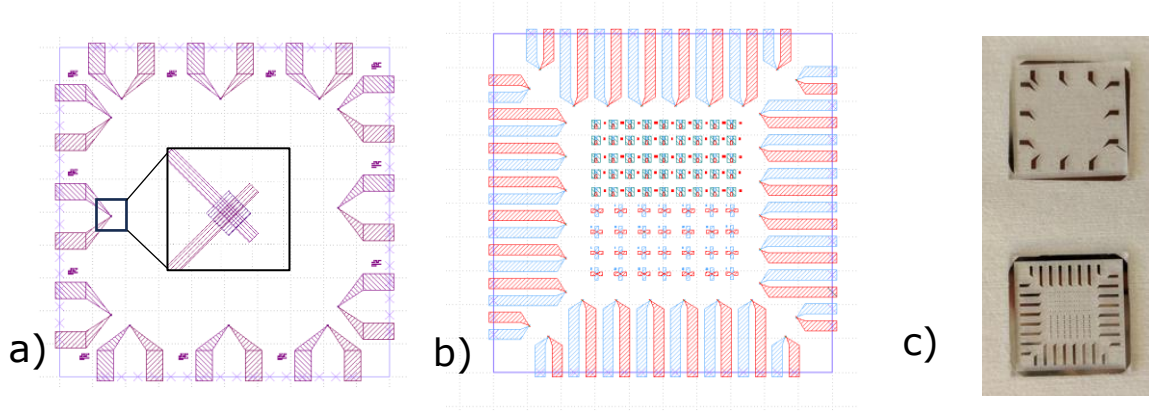

Figure 4.1.2. New layout of diodes for a 2.5 cm x 2.5 cm glass substrate for integration: a) Electrode width of 1 mm, pitch of 3 mm b) electrode width of 0.6 mm pitch of 1 mm c) Pt bottom contact of diodes using the new designs.

The integration of these devices was studied according to the requirements of each partner, and connector PCB boards where the devices will be bonded, were fabricated. Different strategies for bonding the thin film electrodes to the PCB boards such as wire-bonding, or the use of conductive inks/ tapes will be followed. This integration will facilitate the powering and signal extraction of the devices by all partners of SUPERIOT.

4.2 Printed Micro Supercapacitors

In D2.3 the team of NOVA.id.FCT has shown the early designs for the MXenes-based μSC to be incorporated on Demonstrator 2 and 3. To achieve desired demonstrator requirements (V = 3.5 V and C =15 mF) the following energy storage unit was designed:

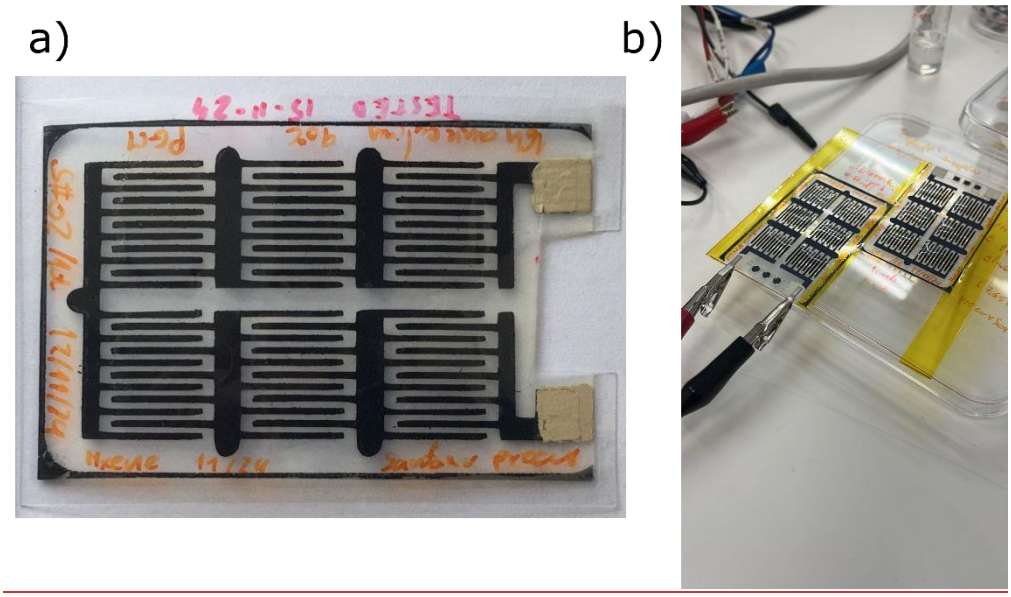

Figure 4.2.1. a) 6 Mxenes - μSC in series deposited on PEN and b) example of the complete device upon measurement.

The total area of the unit shown in Figure 4.2.1.a is about 100 cm^2 (12.5cm × 8 cm) and these devices can operate at voltage of 3.6 V in a polyvinyl alcohol/sulfuric acid (PVA/H_2SO_4) electrolyte (Figure 4.2.1.b). A more sustainable electrolyte option polyvinyl alcohol/lithium chloride (PVA/LiCl) was considered for the μSC development. However, this system does not fully solidify and exhibits a hygroscopic nature, aspects that are detrimental for the devices proper running. Similar comments can be made for hydrogels which can be unstable at wide operating voltage windows.

In Figure 4.2.2.a and Figure 4.2.2.b are shown the curves for cyclic voltammetry and galvanostatic charge discharge experiments, respectively, for the prepared energy storage unit. The resulting graphics exhibit the expected behavior for supercapacitors. The required voltage can be attained, although some electrical resistance is observed, most likely arising from the contacts. Nevertheless, capacitances in the range from 3.5 mF - 4.5 mF were obtained at 5 $mV.s^{-1}$. Some variability in the results is still observed, however it will be eliminated as much as possible with ink deposition optimization. Currently, MXene inks of 10 $mg.mL^{-1}$ are being deposited by blade coating and some edge effects can be observed, resulting in a non-uniform thickness across the sample. To further increase the capacitance, the utilization of the available working area is being maximized by reducing the interfingers distance to 300 mm.

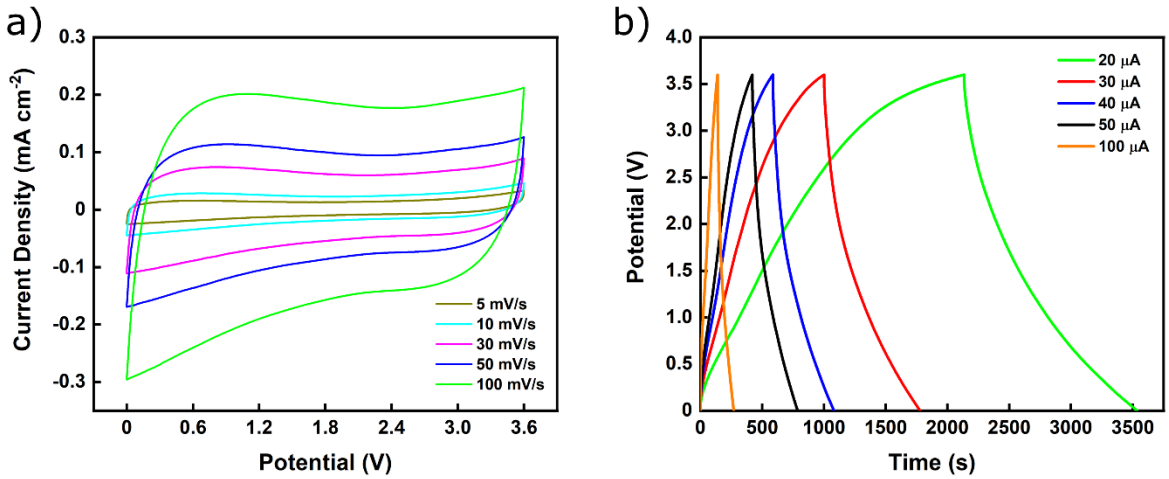

Figure 4.2.2. Representative graphs of a) cyclic voltammetry and b) galvanostatic charge/discharge measurements carried on the 6 µSC in series.

Taking into consideration the most up-to-date results, it will be required 4-5 stacked units to achieve the required 15 mF. This is an attainable metric, however the electrical connections between the different units may further increase the resistance and lead to capacitance loss. In parallel, the team at NOVA.id.FCT is also studying the possibility to design an in-plane unit (larger area) that could help improve the overall charge and discharge process.

In Figure 4.2.3.a is shown a planar energy storage unit composed of twelve µSC (4 in series, 3 in parallel). As before, the voltammograms (Figure 4.2.3.b) and charge discharge curves (Figure 4.2.3.c) exhibit a good capacitive performance. For this first attempt, the number of dispositive in series was reduced to four (2.4 V) as a proof-of concept. The high discharge currents are indicative of capacitances on de dozens of mF, however these results still need to be validated and demonstrate reproducibility at a working voltage of 3.5 V. Moreover, as the unit gets larger, despite the high electrical conductivity of MXenes, current collectors may be needed to prevent capacitance loss. This in plane approach would massively simply the integration process and as it keeps just two electrical contacts also removes the issues associated with the stacked devices tabs.

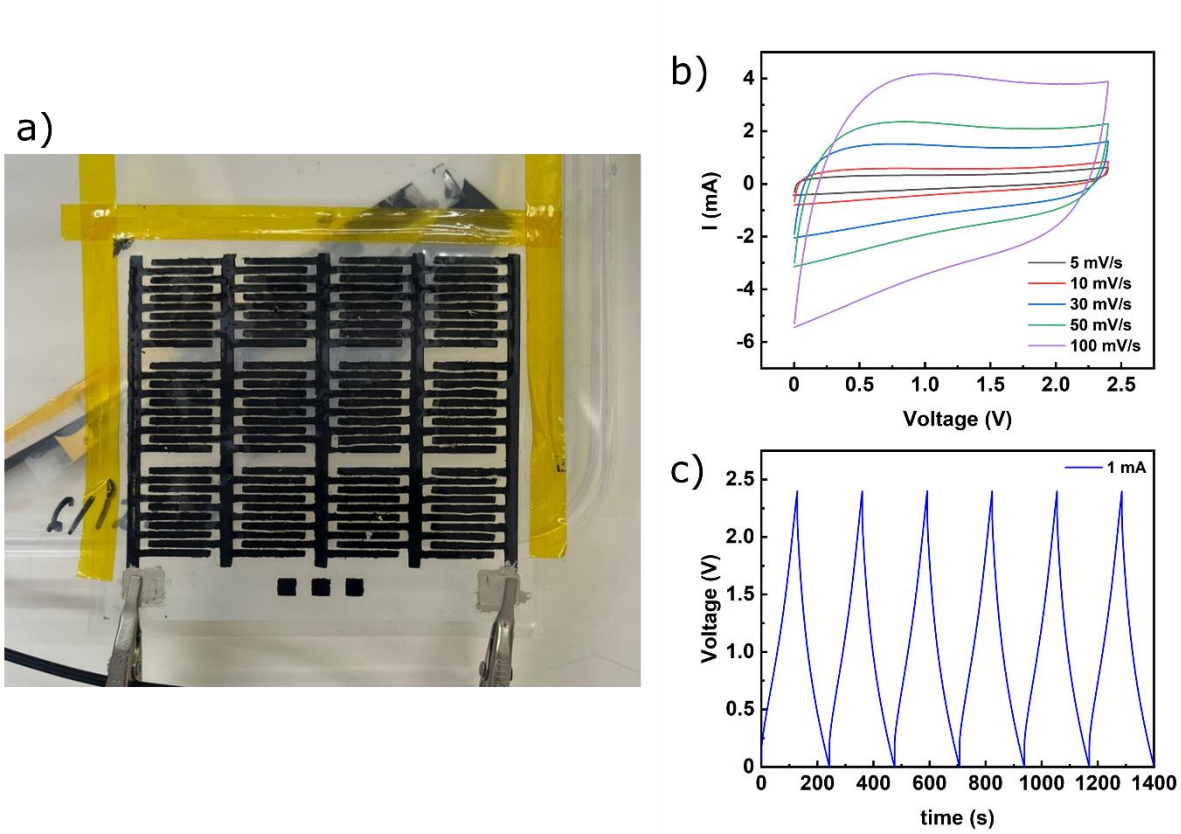

Figure 4.2.3. a) Energy storage unit composed by four μSC in series and three in parallel and respective b) cyclic voltammograms and c) galvanostatic charge-discharge curves at 1 mA.

4.3 Printed Organic Photovoltaic (OPV)

Based on the development in D2.3, the OPV is further improved to fit partners requirements for the integration and for the demonstrators in WP4.

Two devices have been developed based on polyethylene terephthalate/ Poly (3,4 ethylenedioxythiophene) (PET/PEDOT):

- PSS (PH1000) /P3HT:PCBM/LiF/Al (Poly(styrenesulfonic acid)/ Poly(3-hexylthiophene)/Phenyl-C61-butyric acid methyl ester/Lithium Fluoride/Aluminum)

- PSS (PH1000) /NF3000/LiF/Al (Poly(styrenesulfonic acid)/Organic conductive polymer/Lithium Fluoride/Aluminum)

The devices layout is presented in Figure 4.3.1. These devices layout will be used in Section 5 and 6 for integration and performance measurements.

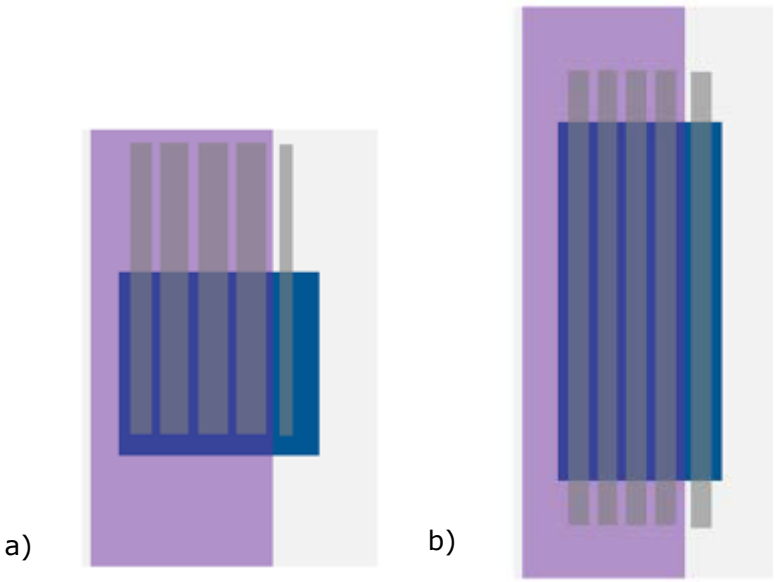

Figure 4.3.1. Two OPV layout with a) 3 single cells with 0.9 cm^2 active cell area/sample and b) 4 single cells with 1.65 cm^2 active cell area/sample.

5 SWIPT Subsystem with Integrated Printed Electronics

The Internet of Things (IoT) expansion demands nodes capable of long-term, maintenance-free operation, especially in remote or inaccessible environments. This work introduces a novel dual-band IoT node that integrates simultaneous wireless information and power transfer (SWIPT) and backscatter communication through a single, shared antenna and circuit. By employing a dual-band matching network, the node efficiently rectifies RF signals for energy harvesting and downlink information reception, while also supporting low-power backscatter uplink at 0.92 GHz. Over-the-air experimental results demonstrate simultaneous energy harvesting with a 100-kbps uplink and a 1 kbps downlink transmission, offering a practical solution for sustainable, long-lived sensor deployments. In addition, we integrated a humidity and temperature sensor powered by the printed solar cells and micro supercapacitor. Over-the-air measurements were conducted using the backscattering technique.

5.1 Introduction

The rapid expansion of the IoT demands long-lived, maintenance-free sensor nodes that can operate without frequent battery replacements. Two emerging approaches that address this need are SWIPT and backscatter communication. SWIPT delivers data and energy through a single downlink channel, reducing the reliance on batteries. In contrast, backscatter enables ultra-low-power uplink by reflecting existing RF signals rather than generating new ones, thereby minimizing energy consumption [5] [6] [7].

However, combining SWIPT and backscatter functionalities into a single, compact, battery less IoT node poses significant design challenges. Many existing solutions treat energy harvesting and communication paths separately, complicating the circuitry. Prior work has demonstrated dual-polarized rectifiers and backscattering [8], as well as multi-band rectifiers and harmonic backscatter approaches that extend functionality over different frequencies [9] [10] [11]. Yet, most implementations still rely on multiple antennas or treat energy and data flows independently, making integration difficult and limiting widespread deployment [12].

This work presents a unified dual-band IoT node, shown in Figure 5.1.1, that integrates SWIPT and backscatter communication into a single antenna and electronic board. The proposed design operates at 0.92 GHz for backscatter uplink plus WPT and 2.42 GHz for SWIPT downlink, employing a dual-band rectifier and matching network. The node efficiently harvests energy by merging these functionalities while simultaneously receiving and transmitting data.

Section 5.2 outlines the circuit design, including the antenna, matching network, and rectifiers. Section 5.3, 5.4, and 5.5 reports measurements that validate the node's performance, including S-parameter characterization, power conversion efficiency results, and over-the-air tests. Finally, Section 5.7 summarizes the integrated approach and its potential to enable truly battery less, sustainable IoT deployments.

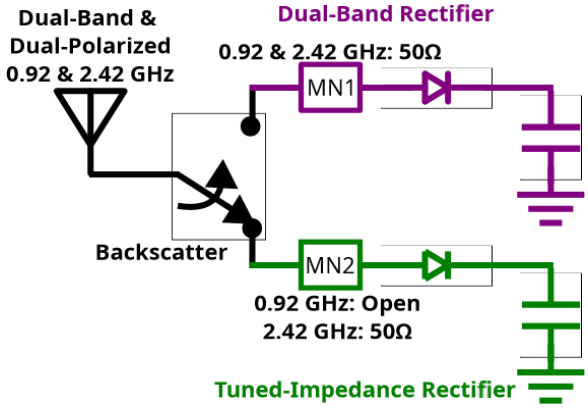

Figure 5.1.1. Block diagram of the proposed dual-band battery less IoT node, featuring a dual-band antenna, backscatter module, and rectifiers for energy harvesting and bidirectional communication at 0.92 GHz and 2.42 GHz.

5.2 Dual-Band Circuit Design

The proposed node incorporates essential components to facilitate simultaneous SWIPT and backscatter communication. A dual-band antenna and circuit that operates at 920 MHz for backscatter communication and WPT and 2.42 GHz for SWIPT.

To achieve a high-gain dual-band antenna operating at 920 MHz and 2.42 GHz, we designed a five-layer stacked configuration, which increases effective aperture and promotes constructive interference, thereby enhancing gain and directivity. The patch dimensions and feed locations were optimized using CST simulations. The antenna comprises a ground plane and five alternating layers: 1.57 mm Rogers RT/duroid 5880 substrates with patch antennas (layers 1, 3, and 5) and 12 mm and 30 mm air gaps (layers 2 and 4). Figure 5.2.1 shows the realized gain-radiation patterns. At 920 MHz, the peak gain is 5.97 dBi; at 2.42 GHz, it reaches 9.15 dBi. The polarization of the designed antenna at 2.42 GHz is orthogonal to the polarization at 920 MHz. Dual polarization reduces self-interference issues in the base station.

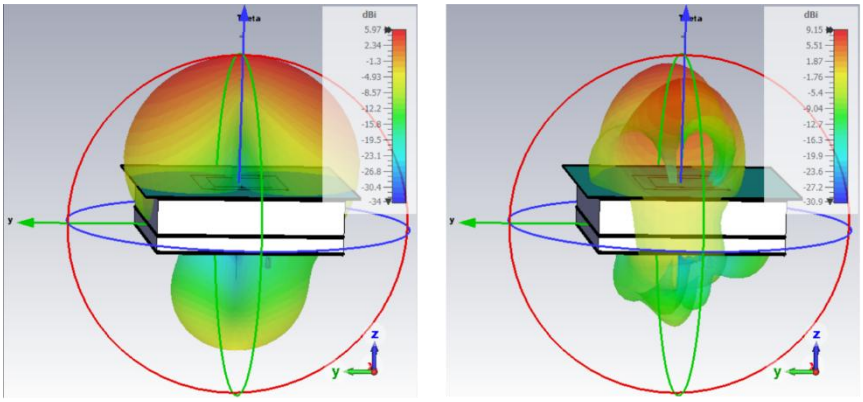

Figure 5.2.1. Realized gain radiation patterns of the dual-band antenna: 920 MHz with a peak gain of 5.97 dBi and 2.42 GHz with a peak gain of 9.15 dBi.

The electronic board, shown in Figure 5.2.2, employs an SPDT switch (AS213-92) to enable on-off keying (OOK) backscatter at 920 MHz by alternating the antenna load between two rectifier circuits: a Dual-Band Rectifier and a Tuned-Impedance Rectifier. Complementary signals V1 and V2 control the switch.

The Dual-Band Rectifier supports operation at 920 MHz and 2.42 GHz and is matched to 50 Ω for optimal power transfer. A low-barrier Schottky diode (SMS7630) with minimal parasitic capacitance ensures high power conversion efficiency. Coupled-line sections are used for the impedance-matching network and to establish open terminations at the diode's input and output. An RC low-pass filter recovers the DC component and data for SWIPT at the diode output.

In contrast, the Tuned-Impedance Rectifier presents an open circuit at 920 MHz to enable backscatter communication without absorbing signal power. At 2.42 GHz, it functions as a rectifier for SWIPT. A similar impedance-based approach ensures proper terminations at the diode output.

The complete board was designed and optimized using electromagnetic simulations in ADS and subsequently fabricated on a 1.57 mm Rogers RT/duroid 5880 substrate.

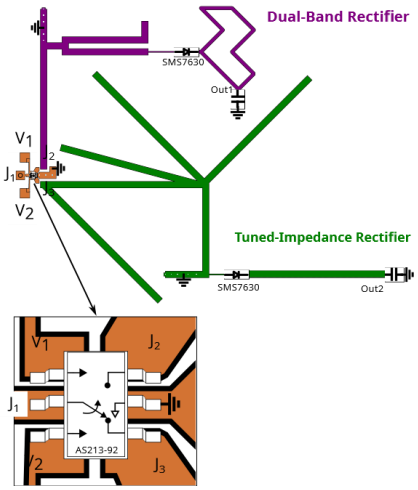

Figure 5.2.2. Schematic of the designed RF circuit, including the dual-band rectifier and the tuned-impedance rectifier configurations.

5.3 Experimental Validation

5.3.1 S-parameter Measurement

The setup is shown in Figure 5.3.1 is used to measure the S_{11} parameter of the designed electronic board. The board is tested with the switch control voltage V1 set to 0 V and 1.8 V. The rectifier outputs remain unloaded. Port 1 of the PNA-X vector network analyzer (N5247B) is connected to the board using coaxial cables.

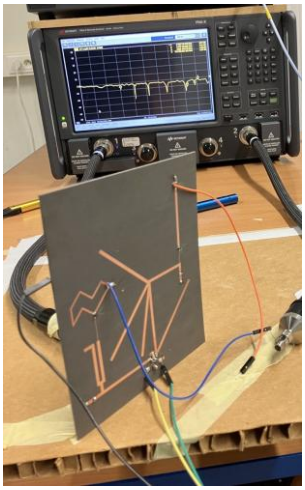

Figure 5.3.1. Setup for measuring the S_{11} of the electronic board.

Figure 5.3.2 presents the measured S11 parameter of the RF system as a function of frequency, highlighting the backscattering and SWIPT operational regions. Two configurations, V1 = 0 V and V1 = 1.8 V are shown. S_{11} reaches −11.25 dB and −2.62 dB in the backscattering and WPT region, indicating efficient power reflection. The SWIPT region exhibits a dip of approximately −10 dB, which is suitable for effectively absorbing the incident signal.

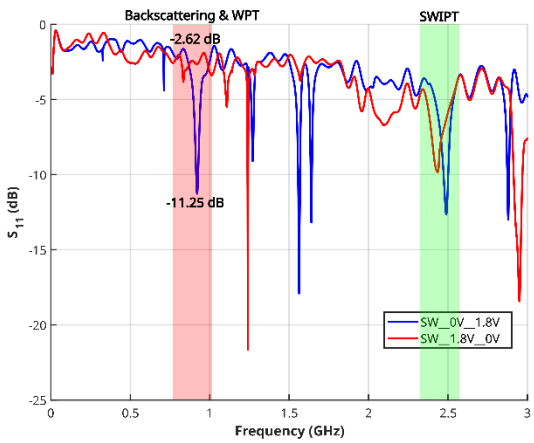

Figure 5.3.2. Measured input reflection coefficient S_{11} of the designed dual-band circuitry for different values of the switch control voltage V_1 = 0 and V_1 = 1.8 V.

5.4 Power Conversion Efficiency of Rectifiers

Using an RF signal generator and an oscilloscope, we measured the dual-band and tuned-impedance rectifiers' power conversion efficiency (PCE) from 0.5 GHz to 3 GHz. Figure 5.4.1 and Figure 5.4.2 present the measured PCE under two different switch control voltages, V1 =0 V and V1 =2 V.

At V1 = 0 V (Figure 5.4.1), the input (J1) is routed to the tuned impedance rectifier, which achieves a high PCE at 2.42 GHz (SWIPT band) but a negligible PCE at 920 MHz. The dual-band rectifier is effectively disconnected in this mode, resulting in nearly zero PCE.

At V1 =2 V (Figure 5.4.2), the input is routed to the dual-band rectifier. As designed, it delivers high PCE at both target frequencies, achieving approximately 53% at 920 MHz and 40% at 2.5 GHz. Meanwhile, the tuned impedance rectifier exhibits negligible PCE at all frequencies. Here, it is essential that the frequency of optimal PCE values in the SWIPT band aligns for both the dual-band and tuned-impedance rectifiers. Similarly, the dual-band rectifier's optimal PCE frequency should coincide with the tuned-impedance rectifier's open-impedance frequency in the backscattering and WPT band. Achieving these conditions ensures optimal backscattering and energy-harvesting performance.

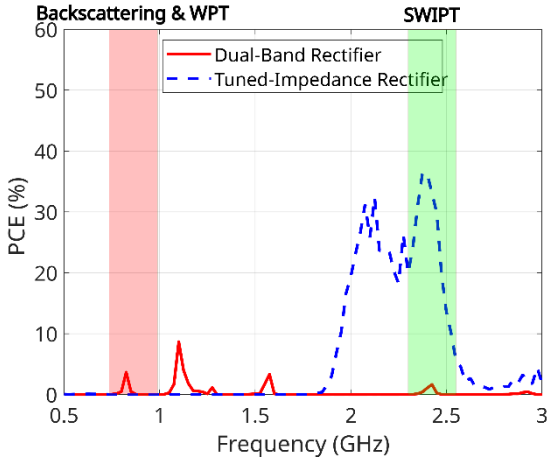

Figure 5.4.1. Power conversion efficiency of the designed rectifiers when the switch control voltage V1 is set to 0 V.

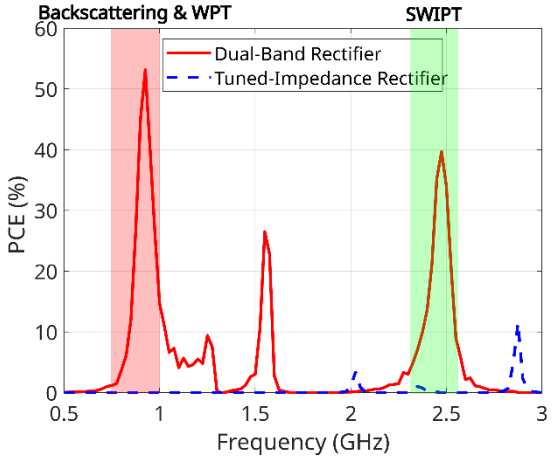

Figure 5.4.2. Power conversion efficiency of the designed rectifiers when the switch control voltage V1 is set to 2 V.

5.5 Over-the-Air Measurements

Figure 5.5.1 illustrates the over-the-air (OTA) measurement setup used to evaluate the performance of the proposed dual-band antenna and its integrated circuitry. The setup employs two RF signal generators (RFSG1 and RFSG2) to produce the desired signals: a 2.42 GHz SWIPT signal from RFSG1 and a continuous wave (CW) 920 MHz signal for backscattering from RFSG2. The power of both RF signal generators is set to 19 dBm. The generated RF signals are subsequently fed into the transmitting antennas (Tx1 and Tx2).

A receiving horn antenna (Rx Antenna) is placed to capture the backscattered signals, which are then monitored using a high-frequency oscilloscope (MSO9254A). The proposed dual-band antenna is positioned 1 m from the Tx and Rx Antennas and is connected to the dual-band circuit via a coaxial cable. An arbitrary function generator (AFG) provides the control signal V_1 to the circuit. The rectifier outputs are observed on Channels 3 and 4 of the oscilloscope. A power supply (PS) also powers an inverter IC to generate an inverted control signal V_2 from V_1.

The high-level voltage of V_1 is 2 V, and its data rate is fixed at 100 kbps with random bit patterns. The SWIPT signal is a two-tone signal with a 1 kHz frequency spacing.

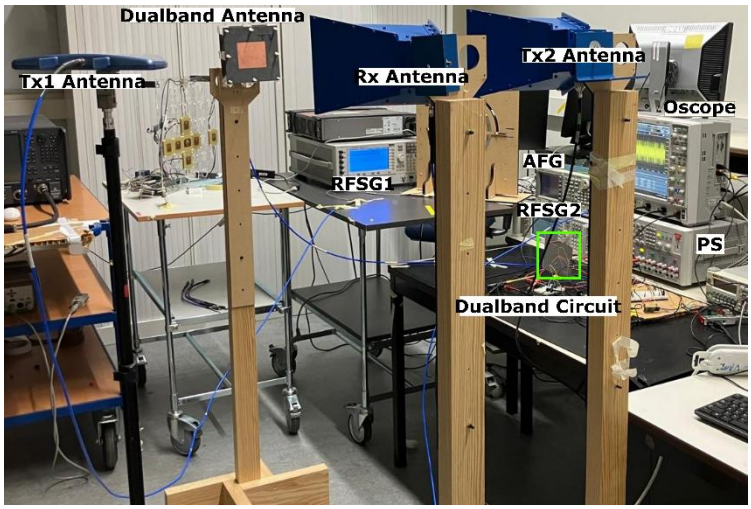

Figure 5.5.1. An over-the-air measurement setup was used to evaluate the dual-band antenna and circuit.

Figure 5.5.2 shows the received OOK backscattered signal VRX captured by the Rx horn antenna. During the "ON" modulation state, the peak-to-peak voltage reaches 0.95 V, while in

the "OFF" modulation state, it is 0.58 V, resulting in a modulation index of M ≈ 24.2%. The received signal is also affected by self-interference from the Tx antennas, introducing a continuous RF wave component. This self-interference reduces the effective modulation index. The 1 kHz SWIPT signal at VOUT2 is visible. The average DC voltages at VOUT1 and VOUT2 are 0.586 V and 0.126 V, respectively. Figure 5.5.3 shows the zoomed version of the waveforms.

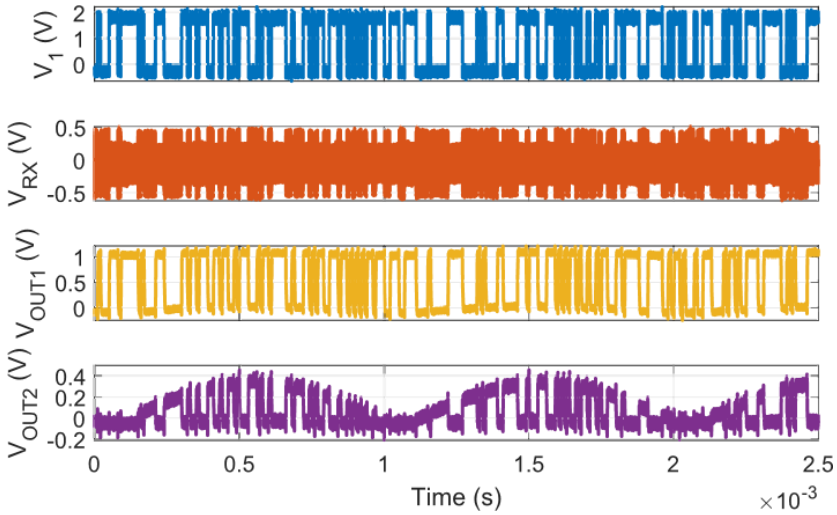

Figure 5.5.2. Over-the-air measurement results showing the received OOK backscattered signal at 920 MHz and the corresponding bit-stream applied to the switch's control voltage via the arbitrary function generator (AFG). V_1 serves as the control voltage for the switch and carries the uplink data, while V_{RX} represents the received backscattered signal. V_{OUT1} and V_{OUT2} denote the outputs of the rectifiers.

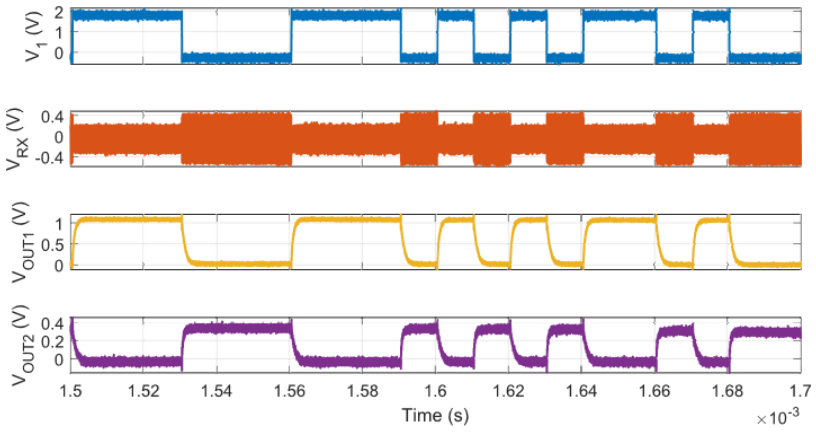

Figure 5.5.3. Over-the-air measurement results showing the zoomed-in received OOK backscattered signal at 920 MHz and the corresponding bit-stream applied to the switch's control voltage via the arbitrary function generator (AFG).

5.6 Solar-Powered Sensing

The experimental setup for the solar-powered sensing system is illustrated in Figure 5.6.1. This setup incorporates the designed dual-band antenna and circuit, a solar cell, a DC-DC converter, an electrolytic supercapacitor, an MSP430F5528 microcontroller, and an HDC2080 sensor to measure temperature and humidity.

The DC-DC converter regulates energy harvesting from ambient light to maintain a 3.3 V stable supply voltage. The electrolytic supercapacitor stores this harvested energy, facilitating continuous operation even under intermittent light conditions. The MSP430F5528

microcontroller, which operates at less than 100 μA, handles system control and data processing. Temperature and humidity measurements are provided by the HDC2080 sensor, consuming less than 0.5 μA per measurement.

Currently, the sensor is powered by harvested energy, while the microcontroller is connected to a USB power source for testing. The entire system will be powered solely by harvested energy in future designs. A lux meter recorded an ambient light intensity of approximately 338.8 lux to assess solar cell performance during the experiments. Figure 5.6.2 and Figure 5.6.3 show the received backscattered signal and temperature and humidity measurements, respectively.

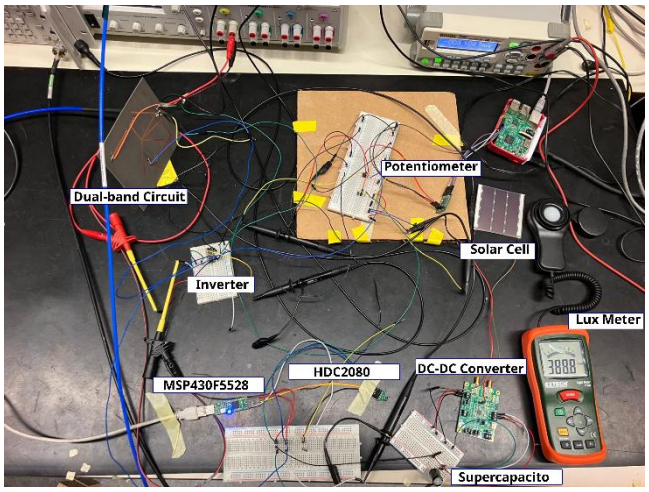

Figure 5.6.1. Experimental setup of the dual-band energy harvesting system integrating a solar cell, supercapacitor, and environmental sensor (HDC2080), real-time data processing on an MSP430 microcontroller and power regulation via a DC-DC converter.

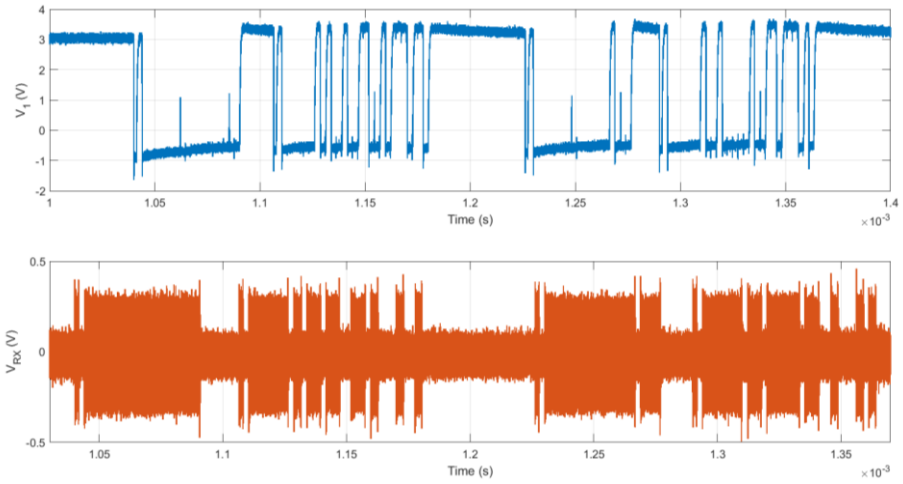

Figure 5.6.2. Received sensor data (V_{RX}) through backscattering.

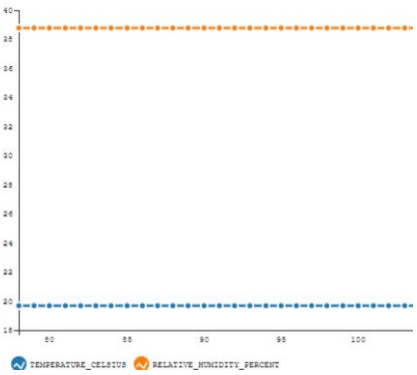

Figure 5.6.3. Measured temperature and humidity.

5.7 Solar-Powered Sensing Using Printed Supercapacitors and Solar Cells

This section examines solar-powered sensing systems using printed organic solar cells and supercapacitors for sustainable, energy-efficient IoT applications. A series-parallel configuration of solar cells, optimized to deliver 0.5 mA at 1 V, powers a DC-DC converter and charges a supercapacitor.

The chapter further analyzes the charging, discharging, and self-discharge behavior of printed supercapacitors under varying conditions, addressing energy retention challenges. Finally, the integration of these components into a solar-powered sensing system is demonstrated, showcasing autonomous operation and over-the-air data transmission using backscatter communication. This work highlights the potential of printed energy components for sustainable IoT applications.

5.7.1 Measurement with DC-DC Converter

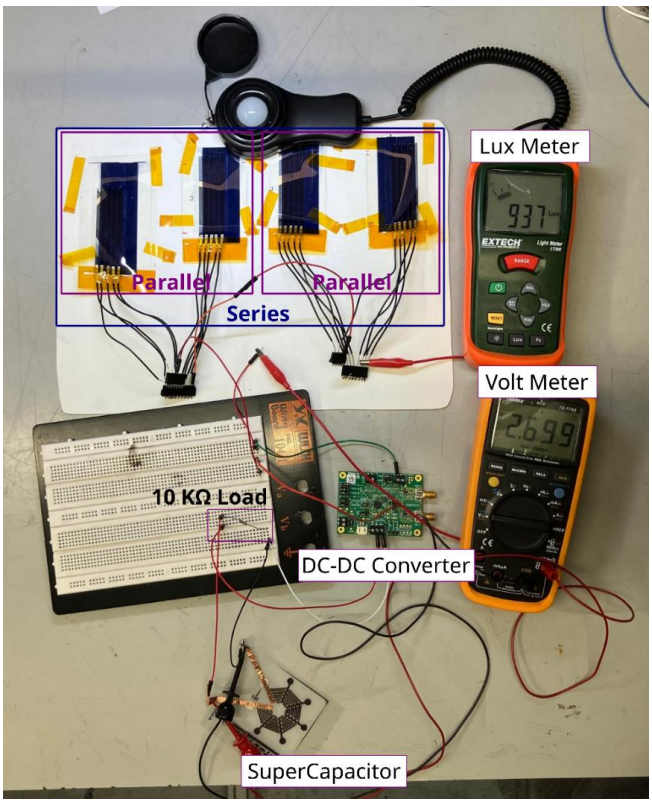

Figure 5.7.1. Experimental solar energy harvesting setup to configure the number of series and parallel elements to provide 0.5 mA × 0.9 V = 0.45 mW unloaded power for the use of electronic circuitry.

This laboratory test arrangement demonstrates a series-parallel configuration of flexible organic solar cells designed to supply a DC-DC converter with 80% and charge a flexible organic supercapacitor, meaning that the power delivered to the supercapacitor is about 0.36 mW. The performance of the solar cells is evaluated using a lux meter, which measures an illumination intensity of 937 lux. At the same time, a voltmeter records the supercapacitor's output voltage of 2.7 V, powering a 10 kΩ load. The objective of the experiment is to identify the optimal number of series and parallel solar cells needed to deliver a current of 0.5 mA at 1 V. In this setup, the requirements are fulfilled by connecting five solar cells in parallel and further connecting this arrangement in series with another identical set of five parallel-connected solar cells as shown in Figure 5.7.1, achieving the target power output of 0.35 mW when loaded.

5.7.2 Charging and Discharging of Micro Supercapacitor

We connected a printed micro supercapacitor to store the energy harvested using an OPV and DC-DC converter with a 10 kΩ load. Figure 5.7.2 shows charging and discharging cycles under illumination, with the voltage oscillating between 3.2 V and 1.75 V, demonstrating consistent energy harvesting and load delivery. Figure 5.7.3 shows the micro supercapacitor's self-discharge in darkness, where the voltage decays from 3.6 V to 0.96 V over 320 seconds.

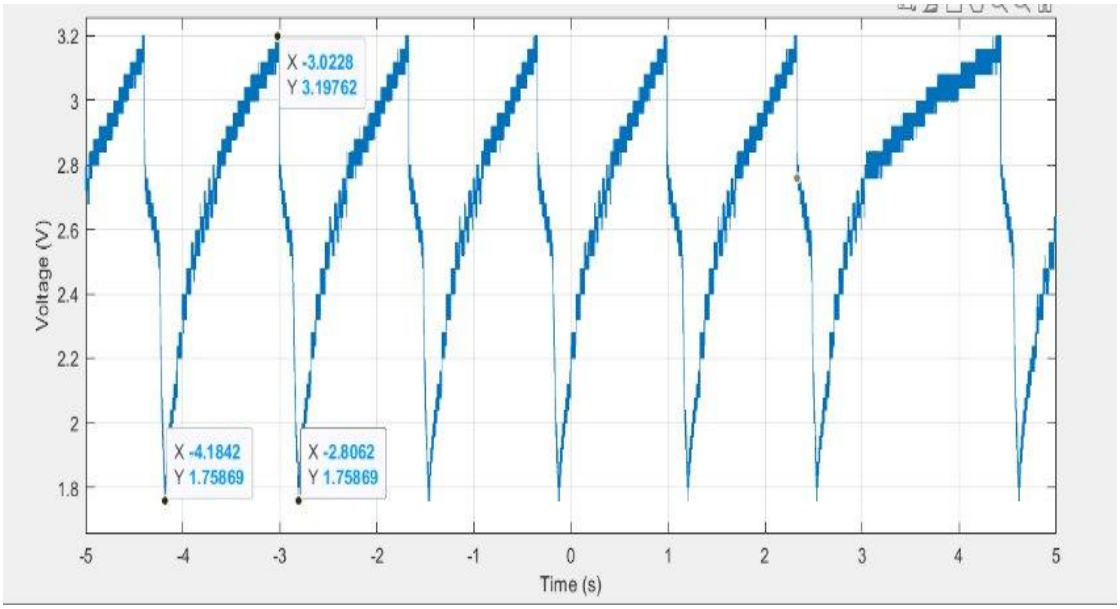

Figure 5.7.2. Charging and discharging cycles of the printed micro supercapacitor under illumination.

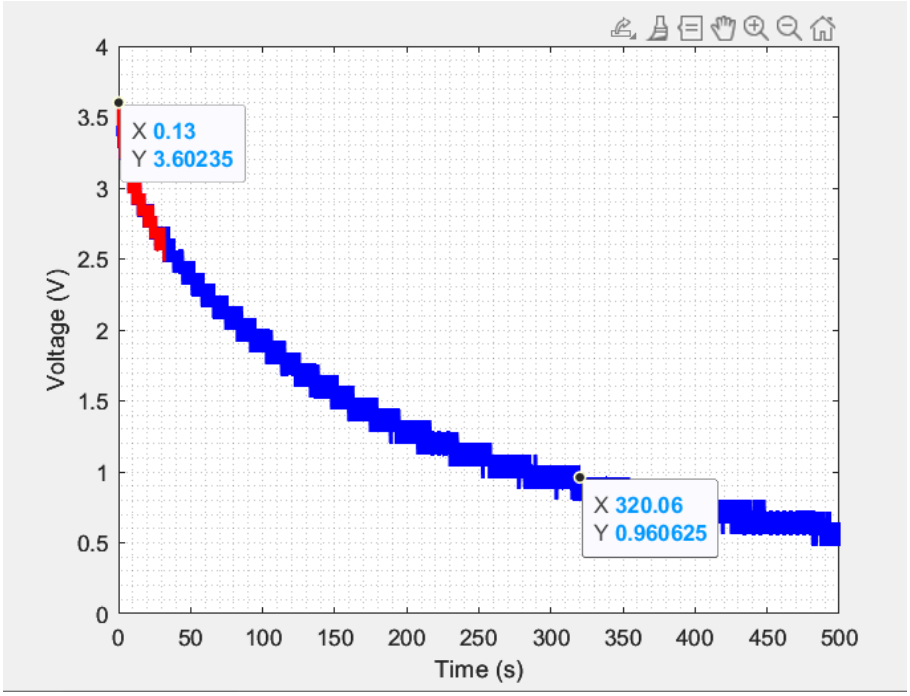

Figure 5.7.3. Voltage leakage behavior of a printed micro supercapacitor in the absence of light.

5.7.3 Combined With Electronics

The setup for solar-powered sensing using printed components is shown in Figure 5.7.4, and the received data over the air is presented in Figure 5.7.5.

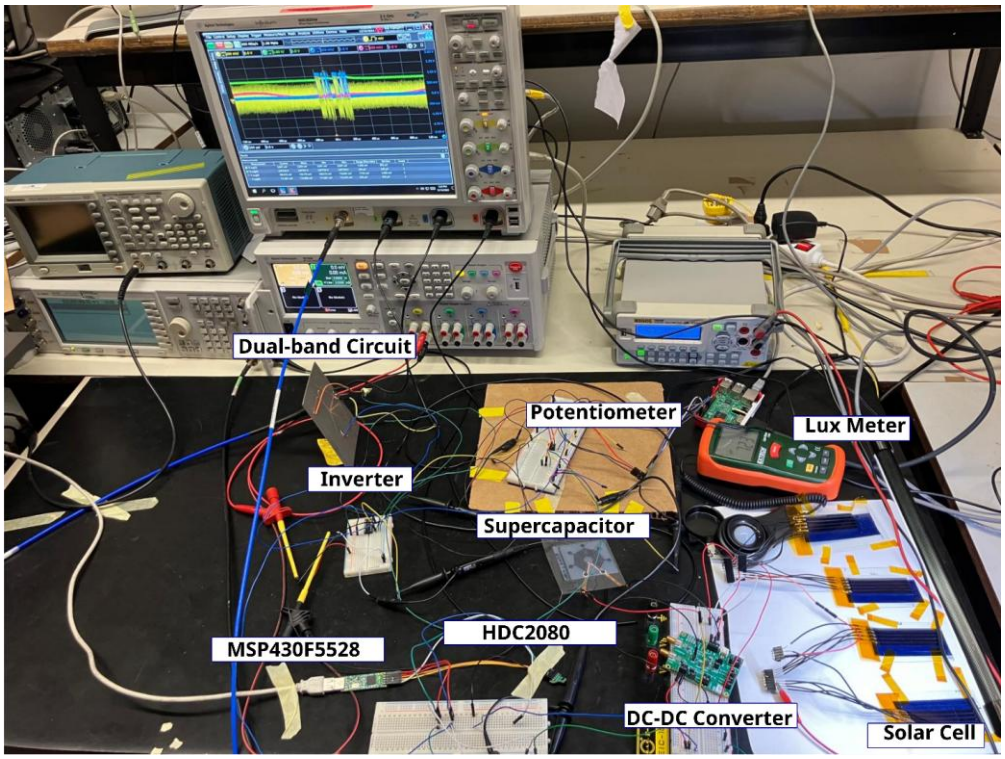

Figure 5.7.4. Experimental setup of the over-the-air sensing with the printed solar cells and micro supercapacitor.

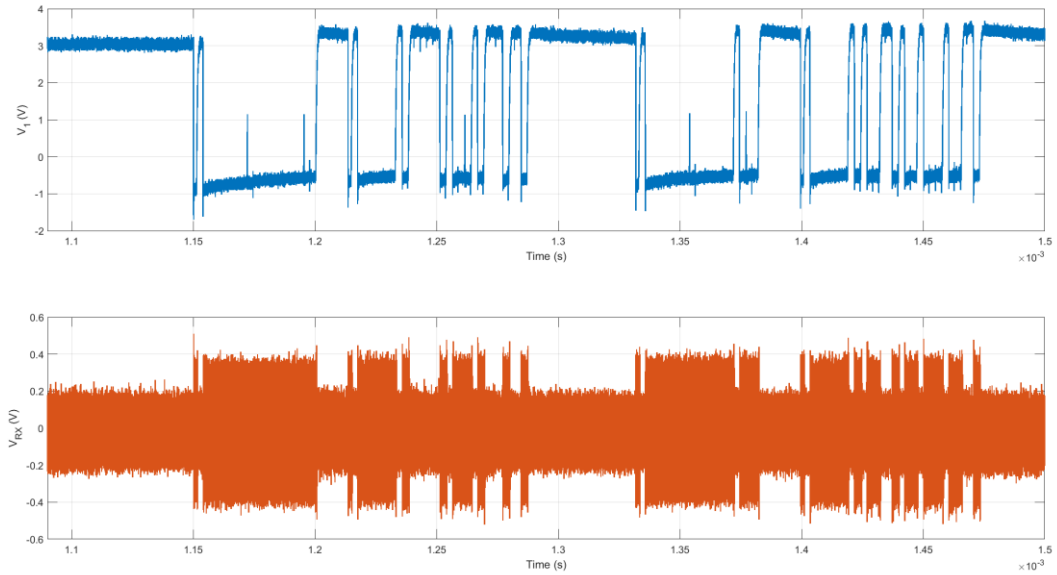

Figure 5.7.5. Received sensor data (V_{RX}) through backscattering while sensor is powered by the printed solar cells and micro supercapacitor.

5.8 Conclusion

This work demonstrated a dual-band, battery-less IoT node that unifies energy harvesting and bidirectional communication within a single architecture. By integrating SWIPT at 2.42 GHz and backscatter uplink at 0.92 GHz through a shared antenna and dual-band circuit, the node achieves efficient energy conversion and data transfer. Over-the-air experimental results confirm simultaneous energy harvesting with a 100-kbps uplink and a 1 kbps downlink. This approach offers a practical and sustainable solution, paving the way for long-lived, maintenance-free IoT deployments.

6 SLIPT Subsystem with Integrated Printed Electronics

Numerous energy sources, such as light in the form of ambient light from the sun or artificial light from the bulb and RF from dedicated or ambient sources, are investigated in the literature, as referenced in [10], [11], [12]. Light energy harvesting (EH), using photovoltaic (PV) cells, emerges with the highest harvested power density, of approximately 15 mW/cm2 outdoors and 100 μW/cm2 indoors, as detailed in [13]. This harvested energy is then utilised to power a battery-less IoT sensor node. Although the IoT node is equipped for EH, its capabilities significantly expand when it gains the ability to communicate [14].

Simultaneous Light Information and Power Transfer (SLIPT) presents a distinctive prospect for IoT sensors to harvest energy and receive data via light infrastructure, such as a light-emitting diode (LED). In this section, we will use the PV for both energy harvesting and front-end optical receiver. Hence, the PV is reconfigured for both functionalities without affecting its main functionality as an energy harvesting tool aligning with the sustainability goals of the SUPERIOT project.

6.1 System Model

The circuit model of the SLIPT receiver is depicted in Figure 6.1.1 will undergo analysis to assess both DC and AC characteristics, as detailed in [15]. DC aspects are contingent on various factors, such as the transmitted light intensity from the LED and the distance between the LED and the PV panel. Conversely, AC characteristics are significantly influenced by the collective values of resistance, capacitance, and inductance within the PV panel and the entire battery-less SLIPT receiver system. The detailed calculation and simulation are discussed in [15].

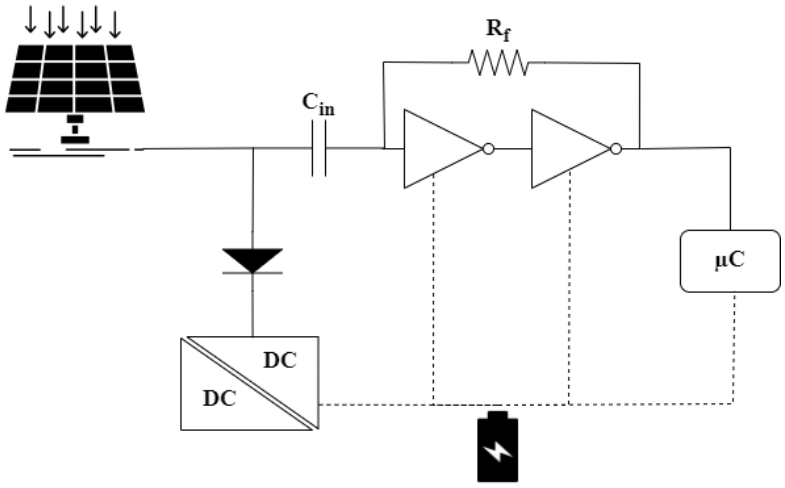

Figure 6.1.1. An overview of the system, including a PV SLIPT receiver employing two logic inverter gates as an optical receiver.

6.2 DC & AC Analysis

The optical power received at the PV panel's front end produces a photon current (Iph), which is then conveyed to the load in the form of a current (I_{PV}) as

$$I_{PV} = I_{ph} - I_d - \frac{V_{OC} - IR_s}{R_{sh}} \qquad (5.1)$$

Where I_d is the diode current, $R_s$and R_{sh} denote the series and shunt resistance of the PV, respectively, I is the output current to the load, and V_{OC} is the open-circuit voltage as depicted in Figure 6.2.1.

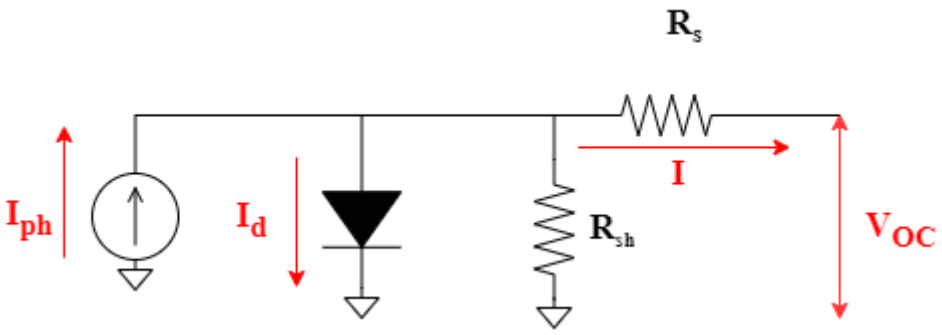

Figure 6.2.1. DC representation of a PV panel.

The inverter-based PV panel receiver's AC characteristics (such as the -3 dB bandwidth) present opportunities to utilize the solar panel as a downlink communication node. The model for this analysis is shown in Figure 6.2.2. For simplicity, the logic inverter is treated as an inverting op-amp in the analysis. Furthermore, the effect of the DC/DC converter, represented by L_{DC} and, R_{DC} can be ignored due to the high value of L_{DC} (in the range of a few μH). The analysis is further simplified by neglecting the shunt components, r_d and C_{PV} , as shown in Figure 6.2.2, since they do not impact the AC behavior of the SLIPT receiver system, which is modeled at the system input.

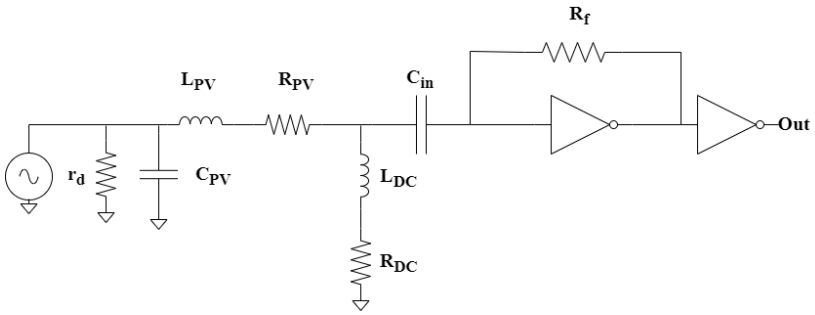

Figure 6.2.2. AC representation of the SLIPT receiver, including PV panel.

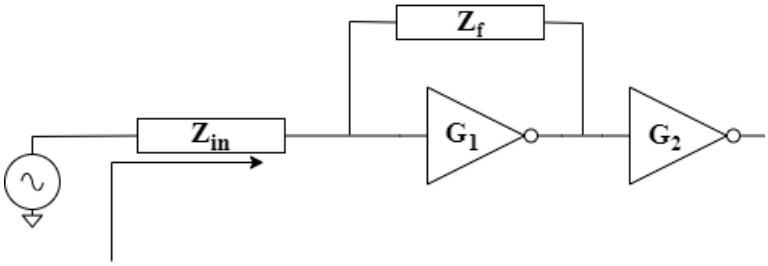

Figure 6.2.3. A simplified representation of the SLIPT receiver.

Figure 6.2.3 illustrates the simplified AC model used for the analysis. In this model, Z_{in} represents the series combination of L_{PV} , R_{PV} , and C_{in} , while R_f is symbolized by Z_f . Both Z_{in} and Z_f are expressed using complex frequency (s) to evaluate the dynamic bandwidth of the inverter-based SLIPT receiver.

$$H = G_1 G_2 = \left(-\frac{Z_f}{Z_{in}}\right)(-1) = \frac{sR_f C_{in}}{s^2 C_{in} L_{PV} + sR_{PV} C_{in} + 1} \quad (5.2)$$

6.3 Experimental Setup

The experimental configuration is depicted in Figure 6.3.1. We employ the RIGOL MSO5354 as a function generator and an oscilloscope to obtain the Bode plot. Additionally, RIGOL DP831 powers the LED optical transmitter, using 5 V and drawing 0.6 A. Consequently, the total power consumption on the transmitter side amounts to 3 W. The LED XHP50.3 is manufactured by CREE and equipped with a lens with a Full Width at Half Maximum (FWHM) of 36◦.

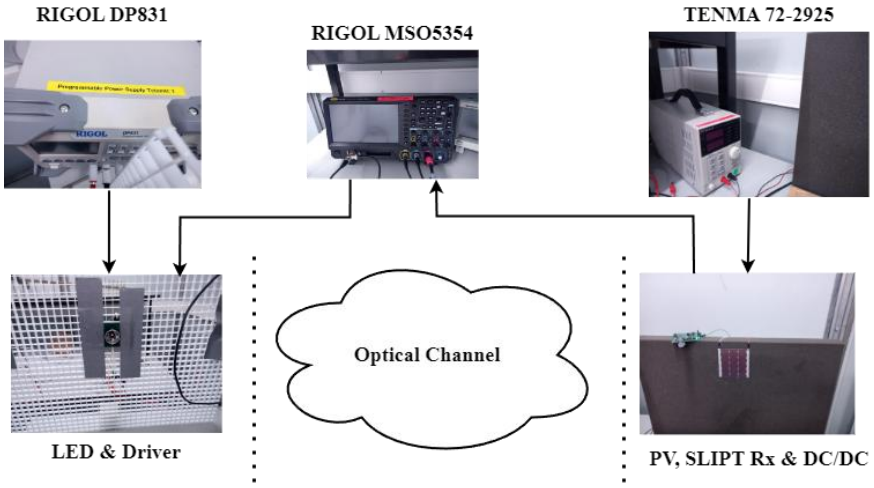

Figure 6.3.1. An experimental setup measures the SLIPT receiver's bandwidth and harvested power.

We positioned either the PowerSolarFilm a-Si model LL200-3.6-75, the Ascentsolar CIGS model B-003-018-026, or the printed OPV solar panel, developed at the VTT premises, at a distance (d) of 2 m from the transmitter on the receiver side. The respective areas for these panels are 0.005623 m^2 (73 x 74 mm), 0.002025 m^2 (45 x 45 mm) and 0.00066 m^2 (40 x 165 mm). The harvested energy per PV type (a-Si, CIGS, and OPV) has been performed and reported in Section 6.4.1 while the charging time of the printed supercapacitor of 3.3 mF (developed by NOVA.id.FCT) has been reported in Section 5.7.2. Finally, these three solar panels' frequency response or the expected -3 dB bandwidth is measured using the setup in Figure 6.3.1. We used a commercial DC-DC converter (AEM10941) from e-peas to manage energy harvesting.

6.4 Results and Discussion

6.4.1 Energy Harvesting: Traditional and Printed Solar Panel

The DC energy required to operate the SLIPT receiver is obtained from indoor radiated light emitted by the LEDs and ambient light. This study utilizes a single LED with a power consumption of 3 W. This results in about 186 lx. However, the illuminance for environments like offices and warehouses falls between 500 ~ 1000 lx [16]. Therefore, we increased the number of LEDs to about 700 lx and measured the potential harvested power. Figure 6.4.1 shows the experimental setup to measure the IV characteristic using a 700 lx light source.

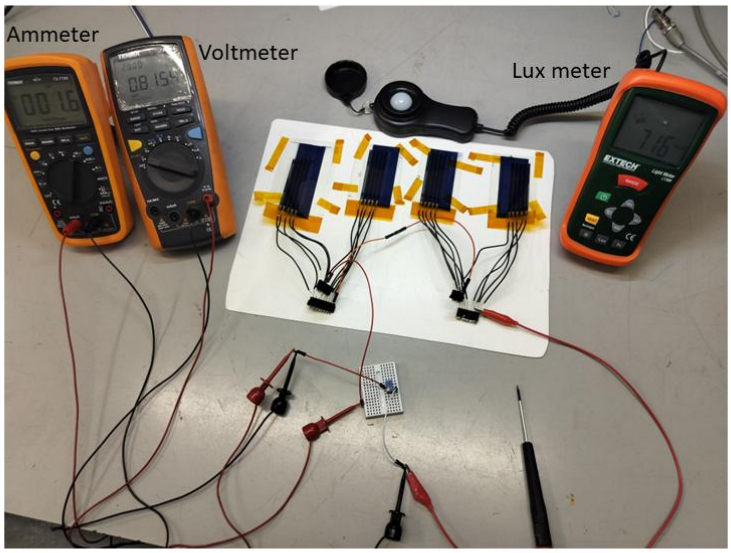

Figure 6.4.1. IV measurement for different PV using 700 lx.

The IV characteristics of three different solar panels, a-Si, CIGS, and OPV, show us their potential capability in energy harvesting under some illumination conditions, in this case, 700 lx. As depicted in Figure 6.4.2.

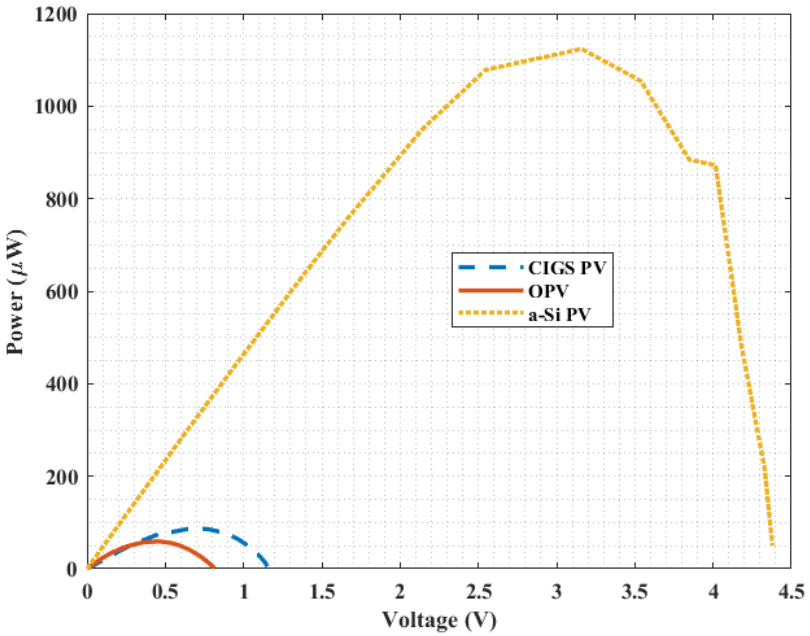

Figure 6.4.2. The IV characteristics of CIGS, a-Si, and OPV solar panels under 700 lx light intensity.

As expected, the a-Si generated the highest power in an indoor light setup. The CIGS performs poorly in indoor light setups, so the generated power is low. The CIGS is optimized for solar light not artificial light from LED. Finally, the OPV reported the least generated power, although the area of the OPV is the largest among the PVs.

6.4.2 -3 dB Bandwidth: Traditional and Printed Solar Panel

In Figure 6.4.3, the gain magnitudes for both CIGS and a-Si PV panels show similar performance, indicating that the magnitude of the internal resistance of the PV can be considered equal. The OPV shows a higher gain magnitude of about 3 dB, implying a double internal resistance of the PV panel. This represents a loss in the harvested power but a better gain for communication. An important observation pertains to the solar panels' -3 dB bandwidth: the a-Si panel demonstrates an operational bandwidth of 200 kHz, the CIGS panel exhibits a bandwidth of 1.5 MHz, and the OPV has a bandwidth of about 65 kHz for both 4 connected OPVs as shown in Figure 6.4.1 as a single OPV element. This discrepancy arises from differences in materials and the stacking configuration of the PV panels, leading to distinct dynamic behaviors. Furthermore, the differences in the bandwidth can be attributed to parasitic capacitance and inductance in all connections between the solar panel and inverter gate. We also observed that the total area of the PV does not have an essential impact on the bandwidth.

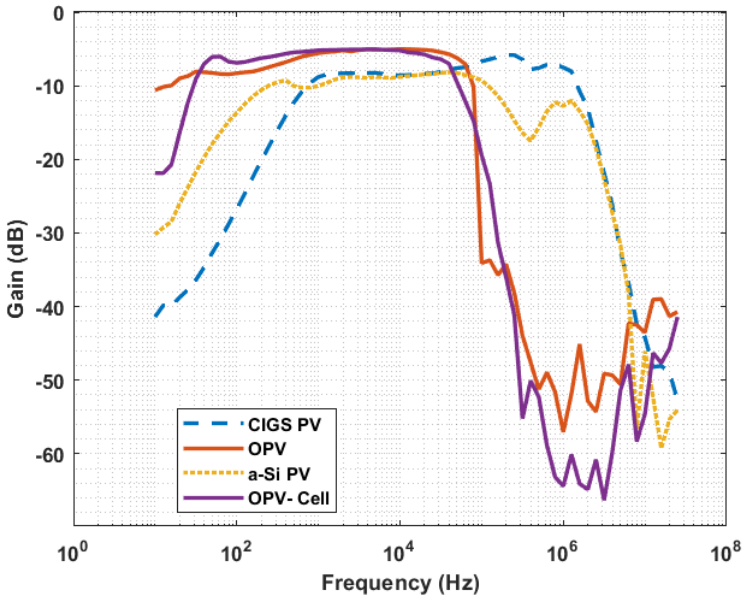

Figure 6.4.3. The -3 dB bandwidth of three types of PV.

An example of received data using the single OPV is plotted against time to check the practical data reception as plotted in Figure 6.4.4.

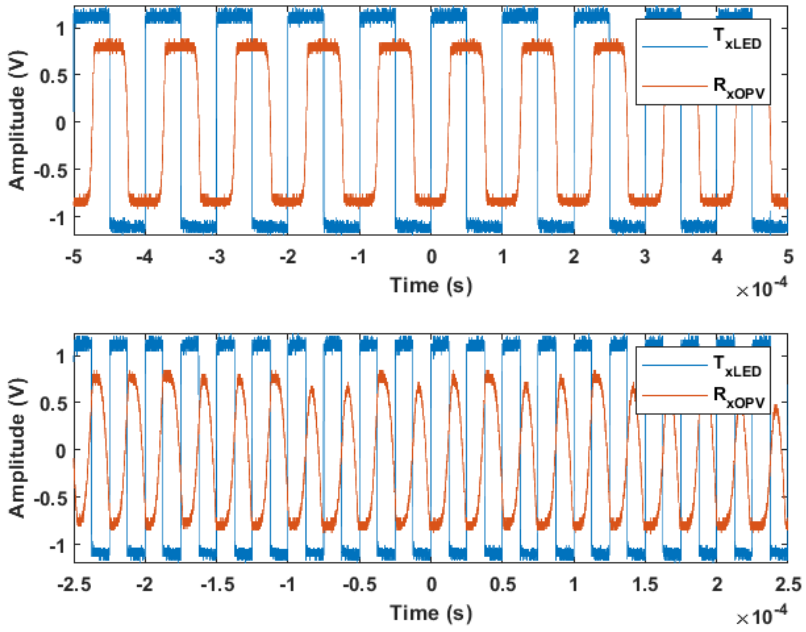

Figure 6.4.4. On-off keying data with 50% duty cycle using two different frequencies.

In this experiment, we transmitted light information using 10 and 40 kHz frequencies, respectively. We noticed that at 40 kHz, the received signal started to degrade, which coincides with the degrading in magnitude of the OPV cell in Figure 6.4.3.

6.5 Conclusion

We presented a reconfigurable IoT solution with minimal hardware, integrating a solar panel as an energy harvester and a communication front-end using light. The study explored various energy harvesting capabilities with three types of solar panels: traditional a-Si, CIGS, and printed OPV. The traditional a-Si panel achieved the highest unloaded harvesting power at 1.2 mW, while the CIGS panel demonstrated a bandwidth of 1.2 MHz.

7 Evaluation of different designs for the energy subsystem in the context of demonstrators and use cases

The energy subsystem is crucial for achieving a sustainable, energy-autonomous RIoT node. It comprises three main components:

- **Energy Conversion Block**: Facilitates energy harvesting from dual sources (light via PV cells and radio via RF antennas).
- **Energy Storage Block**: Employs capacitors instead of batteries, offering non-toxic, battery-free operation with lower maintenance, longer lifespan, and wider temperature tolerance.
- **Energy Management Block**: Optimizes energy harvesting, storage, and consumption to enhance efficiency.

The subsystem's design must align with use-case requirements, factoring in environmental conditions, material durability, harvesting scenarios, power demands, and duty cycles. Various configurations are possible based on the chosen solutions.

The SUPERIOT project explores and evaluates different topologies for these components across four demonstrators and use cases, emphasizing sustainability, reconfigurability, and energy efficiency.

The different designs for the energy subsystem have been considered in D2.1. The designs have been analyzed and evaluated in the context of demonstrators and use cases that had been defined in WP1. The details on the analysis performed can be found in the above-mentioned deliverable. The results of this analysis can be found below in the form of the tables that concludes the evaluation of different designs of three main components of the energy subsystem in the context of demonstrators and use cases:

- energy harvesting design in Table 11,
- energy storage design in Table 12,
- energy management design in Table 13.

Table 11. Evaluation of energy harvesting design of the energy subsystem in the context of demonstrators and use cases.

Demonstrator	Potential Application / Use Cases	High	Moderate	Low or not applicable
Demonstrator 1: Sustainable Smart Tag	1.2 - Smart tags incorporated in sensitive items 1.4 - Tags specifically designed for logistic operations 1.5 - Enhanced label for batch manufacturing 1.6 - Tags incorporated in shelves or in other small product packages 1.7 - Tags and labels for healthcare patients 2.1 - Sensors and actuators for smart buildings	•**RF:** Three-chip (backscatter switch); Adaptive MAC-based; Ink-jet-printed; Sheet-to-sheet-printed; Roll-to-roll-printed •**Light:** EcoSense and Eco-node; BLE beacon; Simple PV; PV indoor; Organic photovoltaics •**Hybrid (dual-mode):** rectangular shorted antenna and flexible film solar cell; amorphous silicon solar cell mounted on	•**RF:** Dipole antenna-based UHF (medium efficiency); Adaptive rectenna; Commercial; Cellular •**Light:** Current Starved-Voltage Controlled Oscillator feedback quasi PV	•**RF:** Embedded (low-efficiency); Air-gap-based power controllable (low efficiency) •**Hybrid (dual-mode):** electric field of fluorescent light (high potential to be in hybrid with light harvesting)

	2.2 - Sensors and actuators for construction monitoring	the RF 2.4 GHz patch antenna		
	2.3 - Sensors for medical and safety applications			
	2.4 - Sensors and actuators applied to smart cities			
	3.1 - Secure and private IoT communication			
	3.2 - Reliable IoT communication			
Demonstrator 2: Advanced Logistics in Medical ICT Scenarios	1.3 - Tags and labels specifically designed for medicines	●**RF:** Three-chip (backscatter switch); Adaptive MAC-based; Ink-jet-printed; Sheet-to-sheet-printed; Roll-to-roll-printed ●**Light:** EcoSense and Eco-node; BLE beacon; Simple PV; PV indoor; Organic photovoltaics ●**Hybrid (dual-mode):** rectangular shorted antenna and flexible film solar cell; amorphous silicon solar cell mounted on the RF 2.4 GHz patch antenna	●**RF:** Dipole antenna-based UHF (medium efficiency); Adaptive rectenna; Commercial; Cellular ●**Light:** Current Starved-Voltage Controlled Oscillator feedback quasi PV	●**RF:** Embedded (low-efficiency); Air-gap-based power controllable (low efficiency) ●**Hybrid (dual-mode):** electric field of fluorescent light (high potential to be in hybrid with light harvesting)
	1.4 - Tags specifically designed for logistic operations			
	1.7 - Tags and labels for healthcare patients			
	1.9 - Labels for tracking critical equipment			
	2.3 - Sensors for medical and safety applications			
	3.1 - Secure and private IoT communication			
	3.2 - Reliable IoT communication			
Demonstrator 3: Printed Limited-capability IoT Node	1.1 - Smart labels attached or incorporated in day-to-day market products (with reduced capabilities)	●**RF:** Ink-jet-printed; Sheet-to-sheet-printed; Roll-to-roll-printed ●**Light:** Organic photovoltaics ●**Hybrid (dual-mode):** rectangular shorted antenna and flexible film solar cell; amorphous silicon solar cell mounted on the RF 2.4 GHz patch antenna		●**RF:** Three-chip; Air-gap-based power controllable; Cellular; Embedded; Adaptive MAC-based; Dipole antenna-based UHF(medium efficiency); Adaptive rectenna; Commercial ●**Light:** EcoSense and Eco-node; BLE beacon; Simple PV; PV indoor; Current Starved-Voltage Controlled Oscillator feedback quasi PV. ●**Hybrid (dual-mode):** electric field of fluorescent light
	1.2 - Smart tags incorporated in sensitive items (with reduced capabilities)			
	2.1 - Sensors and actuators for smart buildings (with reduced capabilities)			
Demonstrator 4: Large-area IoT Node	2.2 - Sensors and actuators for construction monitoring	●**RF:** Three-chip (backscatter switch); Adaptive MAC-based; Ink-jet-printed; Sheet-to-sheet-printed; Roll-to-roll-printed ●**Light:** EcoSense and Eco-node; BLE beacon; Simple PV; PV	●**RF:** Dipole antenna-based UHF (medium efficiency); Adaptive rectenna; Commercial; Cellular ●**Light:** Current Starved-Voltage Controlled Oscillator feedback quasi PV	●**RF:** Embedded (low-efficiency); Air-gap-based power controllable (low efficiency) ●**Hybrid (dual-mode):** electric field of fluorescent light (high potential to be in hybrid with light harvesting)
	2.4 - Sensors and actuators applied to smart cities			
	3.5 - Coverage extension with large-area IoT nodes			

		indoor; Organic photovoltaics •**Hybrid (dual-mode):** rectangular shorted antenna and flexible film solar cell; amorphous silicon solar cell mounted on the RF 2.4 GHz patch antenna		

Table 12. Evaluation of energy storage design of the energy subsystem in the context of demonstrators and use cases.

Demonstrator	Potential Application / Use Cases	High	Moderate	Low or not applicable
Demonstrator 1: Sustainable Smart Tag	1.2 - Smart tags incorporated in sensitive items	PMSC (printed); SC; MSC	MLCC; PAC-ML; PTC	PAC-R (low compact); MTC(high ESR); EAC (high ESR)
	1.4 - Tags specifically designed for logistic operations			
	1.5 - Enhanced label for batch manufacturing			
	1.6 - Tags incorporated in shelves or in other small product packages			
	1.7 - Tags and labels for healthcare patients			
	2.1 - Sensors and actuators for smart buildings			
	2.2 - Sensors and actuators for construction monitoring			
	2.3 - Sensors for medical and safety applications			
	2.4 - Sensors and actuators applied to smart cities			
	3.1 - Secure and private IoT communication			
	3.2 - Reliable IoT communication			
Demonstrator 2: Advanced Logistics in Medical ICT Scenarios	1.3 - Tags and labels specifically designed for medicines	PMSC (printed); SC; MSC	MLCC, PAC-ML, PTC	PAC-R (low compact); MTC(high ESR); EAC (high ESR)
	1.4 - Tags specifically designed for logistic operations			
	1.7 - Tags and labels for healthcare patients			
	1.9 - Labels for tracking critical equipment			

	2.3 - Sensors for medical and safety applications			
	3.1 - Secure and private IoT communication			
	3.2 - Reliable IoT communication			
Demonstrator 3: Printed Limited-capability IoT Node	1.1 - Smart labels attached or incorporated in day-to-day market products (with reduced capabilities)	PMSC (printed)		MLCC, PAC-ML, PTC; PAC-R (low compact); MTC(high ESR); EAC (high ESR)
	1.2 - Smart tags incorporated in sensitive items (with reduced capabilities)			
	2.1 - Sensors and actuators for smart buildings (with reduced capabilities)			
Demonstrator 4: Large-area IoT Node	2.2 - Sensors and actuators for construction monitoring	PMSC (printed); SC; MSC	MLCC, PAC-ML, PTC	PAC-R (low compact); MTC (high ESR); EAC (high ESR)
	2.4 - Sensors and actuators applied to smart cities			
	3.5 - Coverage extension with large-area IoT nodes			

Table 13. Evaluation of energy management design of the energy subsystem in the context of demonstrators and use cases.

Demonstrator	Potential Application / Use Cases	High	Moderate	Low or not applicable
Demonstrator 1: Sustainable Smart Tag	1.2 - Smart tags incorporated in sensitive items	●**Wireless standard:** BLE, LoRa, SigFox; Zigbee, properietary ●**Radio-optimization:** Tx power control; directional antenna (direction of communication needed to be known), cognitive radio ●**Data optimization:** modulation and coding schemes, RLE (lossless compression), aggregation and clustering ●**Scheduling schemes:** sleep scheduling, message scheduling, traffic scheduling, wake-up scheduling	●**Wireless standard:** Cellular ●**Data optimization:** compressive sensing (lossy compression), probabilistic structure, named data networking ●**Routing and topology control:** multipath routing ●**Messaging protocols:** AMQP	●**Wireless standard:** WiFi, WiMAX
	1.4 - Tags specifically designed for logistic operations			
	1.5 - Enhanced label for batch manufacturing			
	1.6 - Tags incorporated in shelves or in other small product packages			
	1.7 - Tags and labels for healthcare patients			
	2.1 - Sensors and actuators for smart buildings			
	2.2 - Sensors and actuators for construction monitoring			
	2.3 - Sensors for medical and safety applications			

	2.4 - Sensors and actuators applied to smart cities 3.1 - Secure and private IoT communication 3.2 - Reliable IoT communication	•**Routing and topology control:** energy efficient routing, distributed topology control •**Messaging protocols:** MQTT, CoAP		
Demonstrator 2: Advanced Logistics in Medical ICT Scenarios	1.3 - Tags and labels specifically designed for medicines 1.4 - Tags specifically designed for logistic operations 1.7 - Tags and labels for healthcare patients 1.9 - Labels for tracking critical equipment 2.3 - Sensors for medical and safety applications 3.1 - Secure and private IoT communication 3.2 - Reliable IoT communication	•**Wireless standard:** BLE, LoRa, SigFox; Zigbee •**Radio-optimization:** Tx power control; directional antenna (direction of communication needed to be known), cognitive radio •**Data optimization:** modulation and coding schemes, RLE (lossless compression), aggregation and clustering •**Scheduling schemes:** sleep scheduling, message scheduling, traffic scheduling, wake-up scheduling •**Routing and topology control:** energy efficient routing, distributed topology control •**Messaging protocols:** MQTT, CoAP	•**Wireless standard:** Cellular •**Data optimization:** compressive sensing (lossy compression), probabilistic structure, named data networking •**Routing and topology control:** multipath routing •**Messaging protocols:** AMQP	•**Wireless standard:** WiFi, WiMAX
Demonstrator 3: Printed Limited-capability IoT Node	1.1 - Smart labels attached or incorporated in day-to-day market products (with reduced capabilities) 1.2 - Smart tags incorporated in sensitive items (with reduced capabilities) 2.1 - Sensors and actuators for smart buildings (with reduced capabilities)	•**Radio-optimization:** directional antenna (direction of communication needed to be known) •**Scheduling schemes:** wake-up scheduling	•**Wireless standard:** BLE, LoRa, SigFox; Zigbee •**Data optimization:** modulation and coding schemes; aggregation and clustering •**Routing and topology control:** multipath routing	•**Wireless standard:** WiFi, WiMAX; Cellular •**Radio-optimization:** Tx power control; cognitive radio •**Data optimization:** RLE (lossless compression);compressive sensing (lossy compression), probabilistic structure, named data networking •**Messaging protocols:** AMQP •**Scheduling schemes:** sleep scheduling, message scheduling, traffic scheduling •**Routing and topology control:** energy efficient routing, distributed topology control

Demonstrator 4: Large-area IoT Node	2.2 - Sensors and actuators for construction monitoring 2.4 - Sensors and actuators applied to smart cities 3.5 - Coverage extension with large-area IoT nodes	●**Wireless standard:** BLE, LoRa, SigFox; Zigbee ●**Radio-optimization:** Tx power control; directional antenna (direction of communication needed to be known), cognitive radio ●**Data optimization:** modulation and coding schemes, RLE (lossless compression), aggregation and clustering ●**Scheduling schemes:** sleep scheduling, message scheduling, traffic scheduling, wake-up scheduling ●**Routing and topology control:** energy efficient routing, distributed topology control ●**Messaging protocols:** MQTT, CoAP	●**Wireless standard:** Cellular ●**Data optimization:** compressive sensing (lossy compression), probabilistic structure, named data networking ●**Routing and topology control:** multipath routing ●**Messaging protocols:** AMQP	●**Wireless standard:** WiFi, WiMAX

8 Conclusion

8.1 Summary of Findings

Task 2.4's integrated energy subsystem enables energy-autonomous IoT devices that remain functional while significantly reducing their carbon and material footprints. The energy characterization of the SUPERIOT Si-based RIoT node has provided a strong foundation for optimizing hybrid and printed IoT nodes. Extensive measurements enabled the development of models with over 97% accuracy in predicting energy consumption across three operating modes, supporting precise energy budgeting and optimization. These models will guide energy management strategies as the project integrates energy harvesting and printed electronics, ensuring efficient operation under varying conditions. Benchmarking the current Si-node's performance ensures iterative advancements in energy sustainability for future designs.

The project has also demonstrated dual-source energy harvesting through experimental subsystems combining RF and visible-light harvesting, ensuring robust power availability and aligning with sustainable design principles. Furthermore, prototype nodes have achieved near-battery-less operation by employing Simultaneous Wireless Information and Power Transfer (SWIPT) and Simultaneous Light Information and Power Transfer (SLIPT), reducing dependence on batteries. The use of printed electronics, including sustainable organic solar cells and supercapacitors, aligns with eco-design guidelines, enabling lightweight, flexible, and recyclable implementations. These innovations not only lower e-waste but also contribute to the circular economy goals envisioned in the project.

8.2 Future Work and Recommendations

Moving forward, the Task 2.4 subsystems will undergo further refinement and integration with the organic components and DC-DC converter developed by our partners. These will be utilized in WP4 demonstrators, where they will be tested with higher-level application scenarios and real-world conditions. We plan to integrate SWIPT and SLIPT to demonstrate a hybrid system for light and RF energy harvesting and communication in WP4.

The insights gained from Task 2.4 ensure that the SUPERIOT project contributes to the broader ambition of building a hyperconnected world that remains environmentally, economically, and socially responsible. By harmonising radio and optical technologies with sustainable practices, the project addresses the critical challenges of powering billions of IoT devices—without sacrificing performance or escalating e-waste—and moves closer to fulfilling the high-level objectives and KPIs outlined in Section 1.1 of the proposal.

9 References

[1] W. He, Z. Yi, S. Shen, Z. Huang, L. Liu, T. Zhang, W. Li, L. Wang, L. Shui, C. Zhang and G. Zhou, "Driving waveform design of electrophoretic display based on optimized particle activation for a rapid response speed," *Micromachines,* vol. 11, no. 5, p. 498, 2020.

[2] M. J. Bocus, *SUPERIOT_UoB - Resources for Node and Network-level Energy Measurement, Analysis, Modeling and Prediction in the SUPERIOT Framework,* GitHub, 2026.

[3] M. J. Bocus, J. Hakkinen, H. Fontes, M. Drzewiecki, S. Qiu, K. Eder and R. Piechocki, *An Energy-Aware RIoT System: Analysis, Modeling and Prediction in the SUPERIOT Framework,* arXiv, 2025.

[4] A. A. Abdellatif, S. Silva, E. Baltazar, B. Oliveira, S. Qiu, M. J. Bocus, K. Eder, R. J. Piechocki, N. T. Almeida and H. Fontes, "RIoT Digital Twin: Modeling, Deployment, and Optimization of Reconfigurable IoT System With Optical–Radio Wireless Integration," *IEEE Open Journal of the Communications Society,* vol. 7, p. 2178–2196, 2026.

[5] R. Ma, J. Tang, X. Y. Zhang, K.-K. Wong and J. A. Chambers, "RIS-Assisted SWIPT Network for Internet of Everything Under the Electromagnetics-Based Communication Model," *IEEE Internet of Things Journal,* vol. 11, no. 9, pp. 15402-15415, 2024.

[6] V. U. Oliveira, P. Capitão and N. B. Carvalho, "Railways Temperature Sensing and Monitoring Based on Passive Harmonic RFID Systems," *IEEE Transactions on Microwave Theory and Techniques,* pp. 1-11, 2024.

[7] Y. Qaragoez, S. Pollin and D. Schreurs, "Biased-FSK Modulation for Simultaneous Wireless Information and Power Transfer," *IEEE Transactions on Microwave Theory and Techniques,* vol. 72, no. 12, pp. 7071-7084, 2024.

[8] I.-T. Chen and M. M. Tentzeris, "Millimeter Wave Dual-Polarized Semi-Passive Energy Detection Backscattering RFID," in *2024 IEEE Wireless Power Technology Conference and Expo (WPTCE)*, Kyoto, Japan, 2024.

[9] L. Hüssen, M.-D. Wei and R. Negra, "Broadband High-Efficiency Microwave Rectifier with Nonuniform Transmission-Line Input Matching for Harmonic Backscattering Applications," in *2024 IEEE/MTT-S International Microwave Symposium - IMS 2024*, Washington, DC, USA, 2024.

[10] L. Balocchi, V. Palazzi, S. Bonafoni, F. Alimenti, P. Mezzanotte and L. Roselli, "Compact Green Harmonic Transponders for Parcel Tracking," *IEEE Journal of Radio Frequency Identification,* vol. 7, pp. 247-256, 2023.

[11] J. Zhang, S. D. Joseph, Y. Huang and J. Zhou, "Compact Single-Port Harmonic Transponder for Backscattering Communications and Energy Harvesting Applications," *IEEE Transactions on Microwave Theory and Techniques,* vol. 71, no. 7, pp. 3136-3143, 2023.

[12] Y. Dia, H. Ribeiro, L. Oyhenart, E. Zaraket, L. Fadel, V. Vigneras, C. Dejous, N. Carvalho and S. Hemour, "A Wireless Motion Sensor Operating Down to −28-dBm Energy Harvesting," *IEEE Journal of Radio Frequency Identification,* vol. 8, pp. 176-184, 2024.

[13] ISO, "ISO 8995-1:2002 - Lighting of work places," ISO , Sep 2005. [Online]. Available: https://www.iso.org/standard/28857.html . [Accessed 1 11 2023].

[14] Y. Qaragoez, S. Pollin and D. Schreurs, "A low power backscattering architecture for batteryless sensor nodes," in *2021 IEEE MTT-S International Microwave and RF Conference (IMARC)*, KANPUR, India, 2021.

[15] K. Hammoud, D. Schreurs and S. Pollin, "Sustainable and Low-Power Logic Inverter-Based Batteryless SLIPT Receiver for IoT Nodes," in *2024 Joint European Conference on Networks and Communications & 6G Summit (EuCNC/6G Summit)*, Antwerp, Belgium, 2024.

[16] K. Hammoud, S. Pollin and D. Schreurs, "Efficient indoor solar panel energy harvesting exploiting the crest factor,," in *2022 Wireless Power Week (WPW)*, Bordeaux, France, 2021.

[17] P. Dhull, D. Schreurs, G. Paolini, A. Costanzo, M. Abolhasan and N. Shariati, "Multitone PSK modulation design for simultaneous wireless information and power transfer," *IEEE Transactions on Microwave Theory and Techniques,* vol. 72, no. 1, pp. 446-460, 2024.

[18] H. J. Visser and K. Hammoud, "A 2.45 GHz shielded, miniature power and data receive," in *2021 IEEE Wireless Power Transfer Conference(WPTC),*, San Diego, CA, USA, 2021.

[19] . T. Sanislav, G. D. Mois, . S. Zeadally and S. C. Folea, "Energy harvesting techniques for internet of things (IoT)," *IEEE Access,* vol. vol. 9, pp. 39530-39549, 2021.

[20] S.-H. Wu, X. Xu, Z. Yue, Y.-L. Yang, S. Li, X.-Q. Lin, Y. Yu and Y. Liu, "Integrated Rectifying-Mixer Circuit for Simultaneous Wireless Information and Power Transfer (SWIPT)," *IEEE Microwave and Wireless Technology Letters,* vol. 34, no. 7, pp. 959-962, 2024.

10 List of figures

11 List of tables

12 List of contributors

Contributors	Short name	Country
KATHOLIEKE UNIVERSITEIT LEUVEN	KU Leuven	Belgium
UNIVERSITY OF BRISTOL	U of Bristol	United Kingdom
NOVA ID FCT - ASSOCIACAO PARA A INOVACAO E DESENVOLVIMENTO DA FCT	NOVA.id.FCT	Portugal
TEKNOLOGIAN TUTKIMUSKESKUS VTT OY	VTT	Finland
MPICOSYS - EMBEDDED PICO SYSTEMS SPZOO	MPICOSYS	Poland
OULUN YLIOPISTO	UOULU	Finland